UNIVERSITY OF CAPE TOWN
IYUNIVESITHI YASEKAPA • UNIVERSITEIT VAN KAAPSTAD

Development of a fatigue tester and material model for flexible heart valve applications

University of Cape Town

Braden van Breda

Supervisor: Prof. Hennie Mouton
Co-Supervisor: Prof. Deon Bezuidenhout

Department of Mechanical Engineering
University of Cape Town

April 23, 2019

This work is submitted in partial fulfilment of the requirements of the degree of Master of Science in Engineering specialising in Mechanical Engineering.

The copyright of this thesis vests in the author. No quotation from it or information derived from it is to be published without full acknowledgement of the source. The thesis is to be used for private study or non-commercial research purposes only.

Published by the University of Cape Town (UCT) in terms of the non-exclusive license granted to UCT by the author.

University of Cape Town

Declaration

1. I know the meaning of plagiarism and declare that all the work in the document, save for that which is properly acknowledged, is my own.

2. This thesis/dissertation has been submitted to the Turnitin module (or equivalent similarity and originality checking software) and I confirm that my supervisor has seen my report and any concerns revealed by such have been resolved with my supervisor.

3. I have used the IEEE convention for citation and referencing. Each significant contribution to, and quotation in, this report from work(s) of other people has been attributed, and has been cited and referenced.

4. I have not allowed, and will not allow anyone to copy my work with the intention of passing it off as his or her own work.

Signed by candidate

Braden van Breda (VBRBRA003)

Abstract

The leaflet material in heart valve prostheses is required to be both flexible and durable to eliminate the need for chronic anticoagulation medication and accommodate younger patients with longer life expectancies. This investigation aims to provide two of the necessary tools to design and test suitably flexible and durable materials for heart valve replacement.

These tools address the question of how to model the stress-strain behaviour of polymer networks and thermoplastic polyurethanes in particular, as well as how to practically evaluate the durability of the proposed material.

A model for polyurethane stress-strain behaviour is proposed, whereby the number of monomers between crosslinks is suggested to evolve with macroscopic strain. Following the polymer chain entanglement theory, the increase in the number of monomers between crosslinks is further extended to be a function of strain rate, incorporating the viscous effect observed in polyurethanes. A multistation, micro-tensile specimen fatigue tester was developed to evaluate material durability.

The proposed equilibrium polyurethane model accurately predicts the experimental data across the full material strain range. The proposed model extension sufficiently captures the rate dependence of polyurethane, however, fails to account for the raised specimen temperatures at high strain rates. The developed fatigue tester is verified to successfully feature selectable variables including test frequency (1 - 20 Hz), amplitude (1 - 6 mm), waveform (Triangular, Sinusoidal, Square and Custom) and environmental temperature control (23 - 50 ^{o}C). Less than 10% error in measured force is observed when compared to a commercial tensile tester.

The proposed model successfully provides a platform to aid the design of flexible materials suitable for heart valve leaflets. The developed fatigue tester enables the assessment of material durability across a range of test conditions, successfully providing a tool for leaflet material durability analysis and verification.

Acknowledgements

I would like to thank Strait Access Technologies by affording me the opportunity to do my masters by funding the 3 years tuition and the machine materials.

I would like to thank my supervisor Prof. Mouton and Prof. Bezuidenhout for their technical support. I especially appreciate your understanding of my additional work commitments, and being patient with me when it comes to deliverables.

Special mention to Dr J. de Villers and J. Coetzee for the essential insight into the mechanisms of polymerisation. This background significantly supported the material model derivation.

To all my close friends, thank you for accepting my absenteeism, and I look forward to catching it all up.

To my ever supportive family, to my mother, Helen van Breda and sister, Jadine van Breda thank you for the constant messages of encouragement and love, this really helped to keep me going. To my father, Mark van Breda, thank you for all the technical advice and pulling out the old engineering books when I was stumped. Also for the financial support throughout this project.

To my loving wife, Lise van Breda, thank you for being there every step of the way, I really could not have done it without you. All the doctoring, cooking and cleaning to allow me to work has been incredibly selfless and I really appreciate it. You are constantly driving me to improve.

Table of Content

1 Introduction

1.1 Motivation

It is estimated by the World Health Organization (2019) that over 30 million people currently suffer from rheumatic heart disease, predominantly affecting young patients with potentially long life expectancy. Patients needing surgical intervention and valve replacements are essentially offered two valve types; rigid mechanical or flexible bioprosthetic valves. Rigid mechanical valves exhibit superior valve durability, however, pose an elevated risk of thrombosis formation. Flexible bioprosthetic valves, in contrast, present a low risk of thrombosis formation but have been shown to suffer from valve fatigue and degradation.

To reduce long term patient risk and increase the standard of living of these patients, researchers are focusing on merging these valve advantages by developing flexible mechanical leaflets from polymeric materials.

This investigation provides essential tools to aid in the development of these potentially revolutionary heart valve leaflet materials.

1.2 Scope of Investigation

The investigation presented herein aims to enhance the understanding of polymers, by proposing a constructive stress-strain behaviour model. The proposed constructive model is primarily developed for thermoplastic polyurethane type polymers. This model covers the equilibrium stress-strain behaviour, the dependence on loading history and the rate-dependent viscous response observed in polyurethanes.

This investigation describes the design and development process of a multi-stationed micro tensile specimen fatigue tester, creating a tool to further assess materials on the basis of fatigue and durability. The developed fatigue tester's secondary function includes the ability to customise test waveforms.

The proposed model is herein compared to experimental data, assessing the model feasibility and accuracy. The experimental data is limited one material namely, Pellethane® 2363-80AE TPU.

The developed fatigue tester is compared to a commercial tensile tester to assess the accuracy and verify against the prescribed machine design specifications and validated in its primary function as a fatigue tester. The ability to customise test waveforms is also showcased within this report.

1.3 Report Outline

The literature review in **Chapter 2**, provides a brief overview of the challenges within current heart valve replacement technology. The fundamentals of polyurethane chemistry are briefly discussed to support the assumptions and conjectures made to develop the material model in **Chapter 3**. The literature review also describes the technology typically utilised in high accuracy oscillating systems, providing context to the machine design section in **Chapter 4**.

The experimental design presented in **Chapter 5**, describes the necessary methods to assess the proposed material model and the verification of the fatigue tester design. This chapter also provides a platform to discuss the results presented in **Chapter 6**.

Chapter 7, summarises the significant test results of both the model evaluation and fatigue tester verification and provides a conclusion thereon. Further model investigation and possible future fatigue tester improvements are discussed in the recommendations presented in **Chapter 8**.

The supplementing appendices attached at the end of the report provide detailed information where necessary, present all the design drawings and the machine control code as well as the model simulation scripts.

2 Literature Review

This chapter provides context on the current state of heart valve replacement, ultimately providing the motivation for this investigation. The essential background in polymers and the chemistry fundamentals thereof is reviewed to provide the basis to further develop a thermoplastic polyurethane stress-strain behaviour model. Technology in both the mechanical and electronic spheres pertaining to fatigue testing is discussed herein, creating a platform from which to suitably design a fatigue tester.

2.1 Heart Valves

According to Maganti et al. (2010) valvular heart disease or (VHD) predominantly occurs due to one of the following causes:

1. Degenerative valve diseases
2. Calcification due to ageing
3. Rheumatic heart disease (RHD)
4. Congenital abnormalities
5. Bacterial endocarditis

Congenital abnormalities and Rheumatic Fever often become a problem at very young ages. In fact Zaman et al. (1998) suggested that in developing countries the average age of diagnosing Rheumatic fever is as young as 12.7 years, of which the majority have already experienced their first attack. Furthermore, the World Health Organization (2019) announced that up to 30 million people currently suffer from RHD, causing an estimated 305000 deaths a year, with similar predictions presented by Tibazarwa, Volmink & Mayosi (2008).

Young symptomatic RHD patients, where valve repair is not feasible, are offered surgically implanted mechanical or bioprosthetic valve replacements (Yau et al., 2000). Mechanical valves are superior in terms of valve durability and for this reason, guidelines advise that patients under the age of 60 receive a mechanical valve replacement (Head, Çelik & Kappetein, 2017). As discussed in Lim, Lloyd & Bhattacharyya (2017) mechanical valves are more prone to thrombus formation mostly due to the rigidity of mechanical valve leaflets. Therefore these patients are prescribed chronic anticoagulation medication which in itself presents many medical and logistical complication.

Musumeci et al. (2018) discusses these valve replacement solutions, emphasising the need for a durable flexible leaflet material alternative, addressing both thrombosis and valve durability with the ability to be percutaneously implanted. Musumeci et al. (2018) goes further to propose and discuss a polymeric type material for the flexible leaflet alternative.

2.2 Polymers

Polymers are large molecules with long molecular chains comprising of repeated units or monomers as described by Coleman and Painter (1998). They can be divided into two major groups namely thermoplastics and thermosets. Thermoplastic polymers are re-processable whereas cured thermoset polymers are irreversibly set in their shape. Polymer chemistry further categorises polymers according to the number of monomer types within the molecule, where homopolymers and copolymers represent single repeated monomer or multiple monomer types, respectively.

2.2.1 Crosslinking

The polymer's molecular chains can be interlinked forming a network structure. In typical elastomer thermosets, the molecular chains are interconnected through covalent bonds producing strong irreversible networks as described by Wittenberg et al. (2018). Freltas, Burgert and Stadler (1987) suggested that hydrogen bonds can also act to interconnect these long molecular chains. Wittenberg et al. (2018) continues by describing how these hydrogen bonds act as thermally reversible crosslinks. Temperatures in excess of 150 ^{o}C results in the total break down of hydrogen bonds as described by Czech et al. (2006).

2.2.2 Polymer Entanglement

Edwards and Vilgis (1988) proposed that the molecular chains are continuously wiggling in what is now referred to as the phenomenon of reputation. According to tube model theory developed by Edwards and Vilgis (1988), when neighbouring chains enter a defined space surrounding a molecular chain, many small interactions are experienced. The accumulation of these interactions can be viewed as temporary crosslinks.

2.2.3 Viscous Elastic Behaviour

Polymer materials typically exhibit both strain and strain-rate dependent stress response behaviour as suggested by Karam (1959), this is referred to as visco-elastic behaviour. Polymer melt viscosity is the resistance to shear flow and is a function of the shear rate as described in Polymerdatabase.com (2019).

2.2.4 Thermoplastic Polyurethane

TPU is a copolymer synthesised by reacting a dialchohol with a diisocyanate (Coleman and Painter, 1998). As described in Hepburn (1982) TPU's consist of phase separated hard and soft segments where the hard segments coagulate via hydrogen bonds to form non-covalent crosslinks (Petrovic and Ferguson, 1991). Figure 2.1 provides a visual representation of the polyurethane hard and soft segment separation.

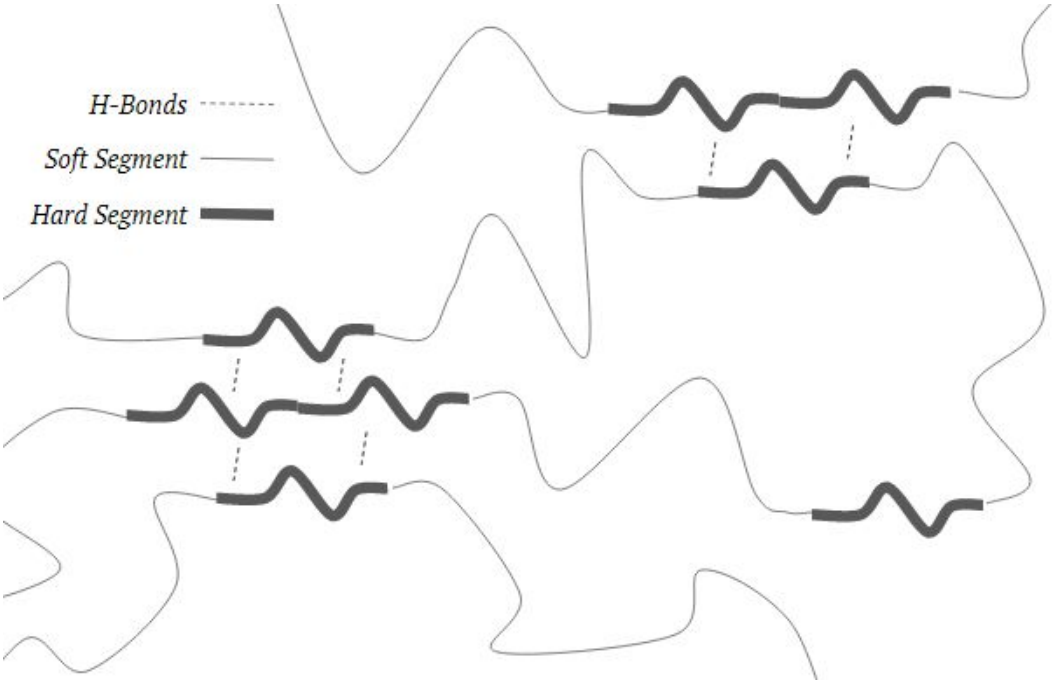

Figure 2.1: The phase separation of the hard and soft segment in polyurethanes.

When a hard segment is disassociated from other hard segment it acts as if it were soft segment, however, still maintaining the potential to reassociate to a cluster of hard segment. Figure 2.1 further presents how the hydrogen bonds act as crosslinks within one molecular chain and neighbouring chains.

2.2.5 Polymer Network Modeling

Kuhn and Grün (1942) provided a model for a single chain using the Langevin statistics to describe the chain energy function also capturing the chain extension limits. As presented in figure 2.2 Arruda and Boyce (1993) propose an 8-chain model relating macroscopic stretch to that experienced in each chain. This model accurately captures the non-Gaussian collective chain stress to an applied macroscopic strain. Eq 2.1 provides the strain energy function that is derived from this logic.

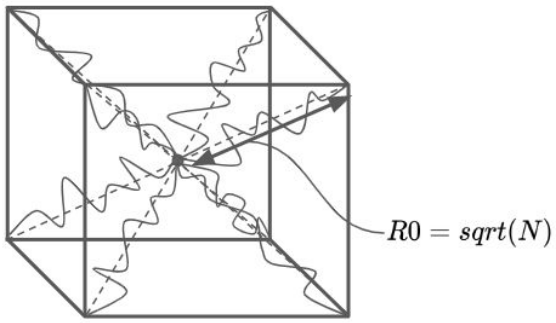

Figure 2.2: Arruda-Boyce 8 chain model.

$$U = \mu \cdot \left[\sqrt{N} \cdot \lambda_{chain} \cdot \beta + N \cdot ln(\frac{\beta}{sinh(\beta)})\right] \qquad \textit{Eq 2.1}$$

Where,

$$\mu = nk\theta \qquad \textit{Eq 2.2}$$

$$\beta = L^{-1}(\frac{\lambda_{chain}}{\sqrt{N}}) \qquad \textit{Eq 2.3}$$

Where μ is the modulus of the cross-linked network, in this case, the soft segment, n is the chain density, k is Boltzmann's constant and Θ is the absolute temperature. N is the number of monomers between crosslinks. λ_{chain} is the average stretch within the chains. L is the Langevin function, it is primarily used in statistically based models specifically describing polymeric networks, the inverse of which is most closely approximated by the function proposed by Jedynak (2017) presented by Eq 2.4.

$$L^{-1}(x) \approx \frac{x \cdot (3 - 1.00651 \cdot x^2 - 0.92251 \cdot x^4 + 1.47353 \cdot x^6 - 0.48952 \cdot x^8)}{(1-x) \cdot (1 + 1.01524 \cdot x)} \qquad \textit{Eq 2.4}$$

Following Qi and Boyce (2004), using the strain energy function presented in Eq 2.1 and the 8-chain model presented in figure 2.2 the stress-strain behaviour of vulcanised rubber or simple crosslinked networks can be accurately expressed as described in Eq 2.5:

$$\theta = \frac{\mu}{3} \cdot \frac{\sqrt{N}}{\lambda_{chain}} \cdot L^{-1}(\frac{\lambda_{chain}}{\sqrt{N}}) \cdot (\lambda^2 - \frac{1}{\lambda}) \qquad \textit{Eq 2.5}$$

Where λ is the macroscopic strain.

2.2.6 Polymer Failure Modes

In the context of heart valve material, it is important to note that there are various contributing and compounding factors affecting polymer failure. As described by Maxwell et al. (2005) there are 7 mechanisms of polymer failure, namely:

1. Fatigue
2. Thermal Ageing
3. Chemical Degradation
4. Creep
5. Environmental Stress Cracking
6. Biological Degradation
7. Weathering and Ionising Radiation

Polymer fatigue failure occurs when a specimen is subjected to cyclic loading and fails at a stress substantially lower than what can be endured under single loading conditions as described by Maxwell et al. (2005). Fatigue is generally studied by analysing the material's S-N curve, where S represents peak stress and N represents the number of cycles. As discussed by Janssen et al. (2008), Fatigue is particularly complex to predict, due to the nonisothermal conditions presented in practice, and thus require thermochemically coupled models to capture the energy dissipated per loading cycle.

2.3 Fatigue Testers

Material fatigue testers are machines designed to subject material specimens to cyclic loads whilst tracking the number of cycles, force response and extension. Fatigue tests are divided into two sections, either stress or strain-controlled. Stress-controlled tests are suitable for simulating applications where materials are subjected to cyclic forces. Whereas strain-controlled tests are better suited to cyclic displacement applications.

2.3.1 Cyclic Actuation

Fatigue testers require cyclic motion, depending on the specific test requirements, one of the following mechanisms is generally employed to achieve this motion:

- Servo-Pneumatic actuation
- Servo-Hydraulic actuation
- Ball screw rotational to linear motion conversion
- Roller screw rotational to linear motion conversion
- Linear Voice Coils
- Rack and pinions
- Belt drives

As shown by Huber, Fleck and Ashby (1997) Servo-pneumatic actuators are an effective alternative for high speed and moderate force outputs. Despite their cost-effectiveness, pneumatics exhibit poor position controllability, making them impractical for finely tuned applications as discussed in the Tolomatic, Inc. (2014) report.

Hydraulic systems possess extremely high power densities and are perfectly suited to applications where force and displacement are the predominant selection criteria as described by Huber, Fleck and Ashby (1997). Hydraulics exhibit improved repeatability and rigidity in comparison to pneumatics, however often are not fit for very finely tuned control applications as suggested in the Tolomatic, Inc. (2014) report.

As described by Lemire, Boni and Furnish (2007), ball lead-screws are a highly efficient rotation to linear motion converters, with efficiencies of up to 95%. They are also capable of being controlled at high frequencies and speeds. Lemire, Boni and Furnish (2007) states that ball screws can achieve positional accuracy ranging from 10 to 50 µm. Lemire, Boni and Furnish (2007) provides a typical life span distance value of 100 - 2500 km for ball lead-screws, this relates to 2 - 5 days of testing at a cyclic amplitude of 10 mm at a 30 Hz test frequency, highlighting the susceptibility to mechanical wear.

Roller lead screw systems share the same merits to that of ball lead screws, with the added advantage of a higher thrust capacity. According to Lemire, Boni and Furnish (2007), roller systems are typically 40% more expensive than ball lead screws.

As discussed by Chen, Fuh and Tung (2005), voice coils exhibit excellent controllability, speeds in excess of 2.5 m/s, high force density, sub-micron resolution and finally exhibit the lowest noise levels without any backlash or clogging. For these reasons voice coils are most suited to high-frequency use and therefore are often utilised in fatigue testing applications.

Rack and pinion mechanisms are commonly used in fatigue testers for load positioning feedback purposes, however, not often used for the application of the actual cyclic load actuation itself. As discussed in the Delphi Technologies Inc (1997) patent, when rotational encoders are coupled to the pinion and a light rack directly attached to the moving load, highly accurate positioning feedback becomes achievable.

Belts and pulley systems provide a simple mechanism to convert rotational to linear motion, however, belts are susceptible to stretching and are therefore limited in positioning accuracy and susceptible to mechanical drift as mentioned by Lemire, Boni and Furnish (2007).

2.3.2 Motion Control

Control system can be classed into open and closed-loop systems. Open-loop systems can be used for applications where the parameter variable *feedback* is *not* required, typically when the output objective is predictable and consistent. Conversely, closed-loop systems are able to handle varying output requirements due to continuous parameter variable feedback (positional feedback in this case).

Proportional-Integrative-Differential (PID) control is a widely used, tunable closed-loop control strategy, suited to fine responsive motor control. As described by Ang, Chong and Li (2005) PID systems continuously compare the set point to the actual position resulting in a

position error term. A system control variable u(t) is derived from the obtained error value e(t) according to Eq 2.6 (Mueller, 2011).

$$u(t) = K_p \cdot e(t) + K_i \cdot \int_0^t e(t') \cdot dt' + K_d \cdot \frac{de(t)}{dt} \qquad \textit{Eq 2.6}$$

Where K_p, K_i and K_d are the proportional, integration and differentiation coefficients respectively. Figure 2.3 provides a block diagram describing how these functions theoretically determine the control variable.

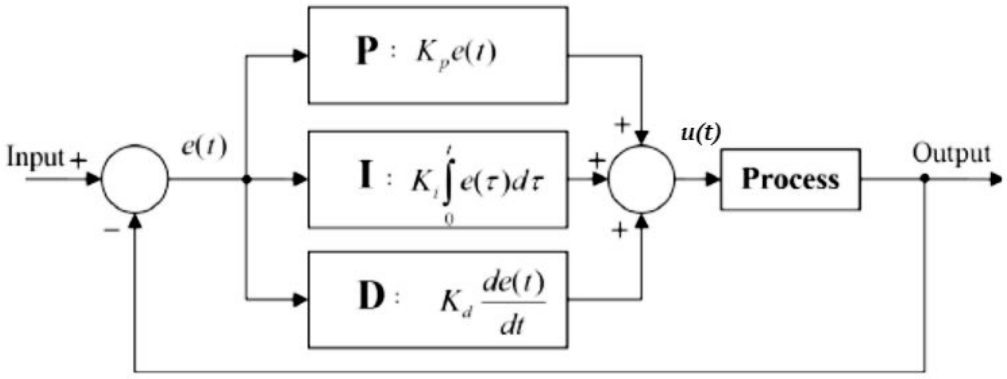

Figure 2.3: The method of proportional, integrative and differentiative control, reprinted from Mueller (2011).

Typically controllers are equipped with externally adjustable potentiometers to set the PID coefficients for application-specific tuning. Figure 2.4 presents how PID circuits practically achieve this using op-amps. Note how resistor adjustment can act as scaling coefficients.

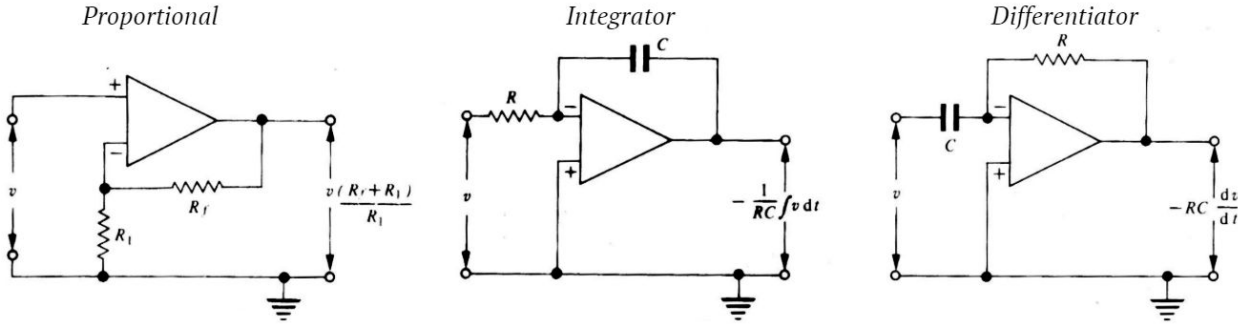

Figure 2.4: The electronic circuits performing the proportional, integrative and differentiative functions, reprinted from Jones (1995).

2.3.3 Displacement Sensing

As discussed for control systems the feedback loop is essential for finely tuned motion control. As presented by Nyce (2019) position feedback can be achieved through various types of displacement sensors:

- Resistive
- Inductive
- Capacitive
- Piezoelectric
- Laser
- Hall effect
- Optical encoder

Optical encoder sensors have the advantage of a digital feedback signal which is particularly useful when used in environments with high signal noise (Vaseghi, 2000). As the name suggests optical encoders function by optically identifying visual makers on the moving component, these markers can be arranged to provide an extremely high positional resolution (Dynapar.com, 2019). As described by Mayer (1994), to digitally increase resolution, two optical sensors can be offset to sense the optical markers on separate channels, typically 180 degrees out of phase from one another. As presented in figure 2.5 by identifying the raising and falling edge of both channel A and B results in a positional resolution 4 times that of the marker resolution. It is also important to note that with two channels the encoder displacement becomes directional which is essential for oscillating motion tracking (Mayer, 1994).

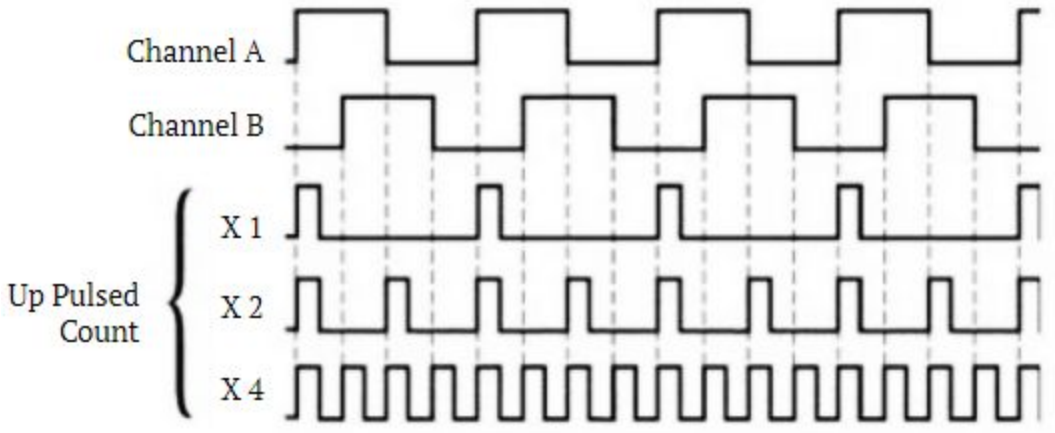

Figure 2.5: *The signal resolution obtained from dual-channel sensing in quadratic encoders.*

2.3.4 Force Sensing

As described by PCB Group (2019) there are a number of methods to measure force, the most common of which are listed below:

- Capacitive
- Inductive
- Piezoelectric
- Strain gauge

As discussed by Brei (2019), Capacitive and Inductance type pressure sensors are suitable for force sensing when in conjunction with appropriate mechanical hardware. Typically capacitive or inductance type pressure transducers are coupled with hydraulic or pneumatic pistons, measuring pressure which is then converted to load.

The piezoelectric material produces a charge Q proportional to the load applied to the material as described by Keim (2018). The charge is converted to voltage as described by Eq 2.7, where the output voltage is proportional to the rate of change in charge and therefore the rate of change in load.

$$V_{output} = \frac{1}{C} \cdot \int \frac{dQ}{dt} \cdot dt \qquad \textit{Eq 2.7}$$

Due to the voltage output's load rate dependence, piezo-based sensors are not suitable for steady-state measurement unless coupled with an integrator circuit as presented in figure 2.4 earlier in this chapter (Keim, 2018).

The electrical resistance of a strain gauge changes proportionally according to the mechanical strain subjected to the strain gauge itself. When attached to a material with a predictable stress-strain relationship, the deforming load can be determined from the voltage drop over the proportional strain gauge resistance.

Load cells typically utilise the Wheatstone bridge configuration which assists in the measurement of very small changes in resistance (Ekelof, 2001). S-type load cells incorporating strain gages in the Wheatstone bridge configuration are well suited to accurately capture both tensile and compressive loads. It is important to consider the fatigue life of the load cell's mechanical structure in oscillating applications (PCB Group, 2019).

2.3.5 Signal Conditioning

Analogue signals require analogue to digital conversion before processing. Analogue signals typically consist of very small voltage fluctuations which result in poor analogue to digital conversion resolutions. Therefore these low voltage signals are typically proportionally

amplified before processing using op-amp circuits as presented in figure 2.4 earlier in this chapter (Jones, 1995). Lower voltage signals are more susceptible to noise and therefore it is advised to filter the signal before digital processing. This is typically achieved using lowpass filters to reduce or eliminate all the unwanted high-frequency noise (Jones, 1995).

In some applications, it is useful to condition digital signals before processing, unlike the analogue signals, this does affect the signal itself but rather how the data being transmitted is ordered for processing. For example, the constantly chaining quadrature encoder step signal would require constant sampling from a processing unit to avoid missing a single step. As described by Cypress Semiconductor Corporation (2010) integrating a quadratic decoder before signal processing, converts the encoded signals into a continuously updated digital register, which can easily be independently accessed at any time by a processing unit. With this method the encoder step signal is continuously sampled independently, without consuming the computing power of your processing unit.

3 Material Model

This chapter starts by developing a geometric translation from macroscopic stretch to individual chain stretch, also describing how the chain stretch amplification factor is derived. The current theory on thermoplastic polyurethane softening is briefly reviewed. From this base theory, an equilibrium stress-strain behaviour model modification is proposed whereby the number of monomers between crosslinks is also suggested to evolve with strain. The proposed model is structured to incorporate loading history as described by Mullins (1969). Thereafter the model is further constructed to account for the strain rate dependence observed in thermoplastic polyurethanes, ultimately unifying the equilibrium and viscous stress-strain behaviour into a single model. Furthermore, the conjecture of streamlining is introduced proposing an unconventional dependence on loading history with respect to the viscous aspect of the stress-strain behaviour.

This chapter is largely based on the work conducted by Kuhn and Grün (1942) on the strain energy density of polymeric chains and the 8-chain constructive model supplied by Arruda and Boyce (1993) to apply the strain energy function to polymer chain networks. Mullins and Tobin (1966) worked on the inclusion of fillers to the polymer network. These fillers are assumed to provide an insignificant contribution to strain but rather amplify the chain stretch in the rest of the polymer network. As described by Mullins and Tobin (1966) this amplified chain stretch is observed to reduce with an increase in macroscopic strain. Later on Mullins (1969) theorised that the softening of the material results from the break-up of the hard fillers thus increasing the effective soft segment volumetric fraction within the network. Qi and Boyce (2005) extend this theory to thermoplastic polyurethanes, where the polyurethane hard segment acts as both fillers and cross-links that too experience softening during macroscopic strain.

3.1 Filled Network Model

This section presents the geometrically derived macroscopic stretch to chain stretch transform within the 8-chain model framework. After which it describes the stretch amplification factor incorporated for filled polymer networks.

3.1.1 Geometric Chain Stretch Derivation

The chain stretch λ_{chain} is typically derived from stretch invariants as used and described by Arruda and Boyce (1993). For improved visualization and model understanding, the λ_{chain} is derived geometrically in this report. Consider the representative 8-chain volume as described in the literature review, upon uniaxial macroscopic strain the chain stretch λ_{chain} is proportional to the change in diagonal lengths as presented in figure 3.1, and described in Eq.3.1.

$$\lambda_{chain} = \frac{DL_1}{DL_0} \qquad \textit{Eq.3.1}$$

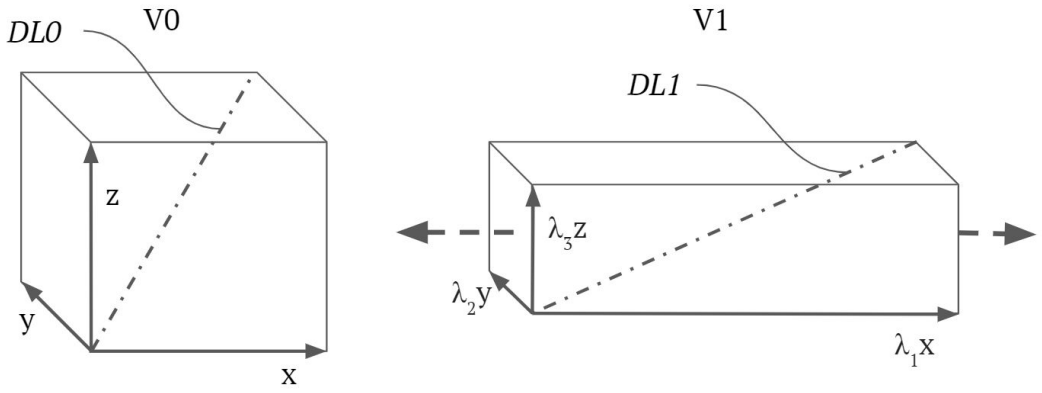

Figure 3.1: The macroscopic uniaxial stretch effects on the 8-chain model diagonal chain length.

The representative volume can be expressed as described in Eq.3.2 and Eq.3.3 for the initial and stretched state respectively.

$$V_0 = x \cdot y \cdot z \qquad \textit{Eq.3.2}$$

$$V_1 = \lambda_1 x \cdot \lambda_2 y \cdot \lambda_3 z \qquad \textit{Eq.3.3}$$

Assuming material incompressibility, the representative volume is conserved during the induced strain. From figure 3.1 x, y and z are unit vectors, describing the initial dimensions of the representative volume. λ_1, λ_2 and λ_3 are scaling factors representing the degree of stretch in the corresponding directions.

$$V_0 = V_1 \qquad \textit{Eq.3.4}$$

$$x \cdot y \cdot z = \lambda_1 x \cdot \lambda_2 y \cdot \lambda_3 z \qquad \textit{Eq.3.5}$$

$$1 = \lambda_1 \cdot \lambda_2 \cdot \lambda_3 \qquad \textit{Eq.3.6}$$

Assuming an isotropic structure, the deformation in the y and z-direction is equal during uniaxial loading in the x-direction.

$$\lambda_2 = \lambda_3 \qquad \textit{Eq.3.7}$$

Substituting equation Eq.3.7 into Eq.3.6.

$$1 = \lambda_1 \cdot \lambda_2^2 \qquad \textit{Eq.3.8}$$

$$\lambda_2^2 = \frac{1}{\lambda_1} \qquad \textit{Eq.3.9}$$

Using simple geometry the diagonal length of both the original cube and stretched cube is calculated as follows.

$$DL_x = \sqrt{x^2 + y^2 + z^2} \qquad \textit{Eq.3.10}$$

$$DL_0 = \sqrt{3} \qquad \textit{Eq.3.11}$$

$$DL_1 = \sqrt{\lambda_1{}^2 + \lambda_2{}^2 + \lambda_3{}^2} \qquad \textit{Eq.3.12}$$

Substituting Eq.3.7 into Eq.3.12.

$$DL_1 = \sqrt{\lambda_1{}^2 + 2\lambda_2{}^2} \qquad \textit{Eq.3.13}$$

Substituting Eq.3.9 into Eq.3.13.

$$DL_1 = \sqrt{\lambda_1{}^2 + \frac{2}{\lambda_1}} \qquad \textit{Eq.3.14}$$

The average stretch per chain upon macroscopic stretch is calculated by substituting Eq.3.11 and Eq.3.14 into Eq.3.1.

$$\lambda_{chain} = \frac{\sqrt{\lambda_1{}^2 + \frac{2}{\lambda_1}}}{\sqrt{3}} = \sqrt{\frac{1}{3} \cdot (\lambda_1{}^2 + \frac{2}{\lambda_1})} \qquad \textit{Eq.3.15}$$

3.1.2 Chain Stretch Amplification

It is assumed that only the soft segment is responsible for strain. Due to the volume-occupying fillers, the stretch experienced within the soft segment is amplified. This notion was first proposed by Mullins and Tobin (1957) specifically for the fillers in vulcanised rubbers. More recently Bergstrom and Boyce (1999) proposed the expression for stretch amplification X which is dependant on both the composite dispersion and the volume fraction of fillers as presented in Eq.3.16.

$$X = 1 + 3.5 \cdot v_H + 18 \cdot v_H{}^2 \qquad \textit{Eq.3.16}$$

Following Mullins and Tobin (1957) in determining the amplified chain stretch.

$$\Lambda_{chain} = 1 + X \cdot (\lambda_{chain} - 1) \qquad \textit{Eq.3.17}$$

Substituting Eq.3.15 into Eq.3.17, the amplified stretch Λ_{chain} can be expressed in terms of macroscopic stretch λ_1, expressed simply as λ for a uniaxial stretch, as presented in Eq.3.18.

$$\Lambda_{chain} = 1 + X \cdot \left(\sqrt{\tfrac{1}{3} \cdot \left(\lambda^2 + \tfrac{2}{\lambda}\right)} - 1\right) \qquad \textit{Eq.3.18}$$

As described by Qi and Boyce (2004) the stress-strain behaviour of filled polymer networks can be expressed using Eq.3.19, where the standard polymer network model is adapted by substituting λ_{chain} with Λ_{chain} and scaling the stress response by the soft segment volume fraction v_s and the amplification factor X (Arruda and Boyce, 1993).

$$\theta = \frac{\mu \cdot v_s \cdot X}{3} \cdot \frac{\sqrt{N}}{\Lambda_{chain}} \cdot L^{-1}\left(\frac{\Lambda_{chain}}{\sqrt{N}}\right) \cdot \left(\lambda^2 - \tfrac{1}{\lambda}\right) \qquad \textit{Eq.3.19}$$

3.2 Thermoplastic Polyurethane Model

As discussed in the literature review, the polyurethane hard segment held together by hydrogen bonds act as the network crosslinks. Petrovic and Ferguson (1991) proposed that the hard segment of polyurethanes can occupy significant volume and therefore be thought of as stiff fillers. Therefore Qi and Boyce (2005) proposed applying the filled polymer network model to that of TPU's.

3.2.1 Strain Softening

In the case of polyurethanes, the evolution of hard to soft segment is a result of connecting chains reaching their maximum stretch $\lambda_{chain\text{-}lock}$ during uniaxial loading. This disassociates the weaker hydrogen bonds that hold the hard segment together thus increasing the percentages of soft segment. As described by Flory (1949) the average unstrained polymeric chain has an end to end distance proportional to the square root of the average number of monomers per chain, as presented in Eq.3.20.

$$R_0 = b \cdot \sqrt{N} \qquad \textit{Eq.3.20}$$

Where b is the size of the monomers and N is the number of monomers in the chain between crosslinks. Therefore the straightened length, as represented in figure 3.2, is determined using Eq.3.21.

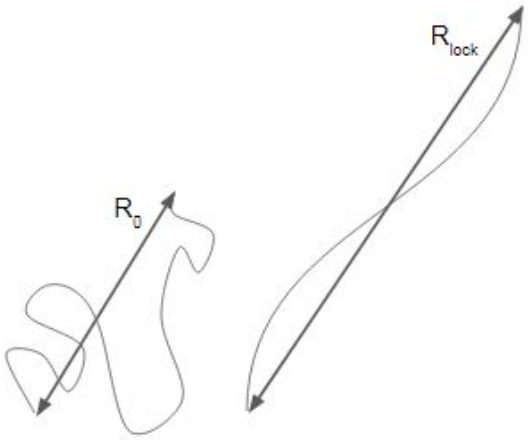

Figure 3.2: Stretch chain length lockout.

$$R_{lock} = b \cdot N \qquad \textit{Eq.3.21}$$

The $\lambda_{\text{chain-lock}}$ is the stretch ratio from R_0 to R_{lock}.

$$\lambda_{chain}^{lock} = \frac{R_{lock}}{R_0} \qquad \textit{Eq.3.22}$$

Substituting Eq.3.20 and Eq.3.21 into Eq.3.22 provides the expression for the lockout chain stretch,

$$\lambda_{chain}^{lock} = \sqrt{N} \qquad \textit{Eq.3.23}$$

Miehe and Keck (2000) suggested that the changing soft segment follows saturation type evolution where v_{ss} represents the soft segment saturation volume fraction. Following Qi and Boyce (2004), the soft segment evolves as follows,

$$v_s = v_{ss} - (v_{ss} - v_0) \cdot exp(-A \cdot \frac{\Lambda_{chain}^{-1}}{\lambda_{chain}^{lock} - \Lambda_{chian}}) \qquad \textit{Eq.3.24}$$

Where A characterises the evolution of v_s.

3.2.2 Proposed Softening Model

It is proposed that the softening effect is not exclusively a function of soft segment volume fraction evolution but includes the simultaneous evolution of the number of monomers between crosslinks N. The number of monomers between crosslinks is representative of the length of the chain between crosslinks as described in Eq.3.21. Consider two finitely long polymer chains, where each hard segment is assumed to be associated with the corresponding

chain's hard segment as presented in figure 3.3. For analytical purposes, figure 3.3 is drawn representing the average lengths of both the hard and soft segment, in reality, these lengths will vary around the average length.

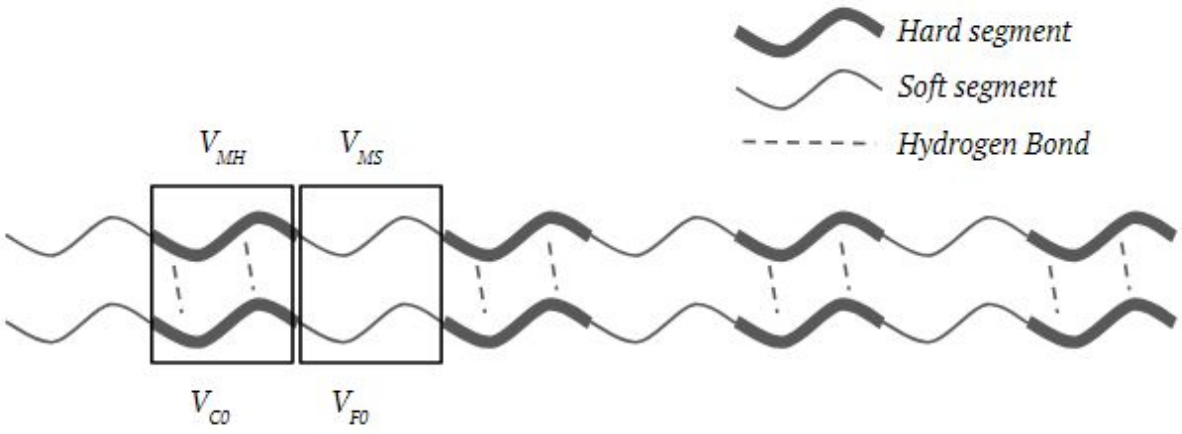

Figure 3.3: *Visual description of the soft segment volume fraction's relation to the material composition ratio.*

In this initial unstrained state, the volume fraction of the soft (free) and hard (constrained) segment can be assumed to be equal to the hard and soft chemical weight composition ratio.

$$\frac{V_{F0}}{V_{C0}} = \frac{V_{MH}}{V_{MS}} \qquad \textit{Eq.3.25}$$

Where the V_{FO} and V_{CO} represent the free and constrained volumetric fractions, respectively. While the V_{MH} and V_{MS} represent the chemical composition ratio of hard to soft segment, respectively. Similarly, the ratio between the free and constrained chain length can be considered proportional to that of the chemically mixed ratios.

$$\frac{L_{CO}}{L_{FO}} = \frac{V_{MH}}{V_{MS}} \qquad \textit{Eq.3.26}$$

Where L_{F0} and L_{C0}, represent the free and constrained chain length, respectively. The resultant soft volume fraction V_S segment can be calculated as follows.

$$V_S = \frac{V_F}{V_F + V_C} \qquad \textit{Eq.3.27}$$

Consider a second state where induced strain has partially broken up the hard segment, reducing the crosslinking density. Figure 3.4 depicts a factor two reduction in crosslink density represented by removing every second hydrogen bond. Recall that *dissociated* hard segment act as soft segment, therefore contributing to the free chain length.

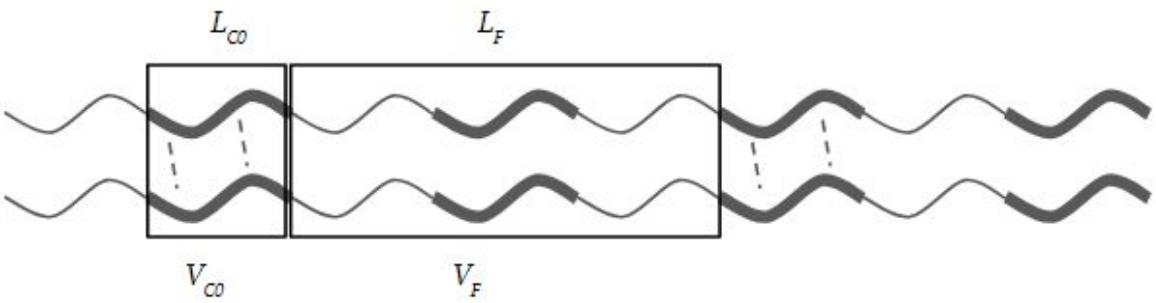

Figure 3.4: The evolution of the free chain length.

As the hydrogen bonds break, the soft segment increases towards a soft segment saturation or total conversion of hard to soft segment (V_S = 1), while the total *free* chain length approaches the full finite chain length. From figure 3.4 it can be shown that as the soft segment fraction increases so too does the free chain length, suggesting a linear relationship. To be compatible with the strain energy function in Eq.3.19, the chain length is expressed in terms of a number of monomers as suggested in the previous section. figure 3.5 describes this linear relationship where the number of monomers between hydrogen bond crosslinks evolves with the evolving soft segment volume fraction from an initial state to a saturation state.

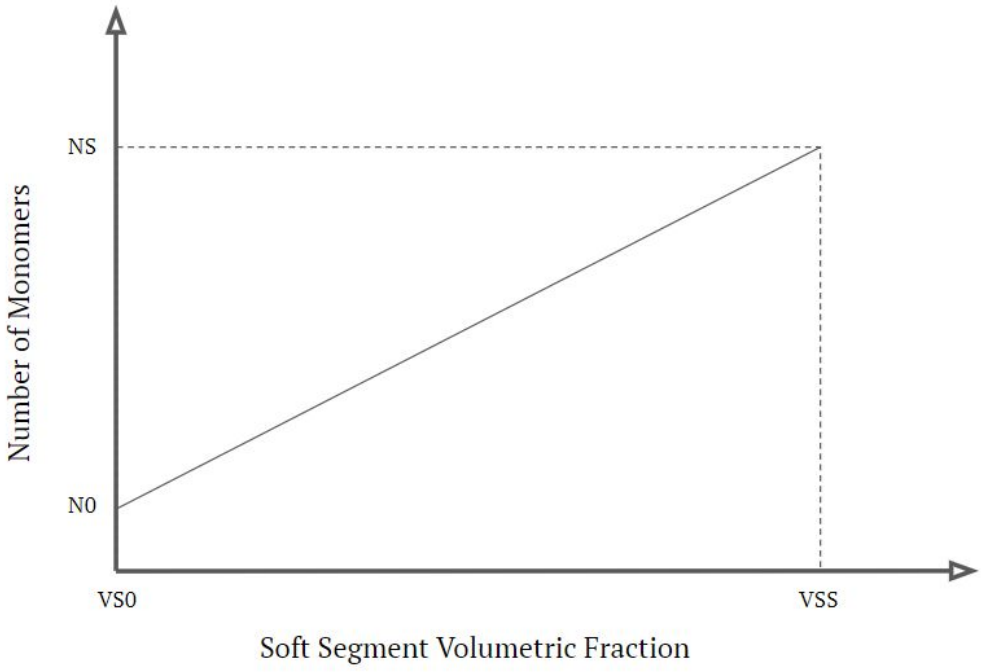

Figure 3.5: *The predicted linear relationship between the number of monomers between crosslinks and the soft segment volumetric fraction within a polyurethane network.*

From figure 3.5, Eq.3.28 can be created to determine the number of monomers between crosslinks while the soft segment fraction evolves during macroscopic strain.

$$N = \frac{N_S - N_0}{V_{SS} - V_{S0}} \cdot V_S + \left(N_0 - \frac{N_S - N_0}{V_{SS} - V_{S0}} \cdot V_{S0}\right) \qquad \textit{Eq.3.28}$$

Where N, N_S and N_0 are the current, saturation and the initial number of monomers between crosslinks respectively, while V_S, V_{SS} and V_0 are the current, saturation and the initial soft segment volumetric fractions respectively.

Figure 3.6 provides a graphical representation of the feedback system where the uniaxial stress is predicted with regard to a macroscopic stretch/strain. This graphic displays which dependent contributing factors interact with each other during the extension of the polyurethane-like network. The connecting arrows provide the direction of dependence from one aspect to another.

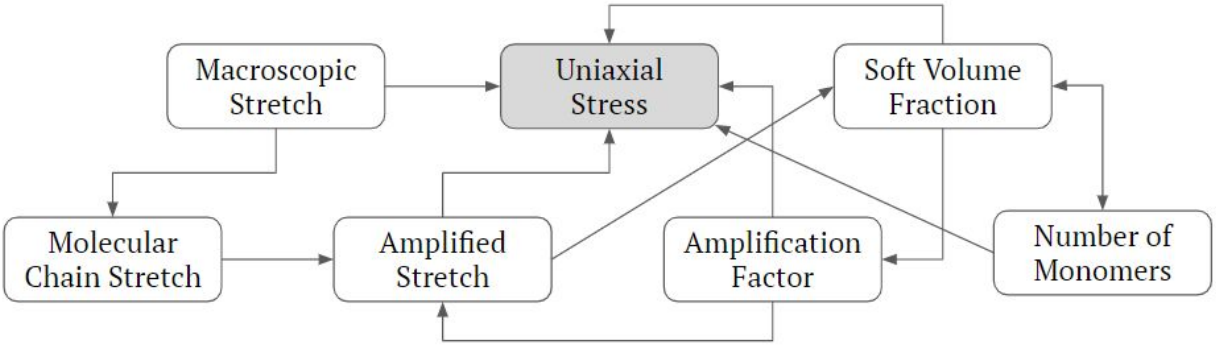

Figure 3.6: The dependencies of functions to predict the stress-strain behaviour in polyurethane-like networks.

3.2.3 Loading History

Estes, Seymour and Cooper (1971) discovered that after loading the decomposed hard segment showed very little recovery. Therefore during cyclic loading at negligible strain rates, no additional softening occurs until the previously experienced maximum strain is surpassed. As described in the previous subsection, the number of monomers between crosslinks evolves with the soft segment fraction. Therefore it is proposed that the number of monomers between crosslinks is also dependant on the specimen's loading history and assumes the value at the previously experienced maximum strain. Once the previously experienced maximum strain is surpassed the model is set up to predict the stress-strain response, independent of its loading history.

The hard segment break up would however create a new minimum state of entropy upon specimen relaxation. This accounts for the residual strain observed after polyurethane like networks are significantly strained. This proposed model currently does not account for a new equilibrium and therefore does not capture the residual strain typically observed.

3.3 Viscous Effect

Qi and Boyce (2005) continue to describe the rate dependent or viscous aspect of the stress-strain behaviour by using a viscoplastic dashpot. This is achieved by separating the equilibrium and the rate dependent responses, viewing the two independently, the sum of which represents the combined response. This approach fails to account for the continuous physical interdependence of the equilibrium and rate dependent interactions.

3.3.1 Proposed Viscous Model

Further incorporating the theory of polymer chain entanglement described by Edwards and Vilgis (1988) into the proposed equilibrium stress-strain behaviour model, has the potential to simultaneously capture both the equilibrium and rate dependent stress-strain response.

Consider a polyurethane above its glass transition temperature; the soft segment essentially acts as a fluid whilst still slightly topologically restricted by the hydrogen bonded hard segment acting as crosslinks. As described by Nakayama (2018) for Newtonian fluids, the shear stress within a fluid is proportional to the strain rate between the particles as presented in *Eq.3.29*.

$$\tau = \mu \cdot \frac{du}{dy} \qquad \textit{Eq.3.30}$$

Where τ is shear stress, μ is the fluid viscosity and du/dy is the velocity gradient. Applying this to the soft segment of polyurethane, the average velocity gradient can be seen as equivalent to the average difference in chain velocity. Assuming the average difference in chain velocity is directly proportional to that of the strain rate, Eq.3.31 can be adapted to incorporate the macroscopic strain rate.

$$\tau \sim \mu \cdot \varepsilon / s \qquad \textit{Eq.3.31}$$

As discussed in the literature review, it is understood that long polymeric chains interact with one another, these accumulative interactions can be seen as effective crosslinks as proposed by Edwards and Vilgis (1988) and presented in figure 3.7.

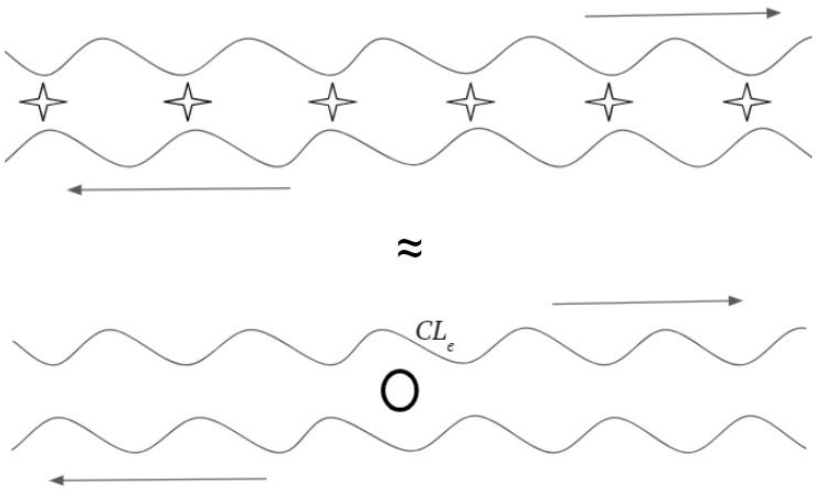

Figure 3.7: *The accumulative interactions combined as one effective crosslink.*

The sum of these shear stress interactions can be likened to entanglement interactions or effective crosslinks, therefore additional effective crosslinks due to strain rates can be expressed as follows.

$$CL_e \sim \mu \cdot \varepsilon/s \qquad \textit{Eq.3.32}$$

Where CL_e is the crosslink density resulting from rate dependant entanglement interactions, ε /s is strain rate and μ is the "fluid" viscosity. For strain rates incurring negligible temperature change the soft segment viscosity μ is assumed to be constant, therefore Eq.3.32 can be represented as Eq.3.33 where B is scaling constant.

$$CL_e = B \cdot \varepsilon/s \qquad \textit{Eq.3.33}$$

For the purpose of this conjecture, hard segment produced crosslinks and the rate independent topological entanglements are consolidated and referred to as CL_x. The total instantaneous crosslink density is equal to the sum of the crosslinks presented in equilibrium and the rate dependent entanglement interactions.

$$CL = CL_x + CL_e \qquad \textit{Eq.3.34}$$

Consider figure 3.7 again, with two adjacent free chains of a defined length. Upon relative motion, the effective resultant crosslinks reduce the free chain length and therefore proportionally decreases the number of monomers between crosslinks. It is defined that at strain rates approaching infinity the effective chain interactions saturate, approaching the maximum possible interactions. The inversely proportional number of monomers between crosslinks subsequently also approaches a finite saturation value. Furthermore, at negligible

strain rates the free chain length or number of monomers between crosslinks should remain unchained. Therefore the expression describing the effect of strain rate on the number of monomers between crosslinks is developed and presented in Eq.3.35.

$$N_{Effective} = N_{min} + (N - N_{min}) / (B \cdot \varepsilon/s + 1) \qquad Eq.3.35$$

Where $N_{Effective}$, N_{min} and N represent the effective, minimum saturation value and actual average number of monomers between crosslinks respectively. ε /s represents the strain rate, while B characterises the degree of the material's strain rate dependence. *Figure 3.8* describes how the effective number of monomers between crosslinks is affected by the strain rate, where $N_{Effective}$ tends towards N as the strain rate approaches zero, and as the strain rate approaches infinity the $N_{Effective}$ tends towards N_{min}.

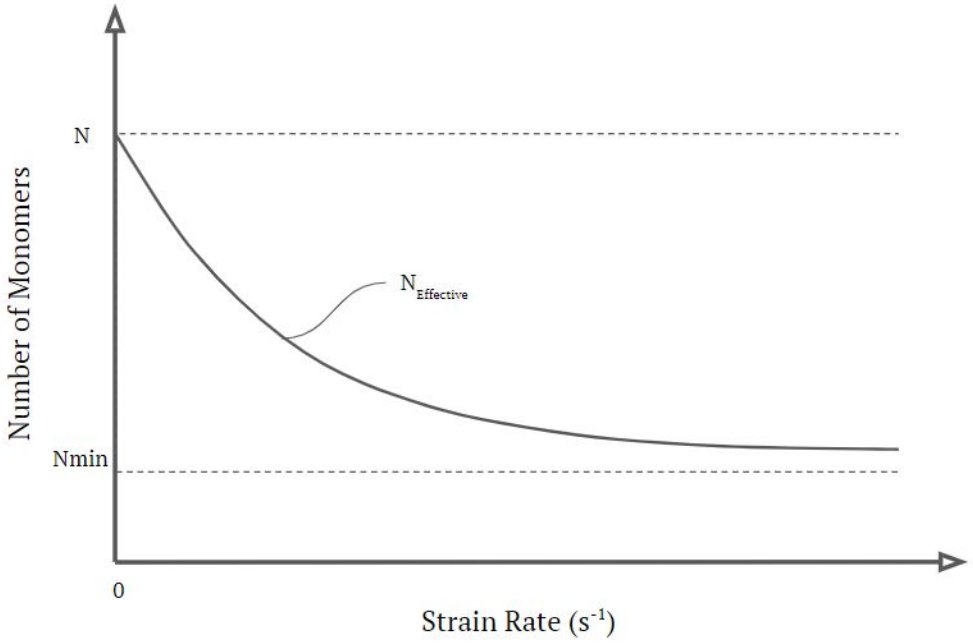

Figure 3.9: *The resultant effective number of monomers between crosslinks as a function of strain rate.*

3.3.3 Streamlining Conjecture

Viscous behaviour such as air resistance typically shows no dependence on actuation history. The surrounding particles are able to quickly return to an isotropic state of equilibrium after disturbance, erasing all evidence of the disturbance in a matter of seconds. The viscous time scales of the larger particles like that of polyurethane networks take much longer to return to a state of equilibrium. For long molecular chains that exhibit significant steady-state entanglement, it is proposed due to the inability to fully re-entangle, that the rate dependent interaction exhibit a dependence on the loading history. Considering this conjecture to be true the rate dependent scaling factor B would be required to evolve with subsequent loading cycles.

Although the viscous interactions may be reduced they cannot be eliminated, therefore a saturation type decomposition for B is proposed. The proposed expression for B is presented in Eq.3.36.

$$B = B_0 - (B_0 - B) \cdot (1 - \frac{1}{1+N_{cycle}}) \qquad \textit{Eq.3.36}$$

Where B_0 is the initial value for B, B_{sat} is the saturation asymptote for B and N_{cycle} is the number of loading cycles. Note, when ($N_{cycle} = 0$), ($B = B_0$) and as ($N_{cycle} \rightarrow \infty$), ($B \rightarrow B_{sat}$).

4 Machine Design

The micro-tensile specimen fatigue tester is designed primarily to fulfil the fatigue testing requirements to further investigate applicable material durability properties, secondarily the system provides a platform for the machine operator to create their own custom tests outside the scope of fatigue testing. For this reason, the hardware is intentionally selected to be over-specified in aspects related to desirable additional custom features while the software is structured to easily incorporate new testing regimes within the machine capabilities. The machine is designed to be a tool for understanding and testing the stress-strain behaviour of polyurethanes and new heart valve leaflet appropriate materials. This section elaborates on the full arsenal of the machine, highlighting the major mechanical, electronic hardware and software design considerations.

4.1 Machine Requirements

The machine's summarised user needs are listed in table 4.1 with the corresponding design inputs presented adjacently. Operating primarily as a fatigue tester, the machine also incorporates the capability for custom experimental test design, these additions to the core user needs will be discussed separately within the appropriate section.

Table 4.1: User needs and implied requirements thereof for the fatigue testing machine.

User needs	**Implied requirements**
Stress-Strain behaviour acquisition	➢ Force recording, load cells ➢ Displacement recording, linear encoder ➢ Strain-controlled actuation, voice coil and driver
Stand-alone machine (can function without a computer)	➢ An onboard control system, 2 x Arduino Due ➢ Built-in GUI, LCD screens and push buttons ➢ Onboard data storage, SD card
Environmental control	➢ Chemically resistant glass fluid bath ➢ Stainless steel submersible clamps ➢ Heating pad and temperature controller, 23 to 50 ^{o} C
Variable test parameter selection	➢ Frequency, 0 to 20 Hz ➢ Amplitude, 0.1 to 6 mm ➢ Waveform, Triangular, Square or Sinusoidal
Multiple sample test stations	➢ 12 testing stations ➢ Individually adjustable pretension ➢ Selectable recording

4.2 Mechanical Design

This section describes the mechanical design considerations presenting the holistic concept rationale, covering the important detailed aspects thereof and including the design calculations required to refine these mechanical selections.

4.2.1 Overview

Refer to the concept design represented in figure 4.1. The rig is made up of a solid base plate with 4 vertical support rods stemming from it. Three platforms are attached to the vertical rods, namely the height adjustable environmental platform, the sensor supporting platform and the actuator supporting platform.

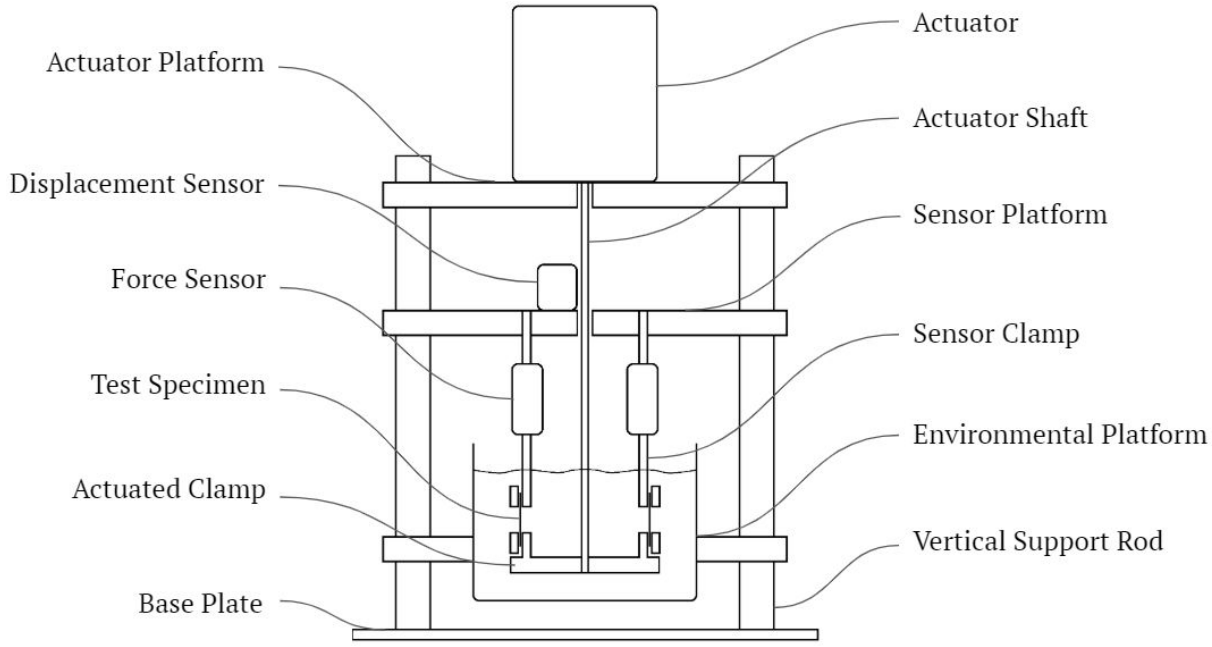

Figure 4.1: The basic mechanical concept.

The structural arrangement presented in figure 4.1 was selected to omit the need for dynamic seals, allowing the actuated clamps to be driven from above. The machine operates by stretching the test specimen in between the actuator and sensor clamps as the actuation shaft is driven up and down by the actuator, the force is transmitted through the specimen's specific force sensor while a single displacement sensor monitors the movement of the actuation shaft. The actuator shaft's displacement is equivalent to that of all the test specimen, therefore it is possible to obtain the force-displacement or stress-strain behaviour of the test specimens.

4.2.2 Actuator Selection

A linear actuator was chosen to reduce mechanical complexity, omitting the need for couplings and cams. A voice coil type actuator was selected on account of its speed and control versatility. The specific voice coil was selected on the basis of stroke length, maximum continues force and power, and peak force output.

The machine is designed to test specimens produced according to the ASTM D1708 – 13 (Tensile Properties of Plastics by Use of Microtensile Specimens). The working length of these specimens is 22 mm. The fatigue tester user need specifies a maximum cyclic amplitude of 0 to 6 mm, to accommodate future custom tensile tests a stroke corresponding to 50% strain is designed for (11 mm).

The specified continuous force needs to be in excess of the required root mean square (RMS) of the total force, the required root mean squared force is calculated for a sinusoidal waveform. The total force is equal to the sum of the force to accelerate the mass, stretch the specimens and overcome gravity.

$$F_{total} = F_{mass} + F_{stretch} + F_{Gravity} \qquad Eq.4.1$$

The sinusoidal testing displacement curve is described by Eq.4.2.

$$x = \frac{x_{max}}{2} - \frac{x_{max}}{2} \cdot cos(\omega \cdot t) \qquad Eq.4.2$$

Where x is displacement, x_{max} is the peak of the displacement curve, t is time per cycle and where,

$$\omega = 2\pi \cdot f \qquad Eq.4.3$$

Where f is the cycle frequency. The velocity curve described by Eq.4.4 is equal to the first derivative of the displacement curve with respect to time.

$$\frac{\partial x}{\partial t} = \frac{x_{max}}{2} \cdot \omega \cdot sin(\omega \cdot t) \qquad Eq.4.4$$

The acceleration curve described by Eq.4.5 is equal to the second derivative of the displacement curve with respect to time.

$$\frac{\partial^2 x}{\partial t^2} = \frac{x_{max}}{2} \cdot \omega^2 \cdot cos(\omega \cdot t) \qquad Eq.4.5$$

Force resulting from mass acceleration is defined according to Newton's second law.

$$F_{mass} = m \cdot \frac{\partial^2 x}{\partial t^2} \qquad Eq.4.6$$

Where the total moving mass is the sum of the moving coil assembly, the actuator shaft and the actuated (bottom) clamps. Where the actuator shaft and bottom clamps have a combined mass of 0.5 kg.

Substituting Eq.4.5 into Eq.4.6, the force resulting from mass acceleration can be calculated as follows in Eq.4.7

$$F_{mass} = \; m \cdot \frac{x_{max}}{2} \cdot \omega^2 \cdot cos(\omega \cdot t) \qquad Eq.4.7$$

The force contribution from the stretching of the test specimen calculation assumes the test specimen's M50 to be a maximum of 9 MPa, which is significantly over the proposed limit of adequate moduli for flexible heart valves. Assuming a simplified linear stress response to strain, following Eq.4.2 for the displacement cure the stress can be derived as described in Eq.4.8

$$\sigma = \frac{M50}{2} - \frac{M50}{2} \cdot cos(\omega \cdot t) \qquad Eq.4.8$$

The cross-sectional area of the test specimen is 4 mm^2 as prescribed by ASTM D1708 (0.8 thick by 5 mm wide). The force per specimen is equal to the stress by cross-sectional area, there are 12 stations for simultaneous testing, therefore the total force required for cyclic testing is expressed by Eq.4.9.

$$F_{stretch} = 12 \cdot A_{CS} \cdot (\frac{M50}{2} + \frac{M50}{2} \cdot sin(\omega \cdot t)) \qquad Eq.4.9$$

The gravitational force calculated over the total actuating mass as prescribed in Eq.4.10 where G is the gravitational constant.

$$F_{Gravity} = \; -m \cdot G \qquad Eq.4.10$$

Substituting Eq.4.7, Eq.4.9 and Eq.4.10 into Eq.4.1 the total force can be calculated using Eq.4.11

$$F_{total} = \; m \cdot \frac{x_{max}}{2} \cdot (2\pi \cdot f)^2 \cdot cos(2\pi \cdot f \cdot t) + 12 \cdot A_{CS} \cdot (\frac{M50}{2} - \frac{M50}{2} \cdot cos(2\pi \cdot f \cdot t)) - G \cdot m \qquad Eq.4.11$$

A potential voice coil was identified with a coil assembly mass of 0.71 kg. The prescribed user need of a maximum test frequency of 20 Hz for fatigue testing is replaced with a maximum of 30 Hz to once again accommodate for future custom tests that may require higher operating velocities. Figure 4.2 presents the total force and its separated constitutes at 30 Hz, note the mass acceleration and the stretch-induced force are π radians out of phase from one another. Due to destructive superposition, the two curves create an almost constant total force.

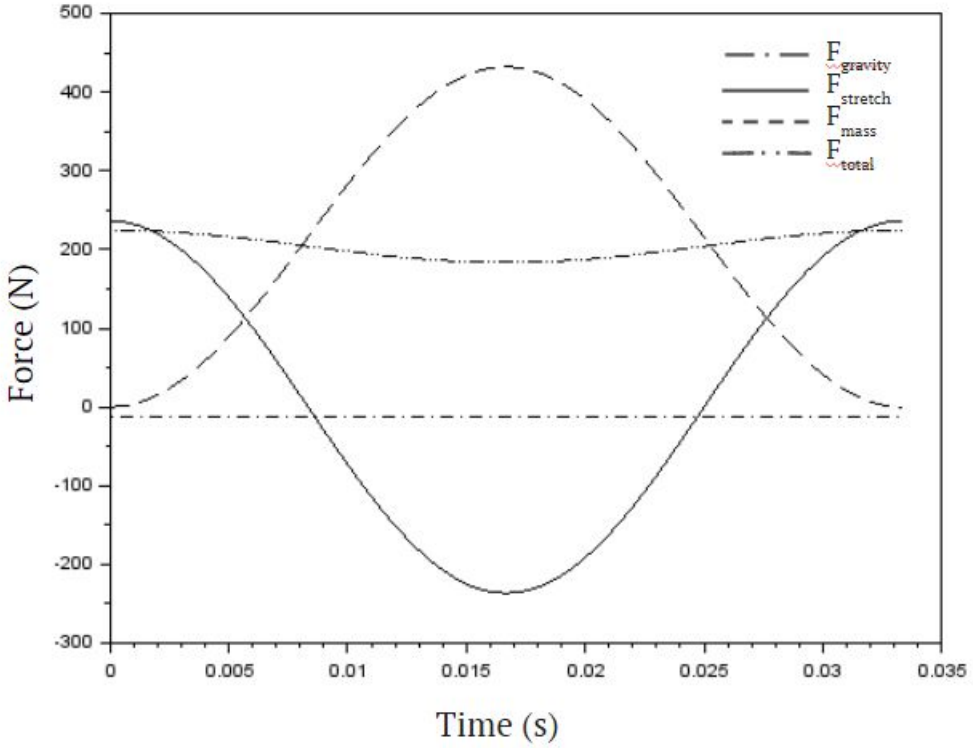

Figure 4.2: The total force and the three forces that make up the total force at 30 Hz.

In order to determine the required peak force, the entire range of testing frequencies is assessed under fully loaded conditions (12 test samples). Figure 4.3 shows the peak force across the full testing frequency range, note due to the phase cancellation the highest peak force is counterintuitively at the lowest testing frequency 1 Hz. This reveals that the peak required force is 420 N.

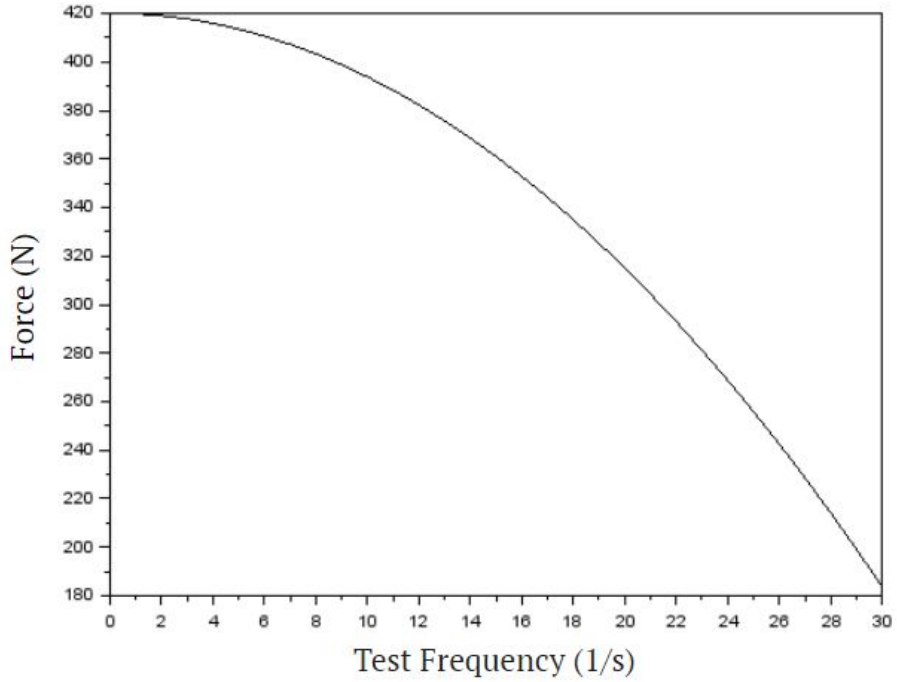

Figure 4.3: The peak force across all test frequencies.

Treating the sinusoidal and the independent constants as separate curves the combined RMS force can be calculated as described in Eq.4.12.

$$F_{rms} = \sqrt{F_{rms1}{}^2 + F_{rms2}{}^2} \qquad \textit{Eq.4.12}$$

Trigonometric expression's RMS value can be calculated using Eq.4.13 where A is the trigonometric scaling constant or amplitude.

$$F_{rmrTrig} = \frac{A}{\sqrt{2}} \qquad \textit{Eq.4.13}$$

Combining Eq.4.11, Eq.4.12 and Eq.4.13 the system required RMS force can be calculated as described in Eq.4.14.

$$F_{rms} = \sqrt{(m \cdot \frac{x_{max}}{2} \cdot (2\pi \cdot f)^2 - 12 \cdot A_{CS} \cdot \frac{M50}{2})^2 + (12 \cdot A_{CS} \cdot \frac{M50}{2} + F_{gravity})^2} \qquad \textit{Eq.4.14}$$

Once again the maximum RMS force, in the fully loaded condition, is determined across all test frequencies as presented in figure 4.4, again for the dynamic simulated load the maximum RMS force is experienced at the lowest testing frequency simply due to test sample load and mass acceleration being perfectly out of phase. The RMS force at the testing frequency of 1 Hz is 255 N.

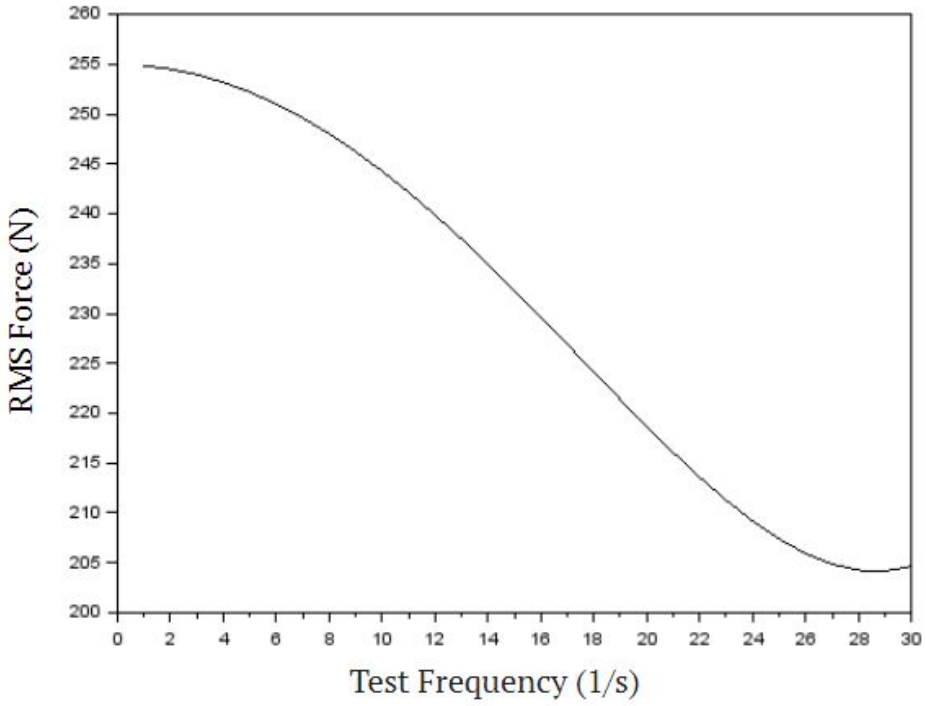

Figure 4.4: The RMS force across all test frequencies.

The continuous power limit is compared to the required root mean squared power, which is proportional to the square or F_{rms} and calculated using the Eq.4.15.

$$P = R \cdot (F_{rms}/K)^2 \qquad \textit{Eq.4.15}$$

Where K is the voice coil's specified force constant and R is the coil resistance, for the proposed voice coil K = 51.6 N/A and R = 3.0 Ohms, therefore using Eq.4.15 the required power is 73.2 Watts. Table 4.2 presents the required and rated selection values to assess the suitability of the proposed voice coil.

Table 4.2: The requirements to the selected voice coil's rated performance specifications comparison.

	Stroke (mm)	**Peak Force (N)**	**RMS Force (N)**	**RMS Power (W)**
Required	11	420	255	75
Rated	24.5	814.5	257.5	73.3

Table 4.2 indicates that the proposed voice coil is suitable for the specifications prescribed in the user needs, note the required RMS Force and Power power is very close to the maximum rating of the selected voice coil, however, the test specimen's modulus selected for this analysis has a 1.8 SF and therefore it is not of great concern. This being said higher test frequencies, as

described in the analytical model chapter, can present significantly higher stresses than that of slower strain rates, in these cases where the required Force and Power is presumed to exceed the rated specifications a reduced number of samples can be chosen for testing. In addition to this, the voice coil's protective covering has been designed to accommodate a cooling fan which can be implemented to increase the "rated" RMS Force and Power.

4.2.3 Force Sensor Selection

The Force sensors to capture the force involved in stretching the test specimens is chosen to be of an S type load cell. As discussed in the literature study S-type are specifically suited to tension applications and achieve high accuracy for a relatively affordable price. As determined in the actuator selection section the maximum specimen tension relates to a total force of 420 N, across 12 stations, the maximum expected force per load cell is 35 N. Selecting from standard options the 10 kg (98 N) load cell was preferred over the 5 kg (49 N) to account for test specimens with significant viscous responses that may experience significantly higher forces at higher testing frequencies. Utilising load cells rated in excess of 10 kg would begin to compromise the load cell accuracy at lower forces.

The load cells are arranged in a circular fashion suspended to the sensor platform in a height-adjustable manner, the bottom of the load cells is directly attached to the sensor clamp as shown in figure 4.5. The adjustability of the load cells/clamp height is useful to accommodate different test specimen sizes, fine-tuning the clamped specimen to start with zero tension or induce an initial pretension for specific test applications. Figure 4.5 describes how the load cell and clamp system's height is adjusted, the square bolts and hole constrains the system rotationally while the rotation of the nuts drives the system vertically.

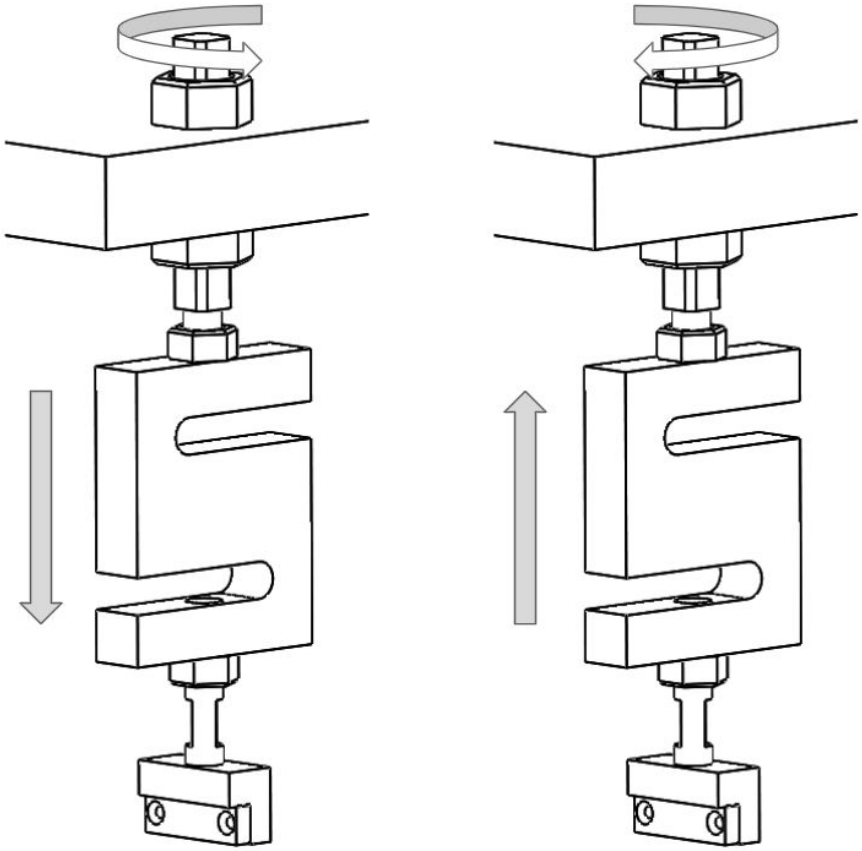

Figure 4.5:Tthe mechanism of height-adjustability for the force sensor system.

4.2.4 Displacement Sensor Selection

The actuator (voice coil) has no internal positioning feedback and therefore external displacement feedback is required, for both motor control and positioning data collection. A quadratic signal optical linear encoder with a linear marker strip is utilised. The linear coder and corresponding strip are selected because of the unit's diminutive size and negligible mass of the moving linear stip. Additionally, the selected encoder has a very high resolution of 25.4 µm/step, perfect for capturing small cyclic oscillations specific to this application. The selected encoder is capable of accurately capturing speeds of up to 9.144 m/s, almost 4 fold the theoretical maximum unloaded speed due to the limiting actuator peak force.

The mounting for the linear encoder strip as shown in figure 4.6 acts both as a shaft coupling (Motor shaft to actuator shaft) and a position zero reference. The moving coupling contains a slot to accommodate a stop pin, this stabilizes the system whilst the test specimens are loaded and provides the zero position for the control program to run off. This is particularly important because the selected linear encoder is simply incremental and contains no absolute positioning reference.

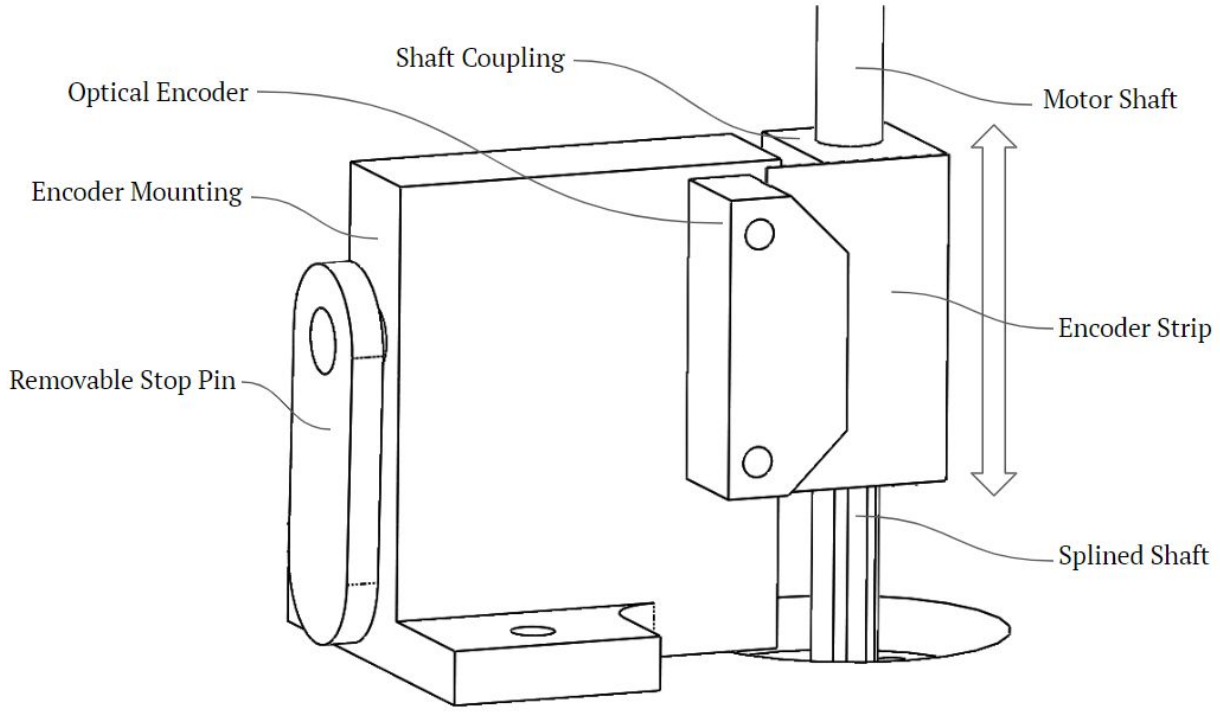

Figure 4.6: The linear encoder mounting and position zero locking system.

Figure 4.7 provides the manufacturer's rated specification for continuous force. Due to the reduction in force at the extremities the zero position reference is set up with the voice coil partially extended so to operate between 7 and 18 mm extension. Thus maximising actuation performance capability. The greyed out section in figure 4.7 represent the intentionally unutilised regions of stroke.

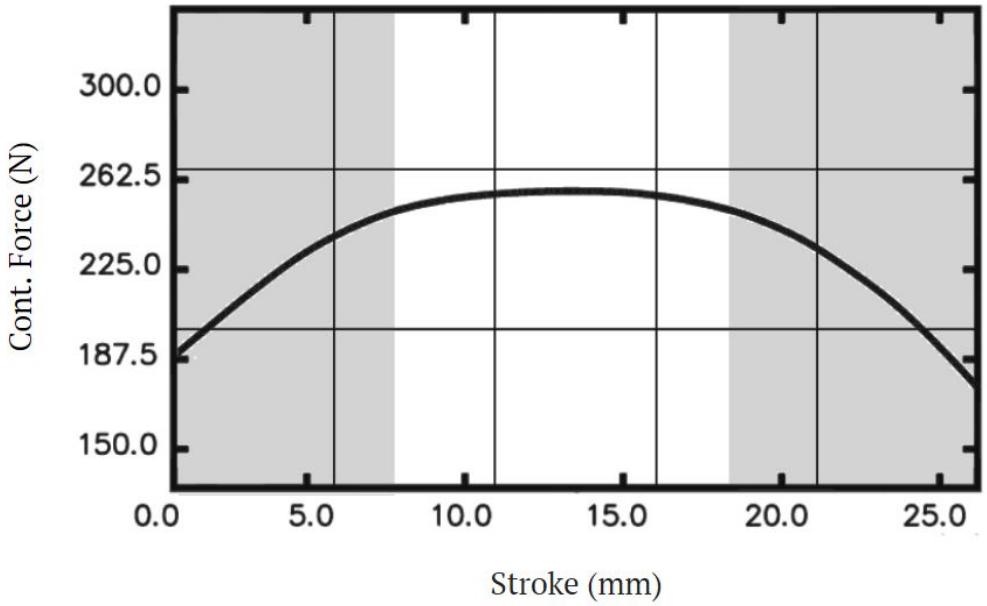

Figure 4.7: The region of maximised efficiency wherein the voice coil is positioned to operate.

4.2.5 Bearing Selection

The voice coil actuator selected is constrained using a plain bearing system and consequently not rotationally constrained, therefore a ball splined linear bearing is selected to prevent shaft rotation. No torque is explicitly induced on the system from the voice coil, therefore a linear bearing specified with relatively low torque resistance is selected, 0.98 N.m. To keep the moving parts as light as possible the thinnest possible splined shaft was selected with its corresponding bearing housing. This shaft is 6 mm in diameter which corresponds to the thickness of the selected voice coil's shaft. The maximum moment induced on the linear bearing is calculated according to the maximum asymmetric load, assuming all 6 specimens on one side of the actuated clamp break, leaving a worst case, asymmetrically loaded system as described in figure 4.8.

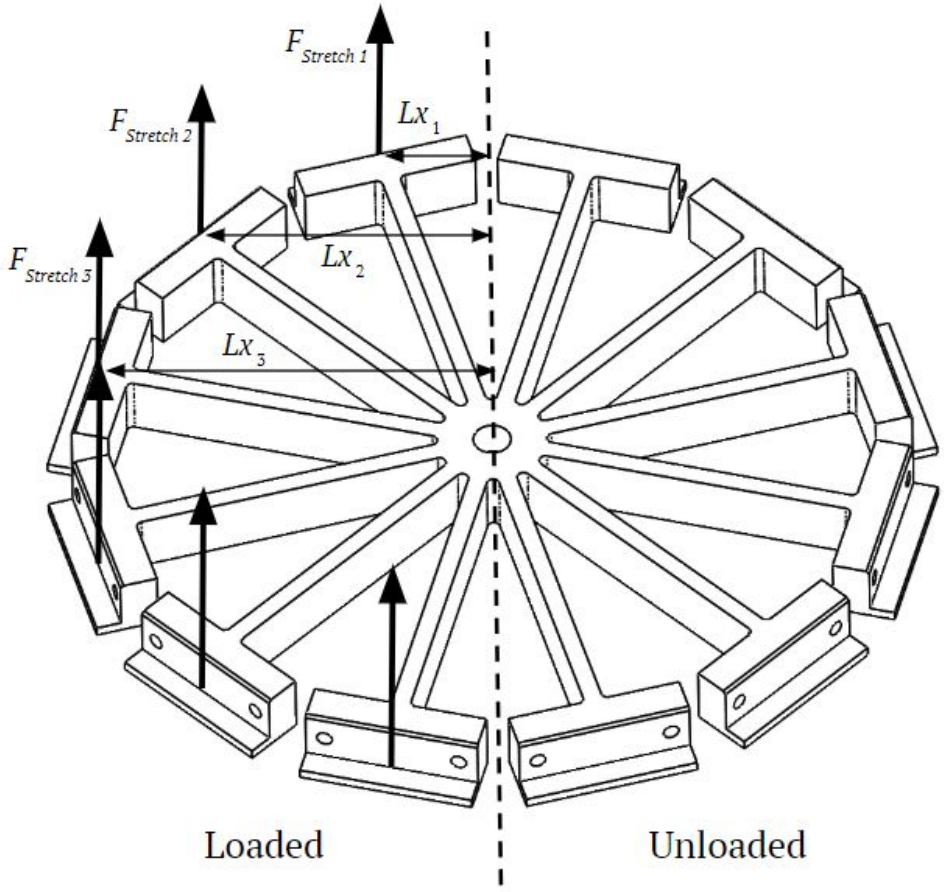

Figure 4.8: The conditions for worst-case loading on the bearing system with respect to moment.

The moment induced by this asymmetrically loaded system can be expressed by the sum of the moment induced by each stretched test specimen described by Eq.4.16.

$$Mo = F_{stretch1} \cdot Lx_1 + F_{stretch2} \cdot Lx_1 + F_{stretch3} \cdot Lx_3 \ldots \qquad Eq.4.16$$

Where Lx_x is the equivalent length in the x-direction of each specimen and $F_{stretchx}$ is the force induced by each stretched specimen. Assuming the maximum specimen induced force is equal across all 6 samples, Eq.4.16 can be expressed as presented in Eq.4.17

$$Mo = F_{stretch1} \cdot Lx \qquad Eq.4.17$$

Where Lx is the total equivalent length in the x-direction expressed as Eq.4.18

$$Lx = R \cdot 2 \cdot (sin(\tfrac{\pi}{12}) + sin(\tfrac{\pi}{4}) + sin(5 \cdot \tfrac{\pi}{12})) \qquad Eq.4.18$$

Where R is the actuated clamp radius which is 65 mm for this design. Substituting Eq.4.18 and an adjusted Eq.4.9 for 1 test specimens into Eq.4.17 the maximum possible moment on the bearing can be calculated using Eq.4.19

$$Mo = 1 \cdot A_{CS} \cdot M50 \cdot R \cdot 2 \cdot (sin(\tfrac{\pi}{12}) + sin(\tfrac{\pi}{4}) + sin(5 \cdot \tfrac{\pi}{12})) \qquad Eq.4.19$$

Assessed at a maximum strain of 50%, the maximum possible moment induced on the linear bearing is 9.03 N.m. A single bearing unit is rated at 4.9 N.m proving to be insufficient for the requirement, however, in accordance to the supplier data sheet, two bearing units in series on the same shaft results in a safe moment rating of 36.3 N.m. Therefore a bearing mounting as presented in figure 4.9 is incorporated to house two bearing units.

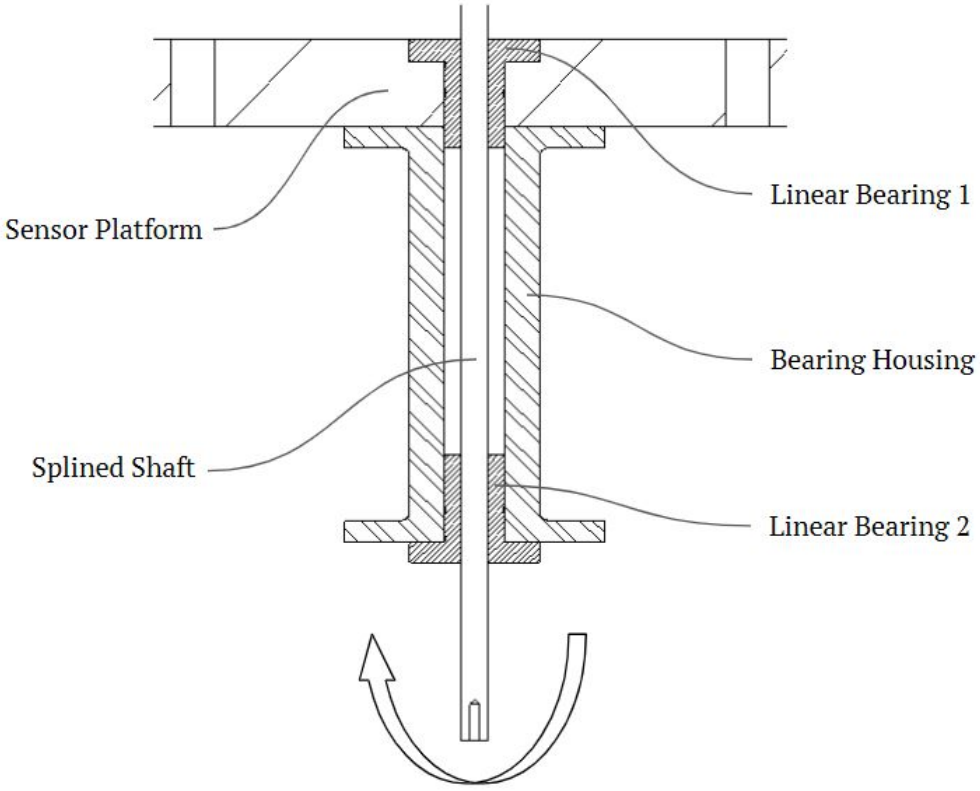

Figure 4.9: The bearing housing utilised to resist induced moments.

4.2.6 Environmental Control

As discussed in the literature study polymers present a chemical vulnerability in particular solutions. Therefore this fatigue tester is designed to simulate the corrosive conditions presented in blood. This dictates that all submerged mechanisms need to be machined from Stainless Steel 316 with a polished finish to reduce risk of corrosion. The submerged actuated specimen clamp displayed in figure 4.8 is designed to minimise fluid disturbance with thin ribs connecting the clamps to the central actuating shaft. The testing environment is contained in a glass bowl for chemical stability and visibility.

The human body temperature functions at an average of 37 ° C, this has a significant effect on polyurethane's stress-strain behaviour. The fatigue tester is designed to simulate this temperature and allow the operator to select from a range of environmental testing temperatures (23 -> 50 ° C) to further understand the mechanics of the test specimens.

The temperature control is achieved by using a standard panel mount temperature controller coupled with a submerged stainless steel Pt100 type temperature probe and a 500 W heater pad. The heating pad adheres to the outside of the base of the glass environmental chamber transmitting heat through the glass while avoiding chemical exposure.

The testing environment is completely removable allowing operators to load test specimens free form hazardous solutions and accommodate cleaning. To avoid thermal shock to the glass bowl the heating system should only be utilised when the test environment is filled with fluid.

4.2.7 Specimen clamping

The actuator and sensor clamp, utilises the same mechanism for specimen clamping, where the test specimen is sandwiched between the floating and the fixed surface of the clamp system as presented in figure 4.10.

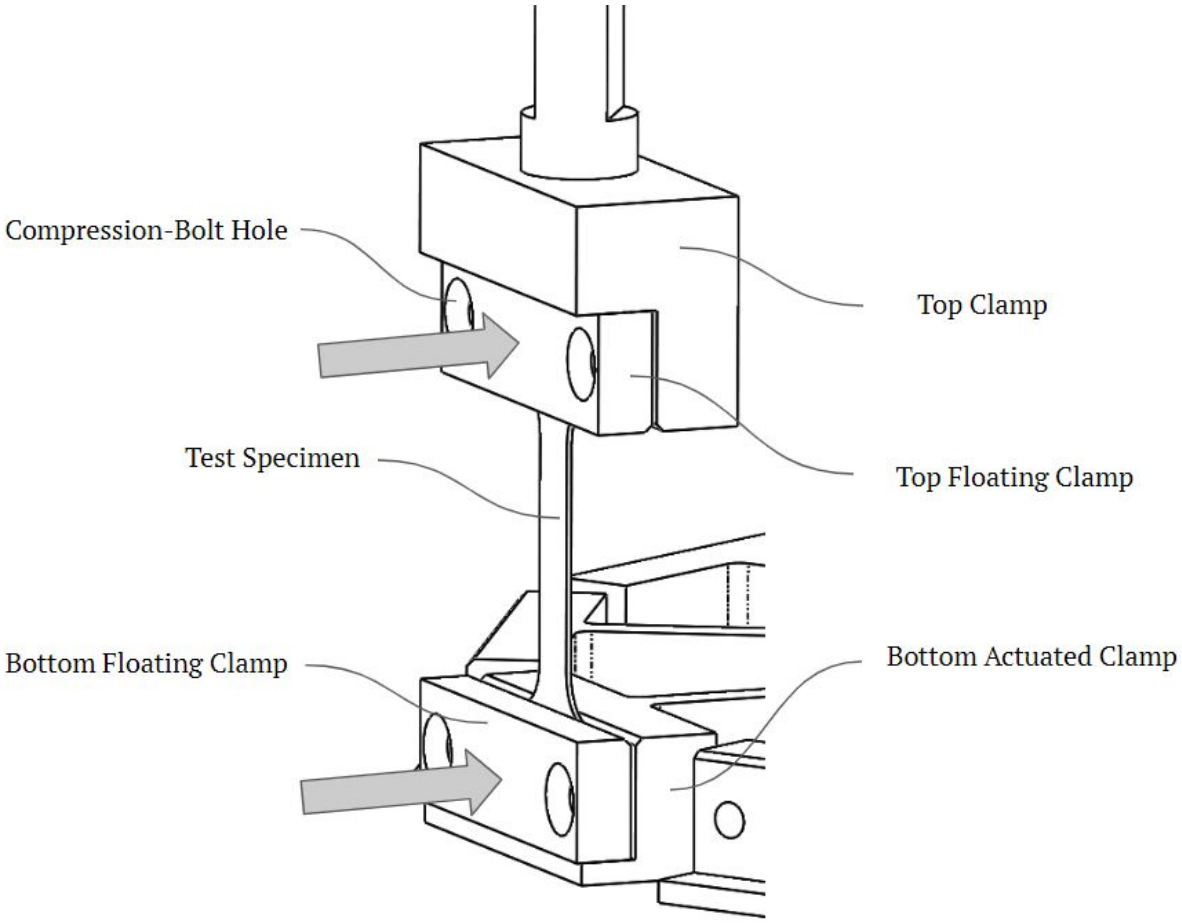

Figure 4.10: The test specimen clamping mechanism for both the sensor and actuated clamp.

The floating surface is tightened onto the specimen using the two allen cap M1.5 screws. A specified tightening torque is required to create sufficient friction to avoid specimen slippage without over tightening and causing stress concentrations at the clamping edge resulting in premature fatigue failure. To balance these extremes a torque settable allen key is utilised for tightening. The torque calculation is developed from the required clamping frictional force described in Eq.4.20.

$$F_F = SF \cdot F_{stretch\ Peak} \qquad Eq.4.20$$

Where SF is the safety factor preventing slippage, this is selected to be 2. The friction resulting from the normal force induced by the tightened floating surface is defined in Eq.4.21.

$$F_F = 2 \cdot F_N \cdot C_F \qquad Eq.4.21$$

Where F_N is the normal force on the test specimen, C_F is the lowest foreseeable coefficient of friction between polyurethane and stainless steel, in wet conditions and high durometer polyurethane a C_F=0.25 is applicable according to Gallagher Custom Polyurethane Molding (2019). As previously calculated the maximum force from a stretched specimen is determined to be 35 N, therefore with a SF = 2 the required friction is 70 N, resulting in a required normal force of 35 N. Therefore, assuming evenly distributed axial loads between the two tightening bolts, each bolt is required to exert 17.5 N of axial force. Using an axial force to torque conversation approximation tool, with an assumed tread coefficient of friction of 0.2, the required clamp bolt tightening torque is determined to be 5.25 N.m.

4.2.8 Mechanical Assembly

The designed micro-tensile specimen fatigue tester's custom part drawings can be seen in Appendix D. These parts are specifically designed to accommodate the selected aspects discussed throughout this section. The final mechanical assembly is presented in figure 4.11.

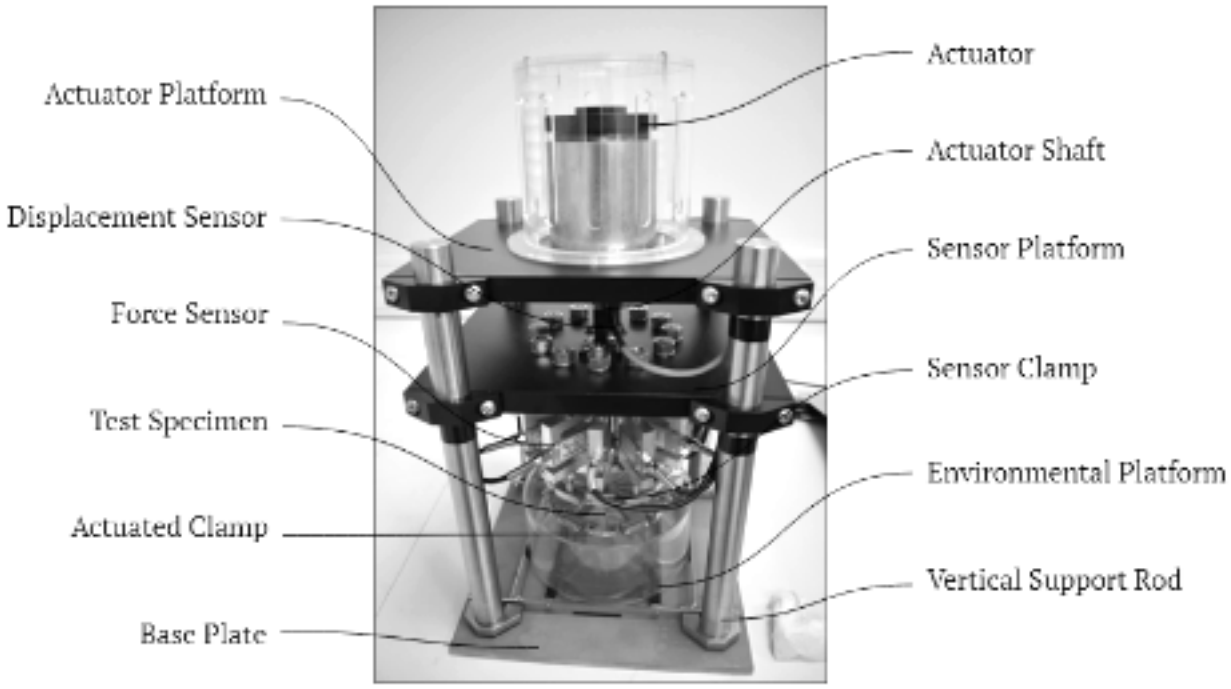

Figure 4.11: The complete fatigue tester mechanical assembly.

4.3 Electronics Hardware Design

This section describes the electronic hardware selection and design to control the systems functions, process and store data and provide a suitable computer free GUI for stand-alone operation.

4.3.1 Overview

The electronics are all contained in a laser cut control box, the box lid provides the platform for the operator GUI and is joined to the mechanical system through a series of data and power cables. The electronics design concept is summarised in figure 4.12. The electronic system consists of two controllers, one that controls the motor driver and the second is responsible for data acquisition and storage, both controllers have a dedicated GUI output in the form of LCD screens, and share GUI inputs. The temperature control is isolated from the two controllers and functions as a stand-alone feature. The entire system is powered through a panel mount emergency stop button to depower the entire system in the case of an emergency.

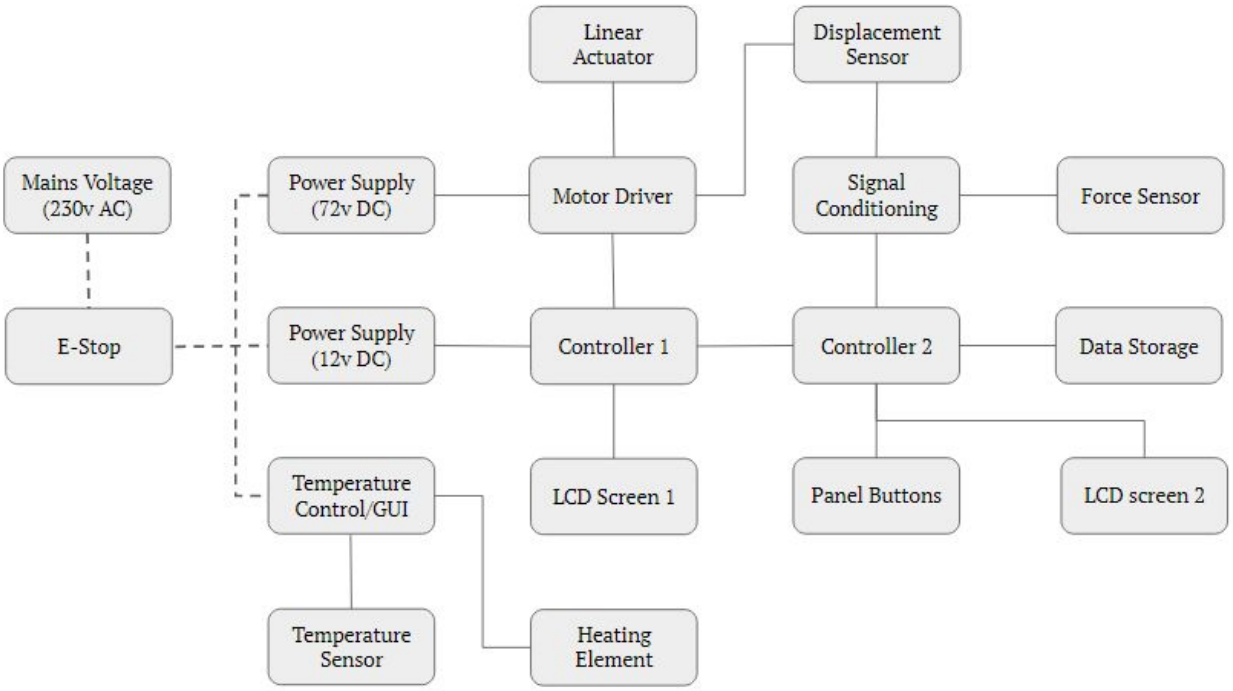

Figure 4.12: The electronic layout concept illustration for the fatigue testing machine.

4.3.2 Controller Selection

For multiple input/output pin communication, Arduino boards are ideal for system control. As presented in figure 4.12 the control unit is intentionally divided into two separate portions, enabling the motion controlling and data recording units to function independently. The data collection board (controller 2) in particular requires a relatively rapid clock speed to "simultaneously" capture all 12 analogue force signals in correspondence to a single displacement reference. The required sampling rate is set to be 40 samples per cycle providing enough overall information of the curve without creating unnecessarily large data files for lengthy fatigue tests. The controller's sample rate requirement for data collection at the maximum test frequency of 30 Hz is described in Eq.4.22.

$$SRate = n \cdot f_{Test} \cdot SD \qquad Eq.4.22$$

Where n is the number of test stations, f_{Test} is the testing frequency and SD is the cycle sample density which is set to 40. This dictates that the selected data collection controller's AnalogRead sampling rate needs to be well in excess of 14.4 kHz. The high-speed Arduino Due's (84 Mhz clock) standard AnalogRead functions at 25 kHz satisfying the high-speed sampling requirement. For ease of intercommunication compatibility, the motion control unit (controller 1) is also selected to be an Arduino Due.

Arduino Due boards operate at 3.3 V unlike that of the typical interfacing electronics which operate at 5 V. Op Amp level shifters and voltage dividers are incorporated where applicable to handle this voltage deficit. The two controllers can be accessed externally for custom tests and software upgrades via two USB ports as shown in figure 4.13.

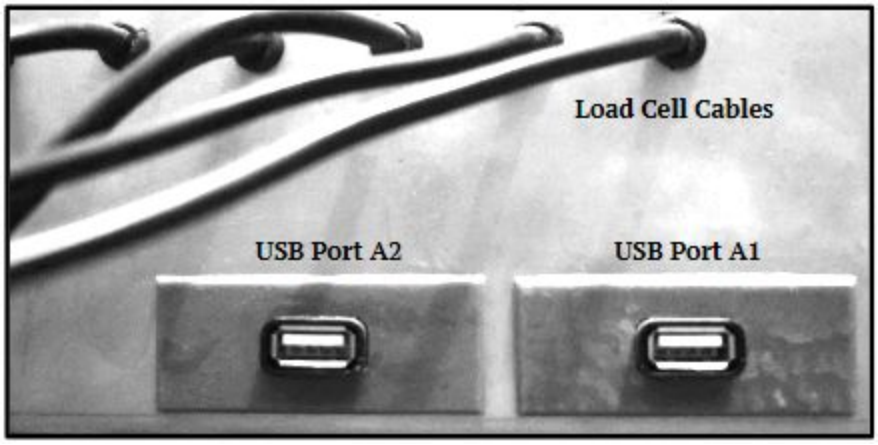

Figure 4.13: The USB connection ports to access both internal controllers 1 and 2.

4.3.3 Motor Driver Selection

Voice coil as selected for the system actuation can be controlled in the same fashion as a DC brush servo motor as described in the literature study, therefore a DC brush motor driver type is selected. The maximum current rating, voltage range and switching frequency are the major selection criteria in this case. For simplicity, it is preferable that the driver acquires its displacement feedback from the same quadrature TTL encoder signal used for the data acquisition. The maximum current required by the voice coil at maximum load (814.5 N) is calculated using Eq.4.23.

$$I_{peak} = \frac{F_{peak}}{K} \qquad \textit{Eq.4.23}$$

Where K is the force constant for the voice coil at 51.6 N/A. Eq.4.23 results in a peak current of 15.8 A. The driver voltage range needs to extend beyond the peak voltage to obtain the peak current as described in Eq.4.24.

$$V_{peak} = I_{peak} \cdot R \qquad \textit{Eq.4.24}$$

Where R is the coil resistance of 3 Ω, resulting in a peak voltage of 47.4 V. As per Eq.4.25, the step frequency requirement is calculated utilising the maximum speed obtained during the testing cycle as described in Eq.4.4 at a theoretical maximum of 57 Hz, which predicts a speed of ~ 2 m/s.

$$f_{step} = \frac{v_{peak}}{S_{Res}} \qquad \textit{Eq.4.25}$$

Where S_{Res} is the step resolution of the selected linear encoder 25.4 µm, resulting in a required step frequency of 80 kHz. By referring to table 4.3, it can be concluded that the proposed driver is suitable for the specified application.

Table 4.3: The required driver specifications to the proposed driver selection comparison.

	Peak Current (A)	Peak Voltage (V)	Step Frequency (kHz)	Quadrature TTL
Required	15.8	47.4	80	Compatible
Rated	15.7	18 - 48	300	Compatible

4.3.4 Signal Conditioning

The quadrature TTL encoder signal from the displacement sensor is decoded into a digital register containing the number of steps from the zero position reference. The HCTL-2022 (5 V) quadrature decoder circuit layout adopted for this application is presented in figure 4.14, note

both voltage dividers and op-amp voltage level shifter are utilised to communicate with controller 1 (3.3 V). The selected decoder is capable of counting 32-bit positions, the required total number of steps is calculated as described by Eq.4.26.

$$n_{bits} = ln(\frac{x_{max}}{S_{Res}})/ln(2) \qquad Eq.4.26$$

Where n_{bits} is the number of bits to count the maximum stroke x_{max} and S_{Res} is the encoder step resolution of 25.4 µm, this result is n_{bits} of 8.76, rounded up to 9 bits (> than 1 Byte). Therefore both the LSB and 3rd Byte as per the table in figure 4.14 is required to calculate the entire stroke range.

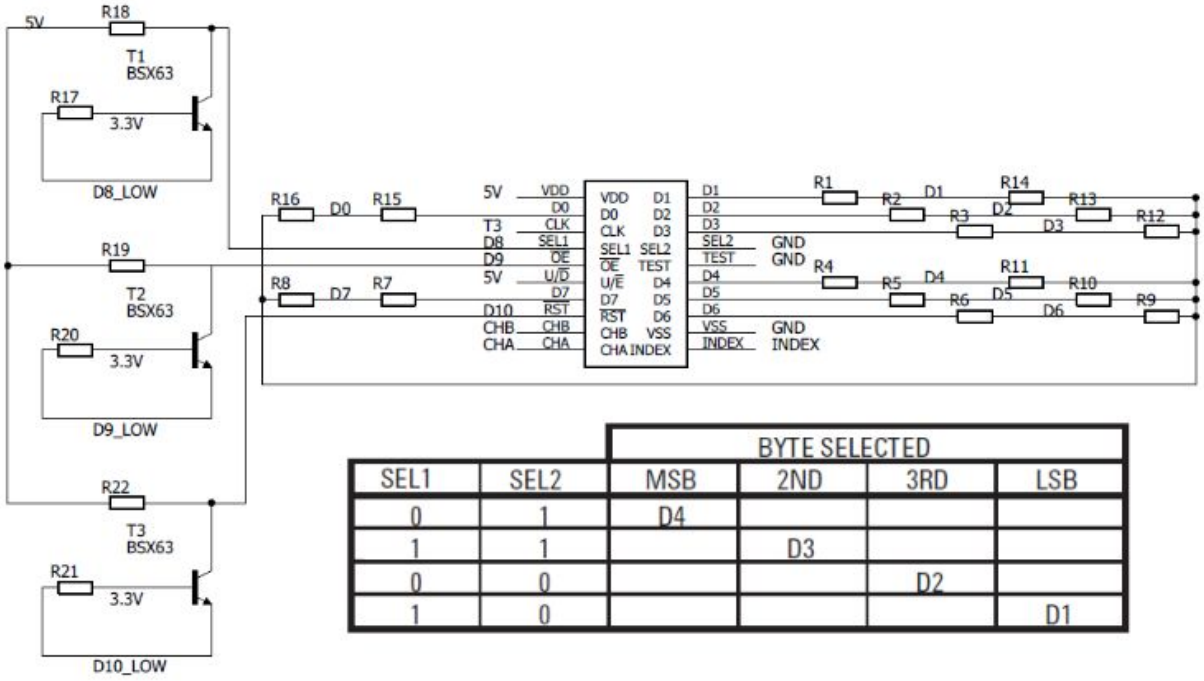

		BYTE SELECTED			
SEL1	SEL2	MSB	2ND	3RD	LSB
0	1	D4			
1	1		D3		
0	0			D2	
1	0				D1

Figure 4.14: The quadrature decoding circuit diagram and the byte selection table to read the appropriate section of the 32-bit position register.

The selected decoder functions from an external clock. To maximise the speed of the decoder a 555 timer integrated circuit configured in an astable condition is utilised to create the clock signal. Figure 4.15 provides the manufactures astable configuration layout with the measured voltage over CT where the selectable RA, RB and CT dictate the clock frequency. The output clock signal is High during the rising tc(H) period and Low during the tc(L) period.

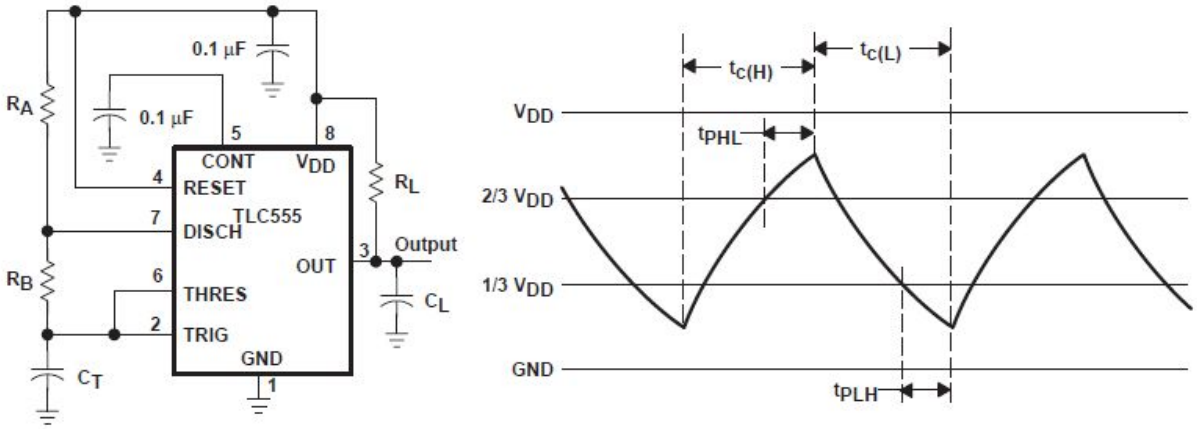

Figure 4.15: The astable configuration for the TLC555 timer and the corresponding CT voltage, reprinted from (Sophphx.caltech.edu, 2019).

The clock signal output frequency can be determined from the total cycle time as described in Eq.4.27.

$$f_{Clock} = \frac{1}{t_{c(H)}+t_{c(L)}} \qquad \textit{Eq.4.27}$$

In accordance with the manufacturer's datasheet, the raising CT voltage time tc(H) and tc(L) can be approximated using Eq.4.28 and Eq.4.29.

$$t_{c(H)} \approx C_T \cdot (R_A + R_B) \cdot ln(2) \qquad \textit{Eq.4.28}$$

$$t_{c(L)} \approx C_T \cdot R_B \cdot ln(2) \qquad \textit{Eq.4.29}$$

Selecting the following resistor and capacitor values, RA = 470 Ω , RB = 200 Ω and CT =200 pF, and substituting Eq.4.28 and Eq.4.29 into Eq.4.27, the generated clock signal frequency is estimated to be 8.3 MHz. In practice, it is shown that this approximation overestimates the actual output signal frequency, measured with an oscilloscope to be 2.1 MHz which is sufficient for the decoder IC's external clock.

To accurately capture the force signals from the load cells, both analogue amplification and filtering are required. The designed signal conditioning circuit is implemented for all 12 load cells and presented in figure 4.16.

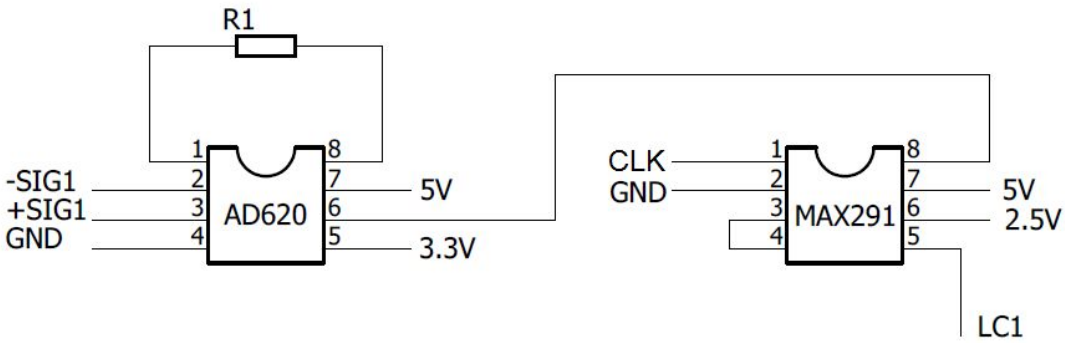

Figure 4.16: presents the signal conditioning circuit.

The load cell differential signal is initially amplified through the AD620, then filtered by the MAX291 IC. R1, as presented in figure 4.16, is selected to provide sufficient signal gain as presented in Eq.4.30.

$$R1 = \frac{R_{Internal}}{G-1} \qquad Eq.4.30$$

Where $R_{Internal}$ is the IC's internal resistance of 49.7 kΩ. The load cell differential output is calculated according to Eq.4.31.

$$dv_{LC} = v_{Excitation} \cdot O_{LC} \cdot \frac{F}{F_{Rated}} \qquad Eq.4.31$$

Where $v_{Excitation}$ is the excitation voltage which is set at 10 V, O_{LC} is the rated output ratio of 2m V/V and F denotes the load cell force experienced while F_{Rated} is the load cell's rated force of 100 N. This results in a differential voltage of 4 mV at the anticipated 20 N load. Therefore to maximise the resolution of this loading condition the required gain is obtained according to Eq.4.32.

$$G = v_{Range}/dv_{LC} \qquad Eq.4.32$$

Where v_{Range} is the maximum conditioned signal range, limited to 1.7 V due to the amplifiers maximum output swing and the controller ADC range. Which results in an optimised gain of 425. Substituting the required gain into Eq.4.30 results in an ideal resistance of 117 Ω for R1, therefore from the standard E12 range of resistors, a 120 Ω resistor is selected.

The selected lowpass filter possesses an adjustable pass-bandwidth feature. The corner frequency is adjusted according to the input clock frequency as described in Eq.4.33.

$$f_{Corner} = f_{Clk} \cdot CR \qquad Eq.4.33$$

Where CR is the conversion ratio of 1:100. The desired pass bandwidth is 0 to 45 Hz to capture the full range of testing and to minimise the typical 50Hz interference from mains power. Therefore the clock frequency is set to 4.5 kHz, this is driven by controller 1.

4.3.5 User interface

In accordance with the user needs the fatigue tester is to function independently from a PC. The operator selects test parameters and initiates/terminates testing programmes from the control machine panel itself. Two LCD screens provide feedback and prompt selection instructions while push buttons and toggle switches provide inputs to the control system as seen in figure 4.17.

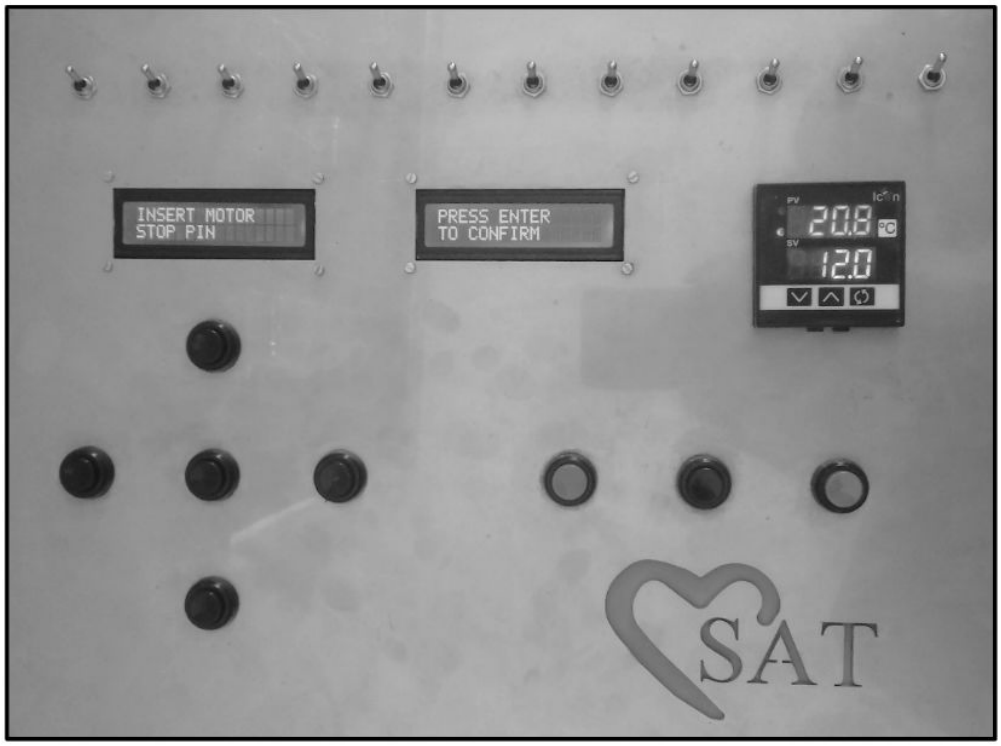

Figure 4.17: The operator-machine interface.

The test data is stored on an SD card which is accessed by the operator via an SD slot on the side of the control box as presented in figure 4.18. The test data stored on the SD card is, however, post-processing on a PC hosted open source software called Scilab.

Figure 4.18: The control box side panel with a removable SD card slot for test data storage.

4.3.6 Power Distribution

The fatigue tester operates off a single mains plug, which is isolated through a panel mount emergency stop. The electronics cooling fans, heating pad and temperature control function directly of the 230 AC mains. Two internal power supplies, power the motor driver and the control and data acquisition system. The motor driver is powered by a 48 V DC 750 W power supply, while the low power electronics are powered by a 12 V DC 24 W power supply. A 10 V regulator is incorporated to maintain the load cell excitation voltage. The IC's are powered through the Arduino's built-in 5 V regulator.

4.3.7 Electronics Assembly

The electronics are hole mounted onto four custom-designed PCBs as presented in Appendix C. In the laser cut control box provisions are made for two cooling fans to regulate the internal temperature of the control box. Figure 4.19 presents the control box in operation mode and opened to display the internal electronic layout and wiring.

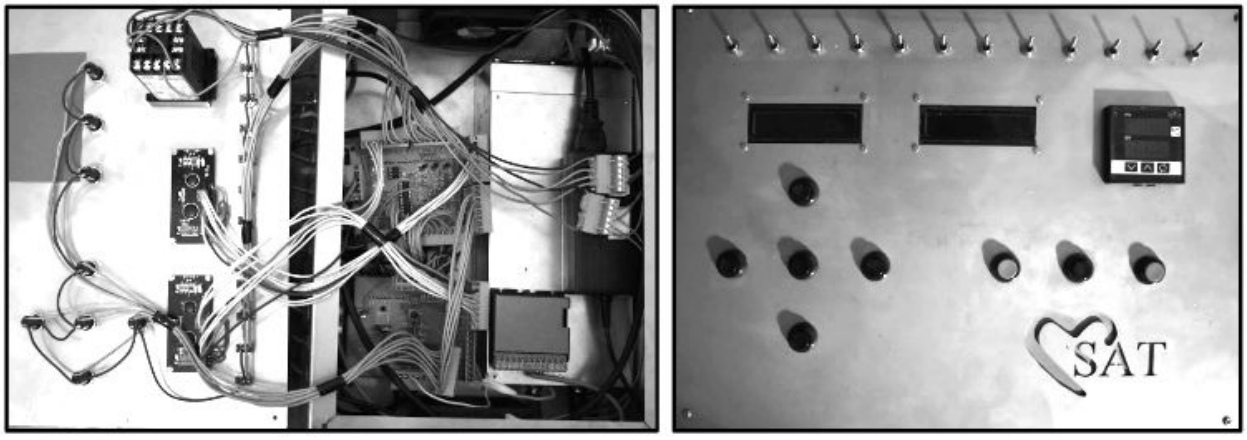

Figure 4.19: The control box in the open and closed state.

4.4 Software Design

This section describes the overall software control logic, highlighting the unique coding methods specifically utilised for the control and data capture of the fatigue and tensile testing machine.

4.4.1 Overview

The fatigue and tensile testing machine is controlled by two central processing units (Atmel SAM3X8E ARM Cortex-M3 CPU - Arduino Due). CPU 1 is employed to control the actuator function whilst CPU 2 simultaneously controls the recording and saving of the acquired data. As depicted in figure 4.20 both Arduinos share the parameter selections input functions and digital input panel buttons, the common information allows the data recording to be specifically tailored to the selected loading program, otherwise, the two CPU's essentially operate independently from one. The control code is scripted in an Arduino's C++ IDE software. The complete script for both CPU's is presented in Appendix A, including comments providing further detail.

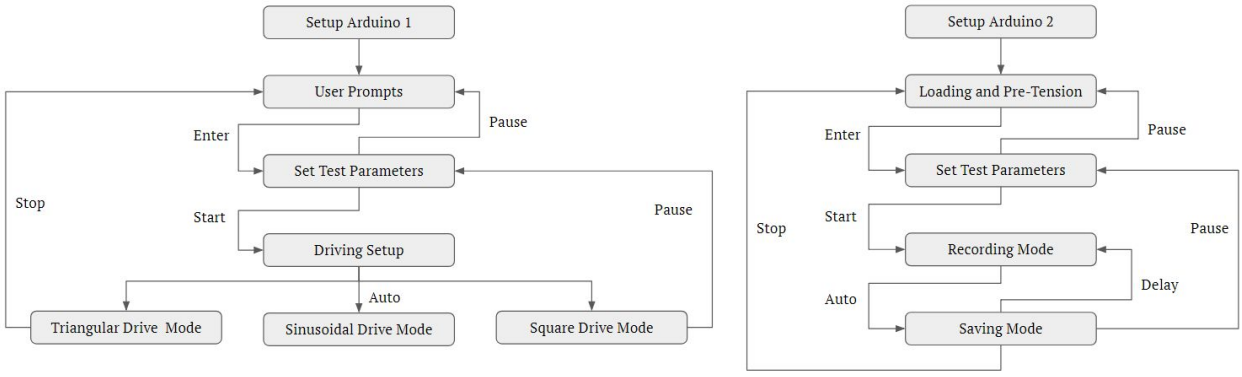

Figure 4.20: The summarised code layout running on Arduino 1 and 2 respectively.

4.4.2 Test Parameter Selection

This shared function enables the operator to select a fatigue test program through the machine's GUI. Figure 4.21 details the parameter select function describing the navigation through subprograms and test parameter value adjustment. The Amplitude and Frequency selection contains upper and lower limits. The program provides a warning when the operator attempts to exceed this set range.

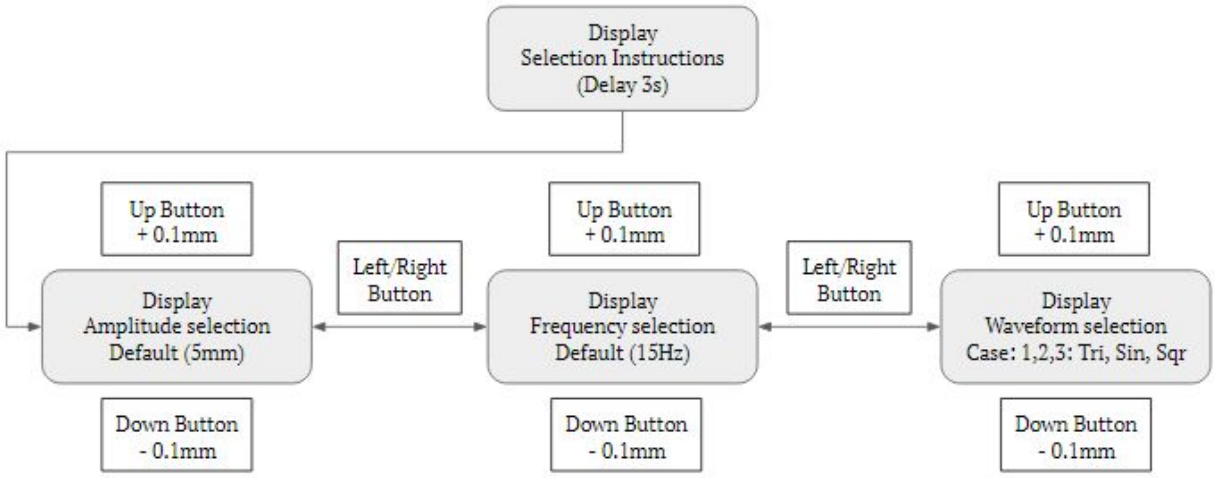

Figure 4.21: The parameter selection function navigation.

4.4.3 Driving function

From the waveform sub-function within the parameter selection function, one of three driving modes can be selected. These include the Triangular, Sinusoidal or Square waveform. There is a dedicated driving function for each of these cases. The motor driver is controlled through the manipulation of the motor driver's step and direction pins. The step pin signal dictates when the driver moves from one encoder increment to the next, while the digital high or low signal on the direction pin dictates the step direction, in this application resulting in either up or down motion. The loading waveform is produced by defining the delay time between step signals.

Triangular waveform mode is the simplest control function due to the constant time delay between incremental steps. The time delay between steps is calculated using the Eq.4.34.

$$td_{Tri} = \frac{S_{res}}{2f \cdot X} \qquad Eq.4.34$$

Where S_{res} is the step resolution, f and X are the selected test frequency and amplitude, respectively. The direction pin toggles at the end of each stroke.

The sinusoidal loading waveform is produced by manipulating the time/displacement function derived in Eq.4.2 to represent time as the subject of the function. The time at each encoder step increment is determined according to Eq.4.35.

$$t[n] = \frac{1}{2 \cdot \pi \cdot f} \cdot cos^{-1}((\frac{X}{2} - n \cdot S_{res})/\frac{X}{2}) \qquad Eq.4.35$$

Where the variable time delay between each encoder step increment can be calculated as described in Eq.4.36.

$$td_{Sin}[n] = t[n] - t[n-1] \qquad Eq.4.36$$

The direction pin is again toggled at the apex of the loading stroke.

A true square waveform requires infinite acceleration which requires infinite power, therefore, this mode only approximates a true square waveform. To best approximate a square waveform the controller's step signal is set to exceed the theoretical maximum acceleration of the voice coils in an unloaded condition, therefore ensuring the lagging output always operates at maximum speed limited only by the motors power output. For the active period, the time delay between step signals is calculated as described by Eq.4.37.

$$td_{Squ} = \frac{S_{res}}{2 \cdot f_{Excess} \cdot X} \qquad Eq.4.37$$

Where f_{Excess} is a frequency set in excess to the theoretical maximum test frequency of 57 Hz, and chosen to be 60 Hz. If the system experience too much overshoot on the rising and falling edge of the square wave the td_{Squ} period may need to be iteratively extended. The rest period delay is calculated by subtracting the active period from the prescribed test frequency's corresponding period as described by Eq.4.38.

$$td_{rest} = \frac{1}{2 \cdot f} - \frac{1}{2 \cdot f_{Excess}} \qquad Eq.4.38$$

4.4.4 Force Sensor Accuracy

The load cells selected have a full-scale non-linearity rating of 0.03%, the anticipated loads are 20% of the full-scale rating and therefore the error due to non-linearity is assumed to be insignificant. The load cell differential voltage is proportional to the force subjected to the load cell, assuming linearity the force is calculated using Eq.4.39.

$$F = M \cdot (LC_{read}) + C \qquad Eq.4.39$$

Where M is the load cell calibration gradient, LC_{read} is the measured load cell voltage signal and C is the load cell zero point error. Load cell force measurement is susceptible to temperature drift, zero point error and signal noise, which all reduce data accuracy. The recording and setup function is designed to digitally minimise the effects of these issues. These digital solutions assume the load cell calibration gradient M to be both constant throughout testing and equal across all the load cells. Upon startup, the data acquisition CPU's setup function runs a comparative sampling test for all unloaded test stations against the unloaded reference load cell. This results in an initial load cell offset as described in Eq.4.40. This comparison compensates for the zero point error and is independent of environmental temperature, basically recalibrating the load cells upon system startup.

$$LC_{Offset\,0} = LC_{Read\,0} - LC_{Ref\,0} \qquad Eq.4.40$$

Where $LC_{Read\ 0}$ is the initial unloaded reading on the sampling load cell while $LC_{Ref\ 0}$ is the initial reading on the reference load cell. For reduced noise and thus improved accuracy these readings are averaged over 100 samples at startup conditions. The reference load cell and the measuring load cells share the same environmental conditions and experience the same temperature fluctuation. This simultaneous load cell drift from one temperature condition to the next is presented in figure 4.22 where the curved lines represent the equal drift between the measuring and the reference load cells.

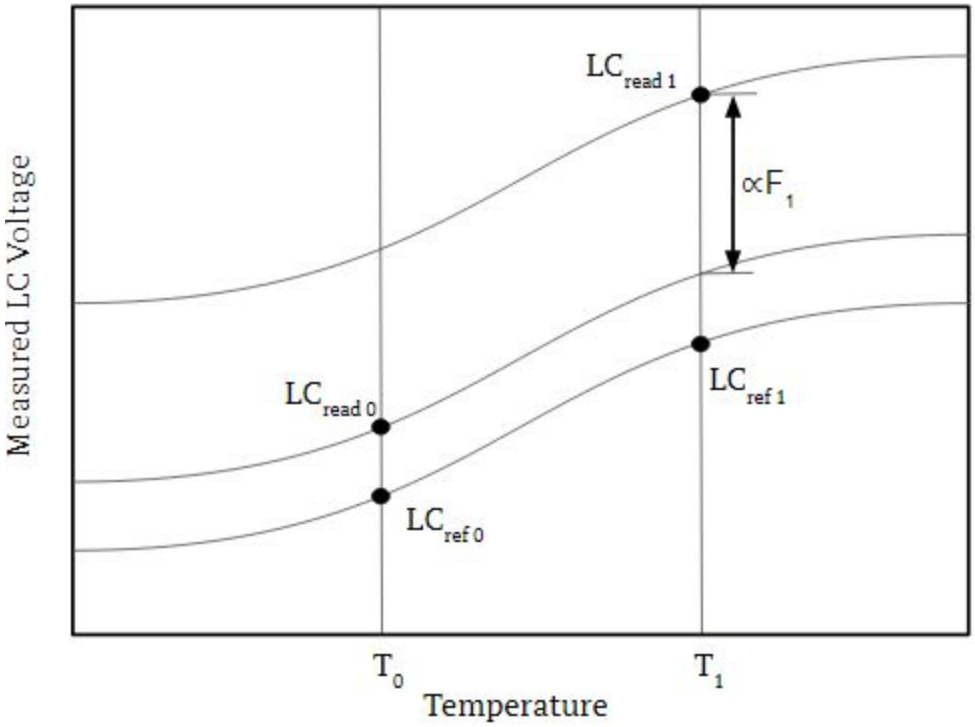

Figure 4.22: The adopted logic for temperature drift and initial offset compensation.

Following the logic presented in figure 4.22 the force can be calculated from the difference between the loaded testing load cells measurement and the unloaded reference load cell measurement at the current temperature condition while subtracting the initial offset constant as described in Eq.4.41.

$$F = M \cdot (LC_{Read} - LC_{Ref} - LC_{Offset\,0}) \qquad Eq.4.41$$

Upon specimen loading the control program enables the operator to view the instantaneous tension, providing an opportunity to precisely zero or pretension the specimens if desired.

4.4.5 Data Acquisition

With regard to fatigue tests, which may last up to a year, the data storage needs to take capacity into account. To conserve space the fatigue recording is programmed to record for 5 second

every 10 min. After every 5 seconds of recording the data is transferred to the SD card via an SPI connection. 5 seconds every 10 min is considered sufficient to capture the degradation of the test specimens over time. The sampling frequency is set at 1200 Hz which corresponds to 60 samples per cycle at the maximum test frequency of 20 Hz. Custom tensile tests are continuously recorded as they are typically relatively short tests. The machine custom test period with constant recording is limited by the CPU's internal memory, the maximum custom test period is calculated according to Eq.4.42.

$$t_{custom} = Mem/(S \cdot sf) \qquad Eq.4.42$$

Where Mem is Arduino Due's internal memory of 2 GB, S is the space utilised per timestamp and sf is the sampling frequency set at 1200 Hz. Every time stamp, recorded as a double (8 Bytes), is saved with all 12 recorded load cells reading as an Int (4 Bytes) and 1 position Int, therefore the total space utilised per timestamp is calculated to be 60 Bytes. Therefore the *custom* tests are limited to roughly a 7.5 hour period.

4.5 Combined Assemblies

The designed and selected mechanical and electronic components are controlled by the developed software to create a standalone multi-stationed microtensile specimen fatigue tester with test environmental control. The completed design and build is presented in figure 4.23.

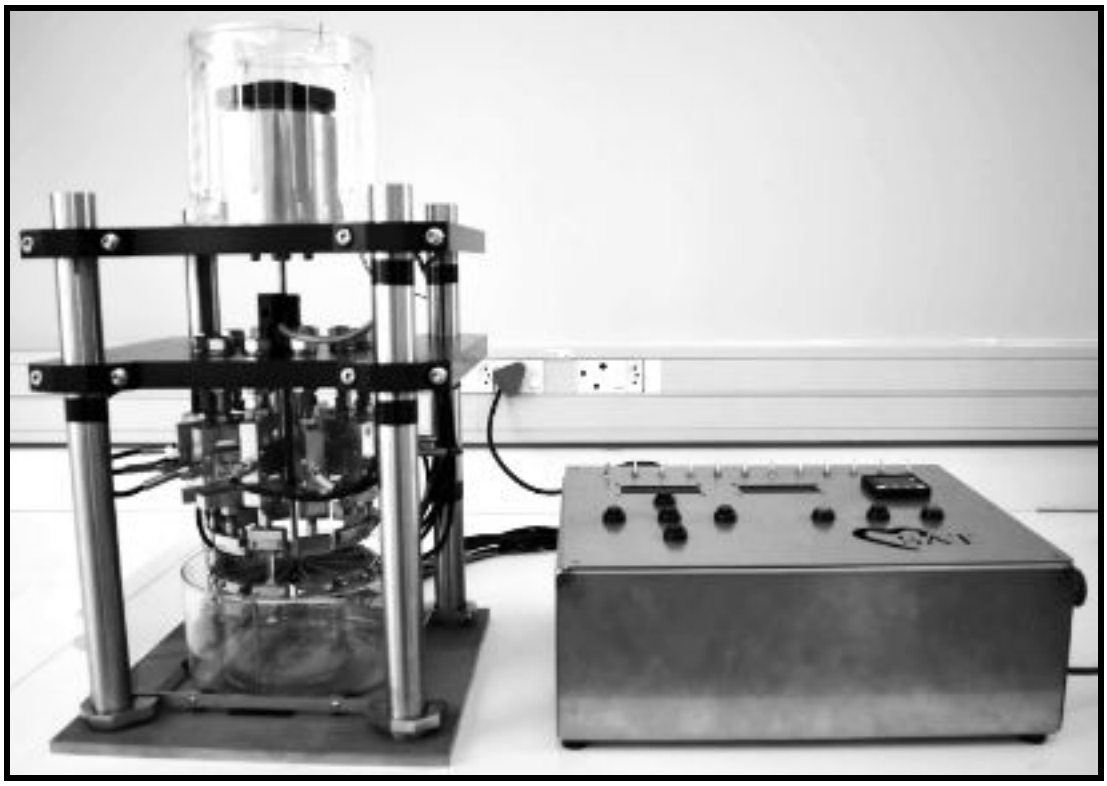

Figure 4.23: The complete fatigue tester assembly.

5 Experimental Design

This chapter's main objective is to describe the methods utilised to assess the proposed analytical model for the stress-strain behaviour of thermoplastic polyurethanes. In addition, describe the methods employed to verify the designed and assembled microtensile specimen fatigue tester. The material and equipment used to conduct this verification and the software to analyse the data is also described within this experimental design chapter.

5.1 Microtensile Specimen Material

Pellethane® 2363-80AE is the selected TPU utilised for the microtensile specimen production to verify both the machine and model. The microtensile test specimen preparation follows the sequence prescribed below:

1. Raw Pellets Drying - 24 hours @ 30 °C in a vacuum oven
2. Film Heat Pressing - Heat press at 200 °C with a 0.8 mm shimming stencil
3. Die Punching - Using a die and press, as prescribed by the ASTM D1708 in figure 5.1
4. Storage - Lain flat in a sealed specimen container @21 °C

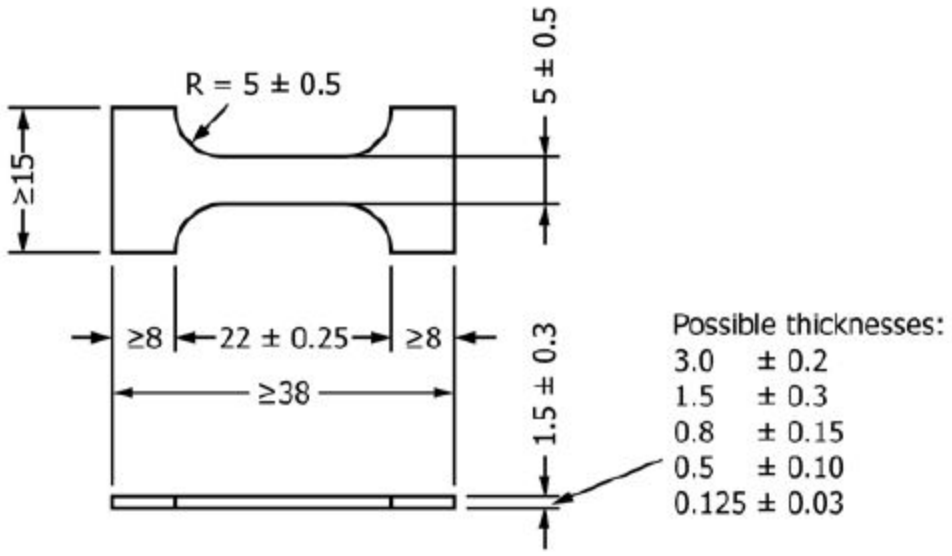

Figure 5.1: The ASTM D1708-13 prescribed microtensile test specimen dimensions.

5.2 Model Verification Methods

This section describes the methods to create the appropriate test data and assess the conjectures made in the proposed model. A validated commercial Instron 5544 tensile tester is predominantly utilised throughout the model testing to ensure accuracy. The proposed model simulation functions are coded in Scilab, for script details view Appendix B.

5.2.1 Softening Evaluation Test Method

This tests objective is to assess the validity of the proposed model where the evolution of the number of monomers between crosslinks in included. This will be assessed by comparing the proposed model's simulation to the experimental data as well as to the model developed from Arruda and Boyce (1993) and Qi and Boyce (2004).

The simulation variables are summarized in the list below:

1. V_{S0} - Effective soft segment fraction.
2. V_{SS} - Saturation Soft segment fraction.
3. μ - Soft segment modulus.
4. N_0 - Initial number of monomers between crosslinks (relative free chain length).
5. N_S - Saturation number of monomers between crosslinks.
6. A - Effective soft segment fraction evolution factor.

The material variables for the simulation comparison are identified by assessing the experimental break pull to break data. The equilibrium response is best approximated by conducting a pull to break test at the slowest test speed of $\dot{\varepsilon}$/s = 0.001 on the Instron 5544, note this method may slightly overestimate the equilibrium however due to the significantly slow strain rate it is assumed that the viscous response is insignificant.

The hard and soft segment composition ratios provide a good estimation of the effective hard and soft segment fraction, V_H and V_S respectively. It is important to note that the effective soft segment fraction can slightly exceed the composition ratio due to the non-contributing soft segment which is fixed by encircled hard segment.

The saturation soft segment fraction V_{SS} is set to 1, assuming that the hard segment binding hydrogen bonds will disassociate before the covalently bonded molecular chains break. Once again it is important to note that specimens may fracture before complete evolution of hard to soft segment in isolated areas and therefore a slightly lowered saturation soft segment fraction may in some cases be more appropriate.

The chain density μ is selected by assessing the experimental data at low strain (0.5) where the hard segment break up is assumed to be insignificant.

The initial number of monomers between crosslinks N_0 is identified by best fitting the curve at lower strains while the saturation number of monomers between crosslinks N_S is determined by assessing the experimental data at higher strains.

The soft segment fraction evolution factor A is determined by best fitting the curve shape. Note, a higher simulated value of A causes more rapid dissociation of hard segment and therefore an increase in the soft segment fraction.

Finally, two graphs are to be created, firstly, where the current model from literature is compared to the experimental data, secondly, where the proposed model is compared to the experimental data. These plots will provide a visual representation of the model feasibility.

5.2.2 Loading History Evaluation Test Method

The proposed model of loading history assumes zero hard segment recovery, and therefore the subsequent loading cycles resume using a V_s associated with the maximum strain of the specimen's loading history. The table 5.1 specifies the maximum strain of each cycle used to illustrate the loading history phenomenon. All cycles are loaded at a strain rate of ε /s = 0.01.

Table 5.1: The maximum strain of each loading cycle.

Cycle 1	Cycle 2	Cycle 3	Cycle 4
100%	200%	300%	400%

5.2.3 The same material variables as determined in the softening feasibility test methods are used for the simulation comparison. The experimental data and simulated model are plotted separately, providing a visual comparison to assess the models capability to capture the stress strain behaviour's dependence on loading history.

5.2.4 Viscous Effect Evaluation Test Method

The proposed conjecture suggests that the effective number of monomers between crosslinks N_0 is affected by the rate of strain, accounting for the viscous response. This is assessed by plotting and comparing the simulated proposed model to that of the experimental data obtained using the Instron 5544 at various strain rates. This model incorporates an addition viscous factor B which dictates the sensitivity to strain rate ultimately representing the degree of viscous effect.

Table 5.2 summarizes the Instron test parameters selected to assess the viscous effect model, each sample is extended to break. The Inston 5544's maximum speed is set at 1020 mm/min.

Table 5.2: The Instron test parameters to assess the proposed rate dependant model.

	Test 1	Test 2	Test 3	Test 4
Extension rate (mm/min)	1.32	13.2	132	990
Equivalent strain rate (ε /s)	0.001	0.01	0.1	0.75

The material variables remain as determined for the softening model evaluation. The additional viscous factor is determined by best fitting the curve over the extension rate 0.001 and 0.01 s^{-1}.

5.3 Machine Verification and Validation Methods

This section describes how the fatigue tester is verified against the prescribed machine requirements. The methods to create custom test programs is also described within this section.

5.3.1 Motion Control Verification Method

First, the PID system is tuned and tested to provide optimum control. In this application, it is imperative that overshoot is minimised to avoid overstraining the test specimens. The PID multipliers are verified by inputting a ramp function to the motor driver and assessing the recorded displacement, figure 5.2 provides an example of a system in either an over, critically or underdamped condition for comparison. The step function used to assess the PID control is set to the maximum controller step input capability, this is the equivalent speed to produce a triangular waveform at 140 Hz over an amplitude of 6 mm.

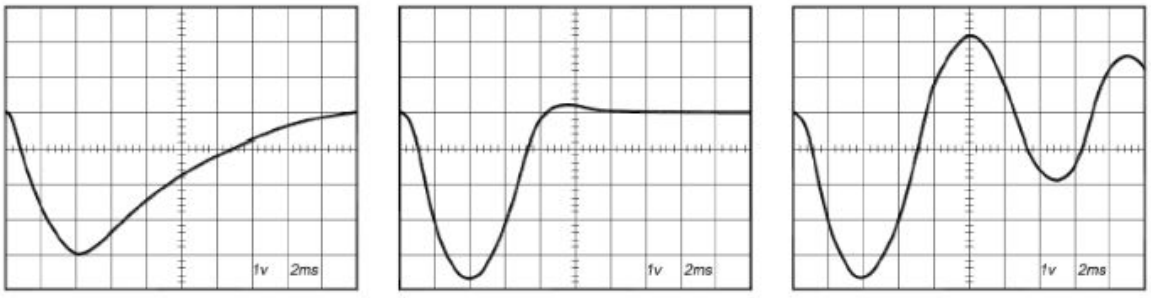

Figure 5.2: A system reaction to a disturbance presenting different levels of damping.

5.3.2 Motion Capability Verification Method

Each waveform function is assessed at a constant frequency and amplitude as presented in table 5.3 for comparison. The recorded motion is saved to the SD card for analysis.

Table 5.3: The test parameters used to verify the unloaded system motion control.

Test #	Waveform Mode	Frequency (Hz)	Amplitude (mm)
1	Triangular	5	3
2	Square	5	3
3	Sinusoidal	5	3

The maximum achievable test frequency across the full 6mm amplitude range is to be tested according to the criteria mentioned below.

- Position overshoot less than 10% for all waveforms
- Square waveform's rest period must exceed 50% of the wave cycle

5.3.3 Customizing Test Methods

The fatigue tester is designed with an additional feature to accommodate custom-designed fatigue tests. This function is demonstrated by creating a custom test waveform. The waveform selected to simulate is that of the strains experienced within a flexible heart valve concept design. This is achieved by conducting Finite Element Modeling (FEM) on a proposed leaflet design, the meshed element that experiences the highest strain is then assessed throughout the modelled diastolic and systolic cycle. Figure 5.3 presentes the two problematic node locations that are to be assessed to create the custom waveform.

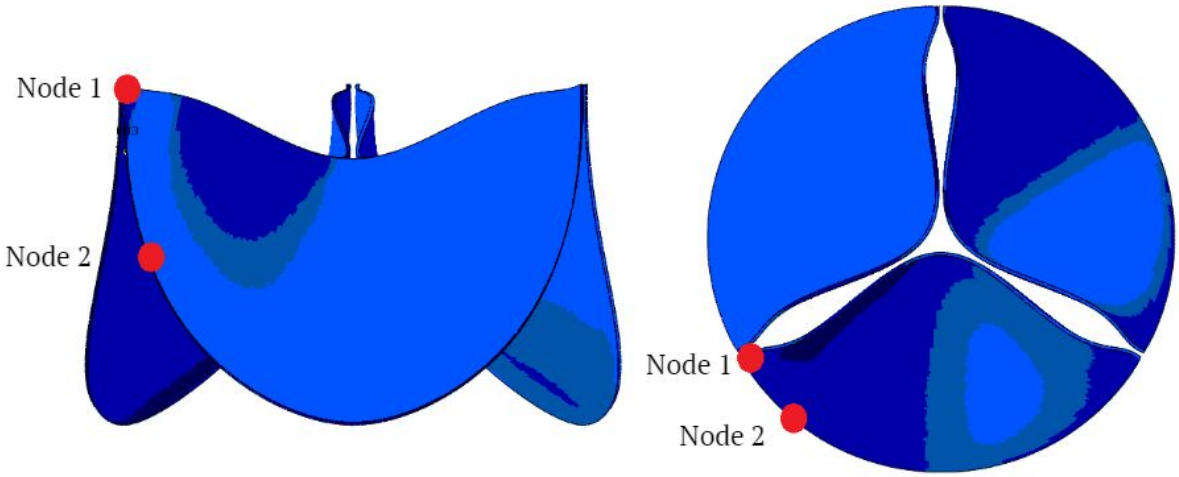

Figure 5.3: The problematic nodes locations under analysis.

By changing pressure as the control variable in the FEM analysis, the principle strain at the prescribed nodes is recorded throughout the cardiac cycle as presented in table 5.4 and table 5.5.

Table 5.4: The leaflet strains observed during systole.

Side View	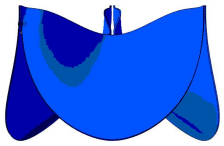	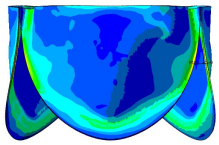	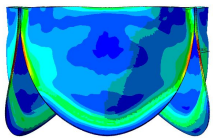	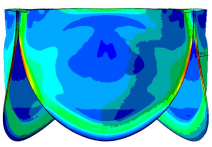
Top View	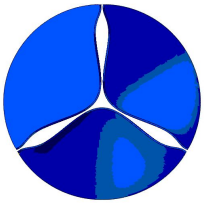		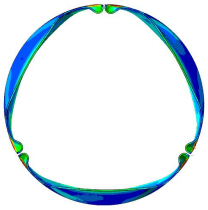	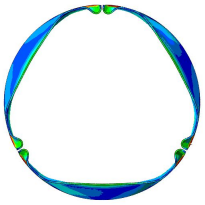
Strain Node 1	0	0.01	0.015	0.015
Strain Node 2	0	0.18	0.22	0.25

Table 5.5: The leaflet strains observed during diastole.

Side View	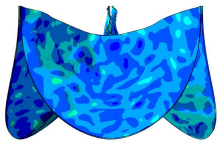	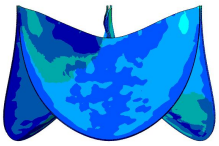	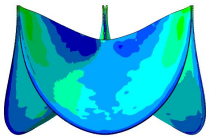	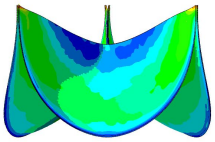
Top View	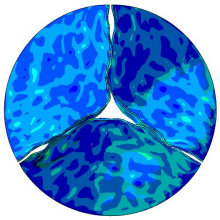	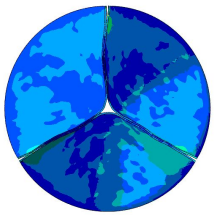	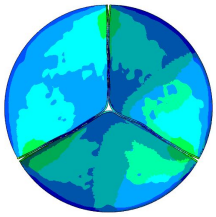	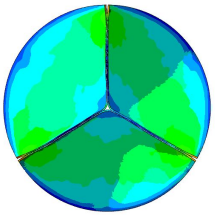
Strain Node 1	0.09	0.16	0.21	0.27
Strain Node 2	0.09	0.01	0.05	0.08

The waveform developed to simulate these strains is simply modelled as straight lines between the simulated data points. Note that this technique of waveform matching increase with accuracy as the simulation sampling resolution increases. To demonstrate this machine function the strain in Node 2 is simulated and tested on the fatigue tester. For this simplified example, the strain at each time interval on a 1 Hz cycle is summarized in table 5.6.

Table 5.6: The custom strain waveform inputs for Node 2.

	5.3.5 Diastolic				5.3.9 Systolic			
5.3.13 Time (s)	5.3.140	5.3.15 0.125	5.3.16 0.25	5.3.17 0.375	5.3.18 0.5	5.3.19 0.625	5.3.20 0.75	5.3.21 0.875
5.3.22 Strain %	5.3.230	5.3.24 18	5.3.25 22	5.3.26 25	5.3.27 9	5.3.28 1	5.3.29 5	5.3.30 8
5.3.31 Disp mm	5.3.320	5.3.33 3.96	5.3.34 4.84	5.3.35 5.5	5.3.36 1.98	5.3.37 0.22	5.3.38 1.1	5.3.39 1.76

5.3.40 Data Acquisition Verification Methods

The data acquisition system's accuracy is compared to that of a verified commercial tensile tester, Instron 5544. The test conditions are set up as presented in table 5.7, note although the two machines have different inputs types the effective motion is matched for direct comparison. This test is set up using the maximum test speed of the Instron 5544, and a custom test program for the fatigue tester.

Table 5.7: The test parameters to effectively compare force accuracy between the designed fatigue and tensile testing machine and the commercial Instron 5544.

	Designed Fatigue and Tensile Tester			**Instron 5544 Tensile Tester**	
Test #	Waveform	Amplitude (mm)	Frequency (Hz)	Amplitude (mm)	Speed (mm/min)
1	Triangular	11	0.75	11	990

The force measured in the first loading cycle on both testing machines is compared at strains of 10, 20, 30, 40 and 50% as presented in figure 5.4.

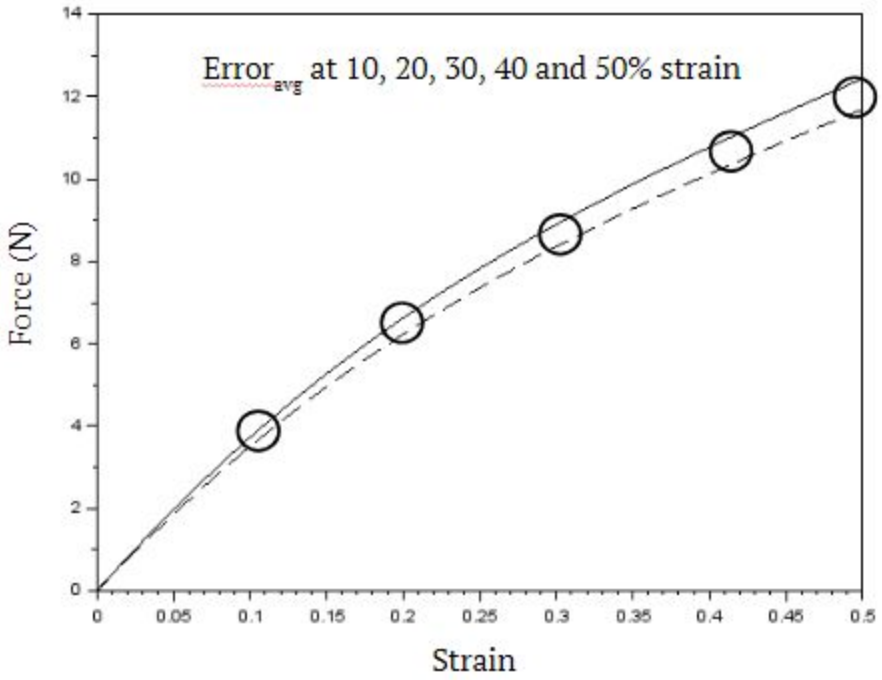

Figure 5.4: The force response curve comparison method between the two machines.

The average error is calculated according to Eq.5.1 at each strain interval.

$$Error_{avg} = \left| \left(F_{avg}^{Instron} - F_{avg}^{Fatigue} \right) \right| / F_{avg}^{Instron} \qquad Eq.5.1$$

The average force measured from the designed fatigue tester ($F^{Fatigue}$) is calculated from three simultaneously tested samples.

The steady-state noise of the designed fatigue tester is once again compared to that of the commercial tensile tester, Instron 5544. To assess the effectiveness of the signal conditioning circuit the force is sampled for 1 second in both the machines. All 12 load cells are assessed against the Instron's single sensor. The force data is compared with respect to maximum range and standard deviation thus representing the degree of steady-state noise.

5.3.41 Environmental Control Verification Methods

The fluid-filled testing environment is tested for splashing across a range of frequencies. The unloaded machine’s environmental control bowl is ¾ filled with water and a series of tests are performed at an amplitude of 6mm for 1 min at a range of frequencies, f = 1, 5, 10, 15 and 20 Hz. During this test the degree of fluid disturbances is observed and graded as negligible, mild, moderate and severe, the grading definitions are summarised in table 5.8.

Table 5.8: The grading conditions associated with the degree of fluid disturbance in the environmental control bowl.

Grade	**Conditions for grading**
Negligible	Virtually no visible fluid disturbances
Mild	Visible fluid disturbances, but no external splashing
Moderate	Visible fluid disturbances, with minimal external splashing
Severe	Significant external splashing

With relatively inert fluids like water, moderate disturbances are tolerable for short test periods, however, for long term fatigue tests or tests containing highly oxidative solutions a zero or mild grade of fluid disturbance is prescribed.

The ¾ water filled fluid bath's heating capabilities is tested at the maximum prescribed setting of 50 °C, the bath temperature is logged every 5 minutes using a calibrated 100 °C lab thermometer, only once the temperature has settled at the setpoint for more than 10 minutes is the test complete. The temperature controller's sensor value is simultaneously logged and compared to that of the thermometer. The temperature logging thermometer is utilised in the following manner:

1. The thermometer is placed in the centre of the fluid bowl, both radially and with respect to height.
2. The thermometer is kept in the heated fluid and only momentarily removed for temperature readings.
3. Readings are taken immediately after removal from the fluid.
4. Reading are taken holding the thermometer perpendicular to the tester's line of sight.

5.3.42 Final validation Method

The fatigue tester is finally validated in its standard fatigue testing capacity through a simulated use test. Here the full set of user needs is tested, from test selection through the user interface, to specimen loading, specimen clamp slippage, to long term stand-alone testing and data storage all under controlled environmental conditions. This designed fatigue tester verification test is set up for 6 test specimens with the test parameters presented in table 5.9. Note this test is prescribed for one hours worth of testing however full-scale fatigue tests may continue for a number of days.

Table 5.9: The fatigue tester validation test parameters.

Amplitude (um)	Frequency (Hz)	Waveform type	Temperature (°C)	Environment Solution	Duration (min)
6000	5	Sinusoidal	37	H_2O	60

The data is assessed by measuring the decay of peak force over time as well as the Peak stress versus number of cycles.

5.4 Data Analysis Methods

Custom data analysis code is developed to assess large data sets for long fatigue tests. These methods work by sampling the data set at defined time intervals then interpreting the data surrounding the selected point.

5.4.1 Peak Force Analysis Method

Typically the peak force over time is of interest in fatigue tests. It takes very long to find and plot every recorded peak force for large data sets often associated with fatigue tests. Therefore a sample interval is defined where the nearest peak-force to the sample point is recorded. This is repeated for the entire data set, summarising the data into a decaying peak force trend throughout the fatigue test duration. The peak force is determined as presented in figure 5.5, each data point within half a cycle of the sample interval point is compared, identifying the peak force within the single cycle sample range. This peak force is then recorded and plotted for the corresponding time interval.

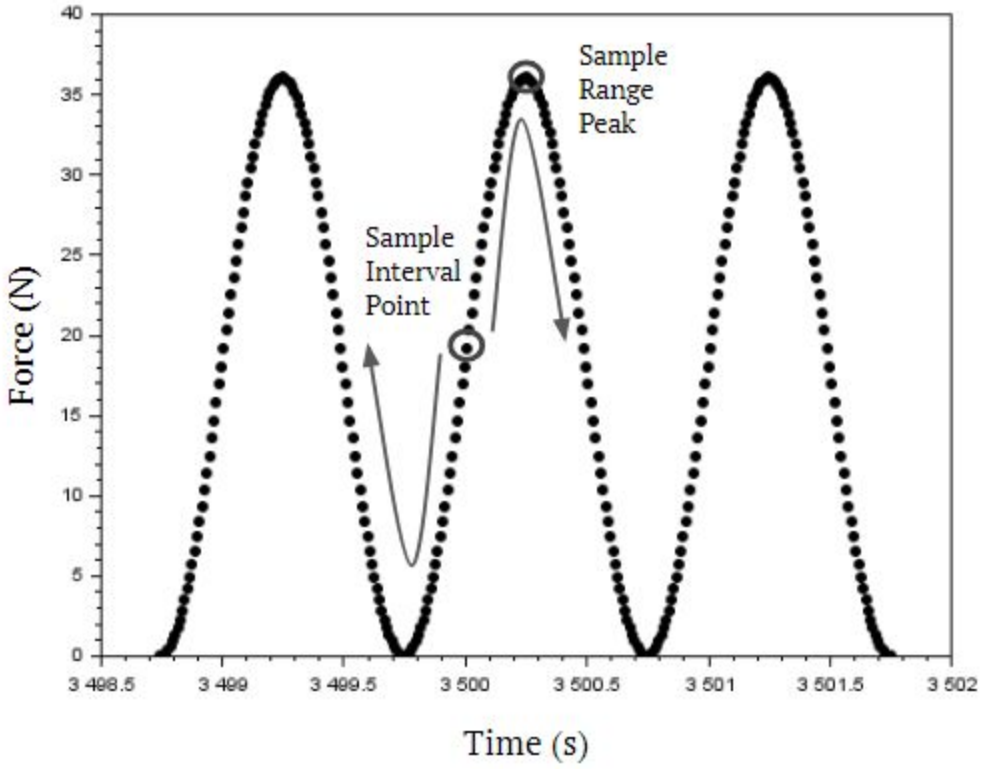

Figure 5.5: The method employed to identify the peak force from the fatigue tester generated data set.

5.4.2 Hysteresis Analysis method

The first step to determine the hysteresis within a loading cycle is to determine the start, middle and end of the loading cycle, the data points with the maximum and minimum displacements are determined using the same logic described in figure 5.5. Hysteresis is defined as the energy dissipated during a loading cycle which is equivalent to the area under the stress-strain curve. This area can be calculated using the area under the force-displacement curve, divided by the square of the test specimens cross-sectional area. The area under the curve is determined as described in figure 5.6, the accumulative unloading area is then subtracted from the loading area.

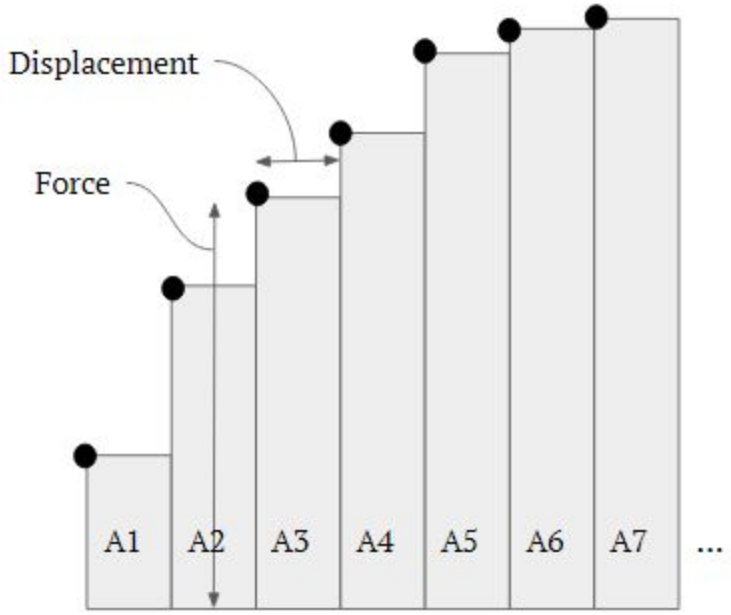

Figure 5.6: *The method of calculating hysteresis from the fatigue tester generated data set.*

From the data acquired during the fatigue test the hysteresis is calculated using the logic presented in figure 5.6, this can be formulated as described in Eq.5.2, Eq.5.3 and Eq.5.4.

$$Hys = A_{loading} - A_{unloading} \qquad Eq.5.2$$

$$A_{loading/unloading} = A1 + A2 + A3 + \ldots \qquad Eq.5.3$$

$$Ax = Fx \cdot Dx \qquad Eq.5.4$$

Where A is the subdivided area, F is force data point and D represents the displacement difference between data points.

6 Results and Discussion

This chapter presents the assessment of the two material selection tools described throughout this report. The simulated material model is compared to the test data and critiqued. The microtensile specimen fatigue tester functionality and accuracy assessments are presented and discussed in this chapter.

6.1 Model Results and Discussion

This section presents how the polyurethane material model captures the material softening, loading history dependence and the viscous behaviour of polyurethanes. The results are followed by commentary highlighting the model's limitations and successes.

6.1.1 Softening

As discussed in the previous chapters the current strain energy models for thermoplastic polyurethane utilises a fixed number of monomers between crosslinks throughout the strain range, as per the proposed model, this number of monomers is adapted to evolve with the evolving soft segment fraction. Figure 6.2 and figure 6.1 present the stress-strain behaviour prediction with and without the evolution of the number of monomers between crosslinks. Both simulations are perfectly fitted to the experimental data for the strain range of 0 to 100% and then left to run to a strain of 600%.

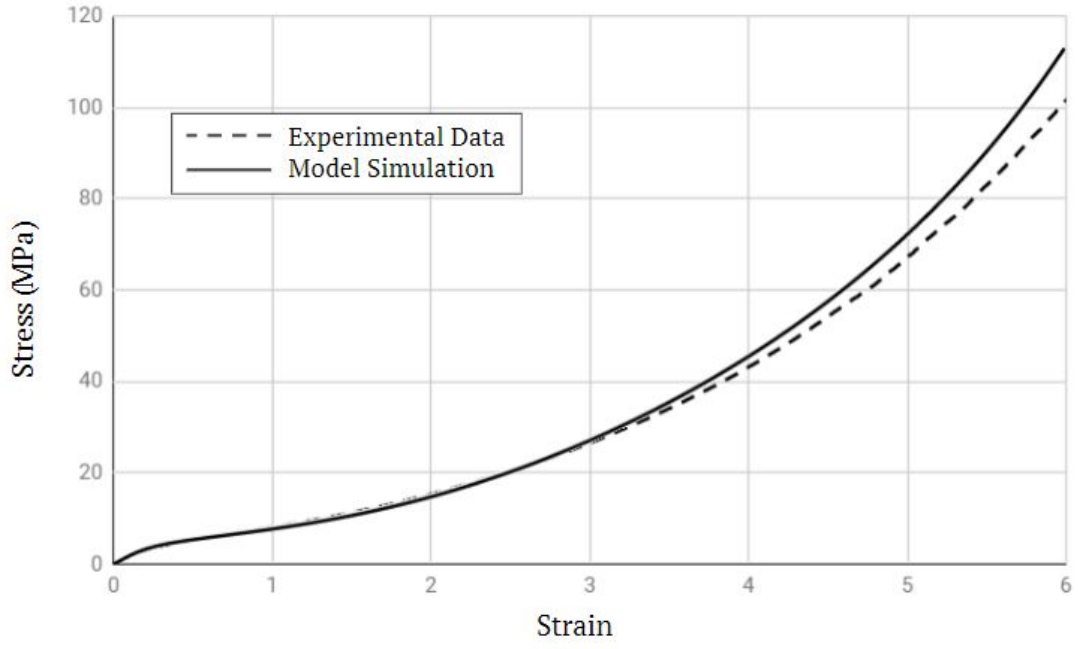

Figure 6.1: *The comparison between the stress-strain behavioural model (with a **static** number of crosslinks between monomers) to the acquired experimental stress-strain data.*

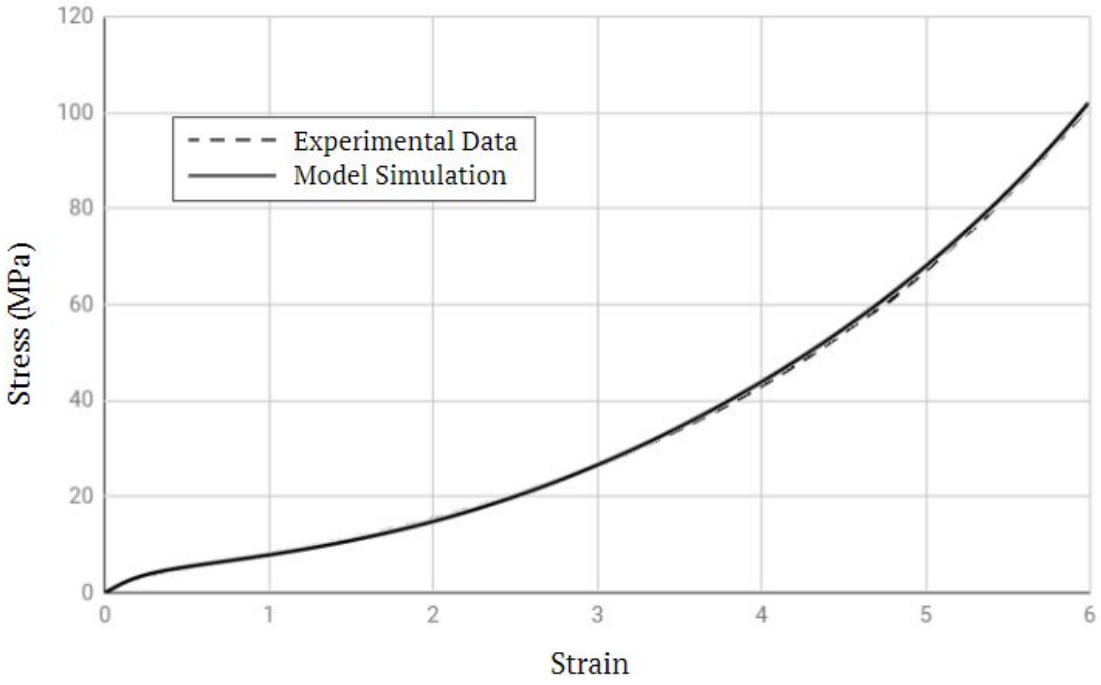

Figure 6.2: *The comparison between the stress-strain behavioural model (with an **evolving** number of crosslinks between monomers) to the acquired experimental stress-strain data.*

The inclusion of the evolving number of monomers between crosslinks results in different chain lockout lengths during the macroscopic straining of these polymer networks, ultimately creating a new stress-strain behaviour model, evidently providing an improved reflection of actual chain interactions. Under the condition presented in figure 6.1 it is not possible to match the stress response throughout the entire strain range. By fitting the curve for lower strains the model overpredicts the stress response at higher strains. Under the conditions presented in figure 6.2 however, the lengthening free chain length and therefore the number of monomers between crosslinks predicts the stress response across the entire strain range with high accuracy.

As prescribed in chapter 5, the experimental data was obtained using the lowest possible strain rate of 0.001 s^{-1}. This is assumed to approximate the equilibrium stress-strain response. Therefore both of these equilibrium model simulations are run at strain rates of zero, ignoring any viscous effects.

The adjustable model parameters to fit the experimental data in figure 6.1 and figure 6.2 are summarised in table 6.1. The initial soft segment volumetric fraction V_{s0} is set according to the mixing ratio while the soft segment saturation volumetric fraction is always set to 1 for both simulations.

Table 6.1: The curve fitting parameters for stress-strain models with static vs evolving number of monomers between crosslinks.

Model Type	A	μ	N_0	N_s
Static N	20	1.55	36	-
Evolving N	20	1.55	24	44

6.1.2 Loading History

The loading history phenomenon is presented with experimental data in figure 6.3 where only the sample's extension cycles are recorded. Figure 6.4 presents the simulated model were by subsequent extension resume the V_s and N associated with the maximum previously experienced strain.

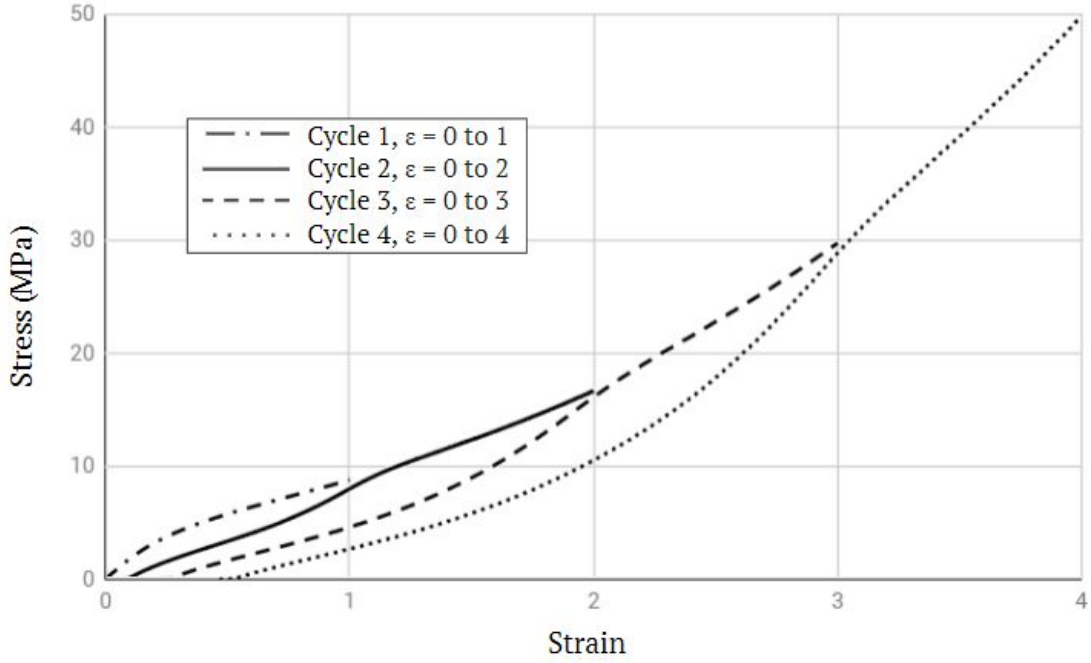

Figure 6.3: TPU's dependence on loading history from experimental data.

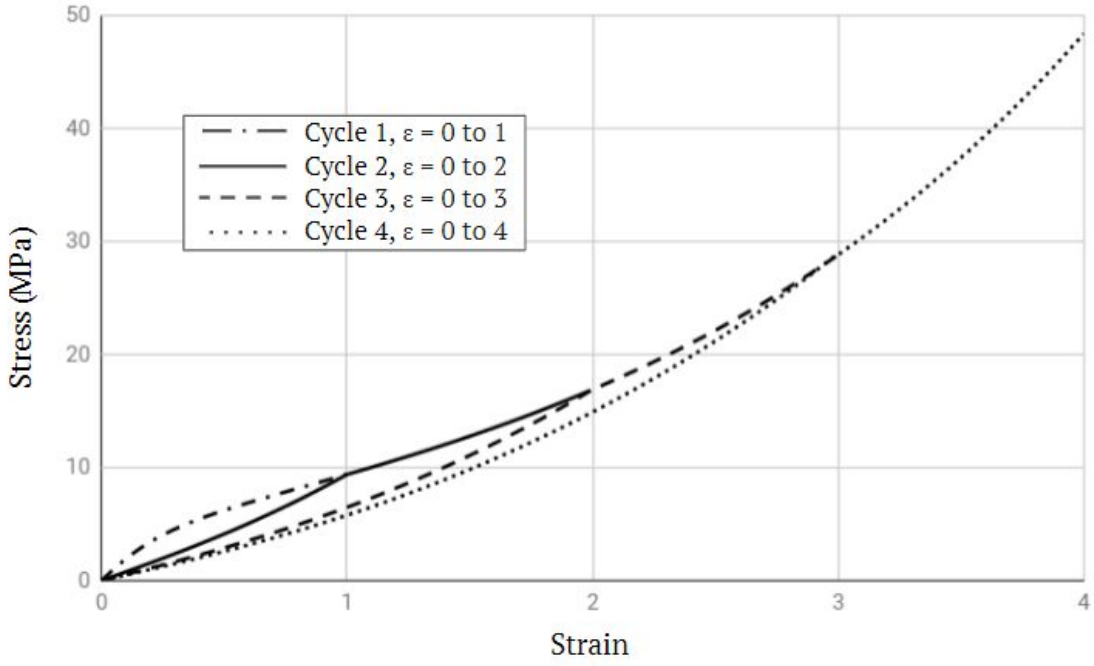

Figure 6.4: The simulated model of cyclic loading capturing TPU's dependence on loading history.

As discussed in chapter 3 and shown in figure 6.4, the simulated model clearly does not capture the residual strain as observed in the experimental data. As a result, the model overpredicts the stress response during secondary strains. The simulation does, however, closely match the experimental data once the previous maximum strain is surpassed.

Table 6.2 provides the fixed inputs to create the cyclic stress-strain response presented in figure 6.4. These normally evolving values (V_s and N) are determined by assessing the normal stress-strain curve at each of the specified strain intervals. Thereafter these inputs are statically used for subsequent extensions until the previous maximum strain is surpassed.

Table 6.2: The soft segment fraction and the number of monomers between crosslink used to simulate the secondary cyclic extensions.

ε	**100%**	**200%**	**300%**
V_s	0.85	0.95	0.98
N	22.91	26.40	27.68

From figure 6.3 the large difference between the stress in the third and fourth cycle suggests that there is still significant softening happening between the elongation of 200 to 300%. The model, however, shows only 0.03% change in soft segment fraction between these two strain intervals. Suggesting that the model may be overestimating the rate of hard segment dissociation.

6.1.3 Viscous Behaviour

As discussed in chapter 3 TPU's exhibit a viscous component, where the stress-strain behaviour is affected by the strain rate. Figure 6.5 presents the experimental data that exhibits this strain rate dependence. Figure 6.6 provides the proposed simulated model of the stress-strain behaviour for the same changes in strain rate.

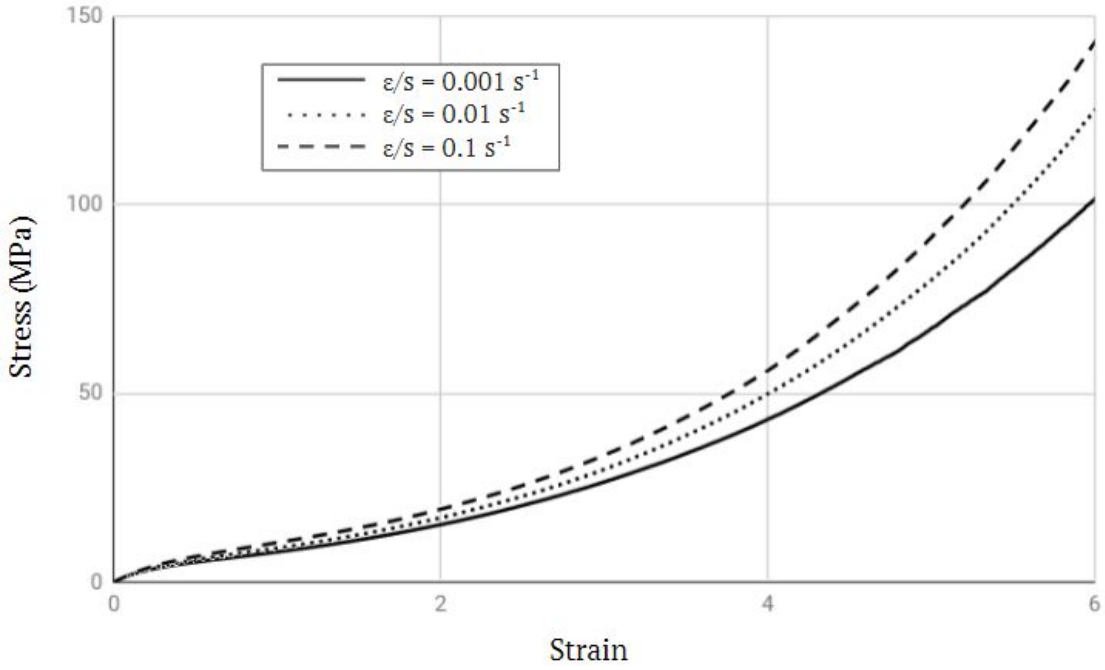

Figure 6.5: The experimental data representing the stress-strain behaviour of Pellethane® 2363-80AE at different strain rates.

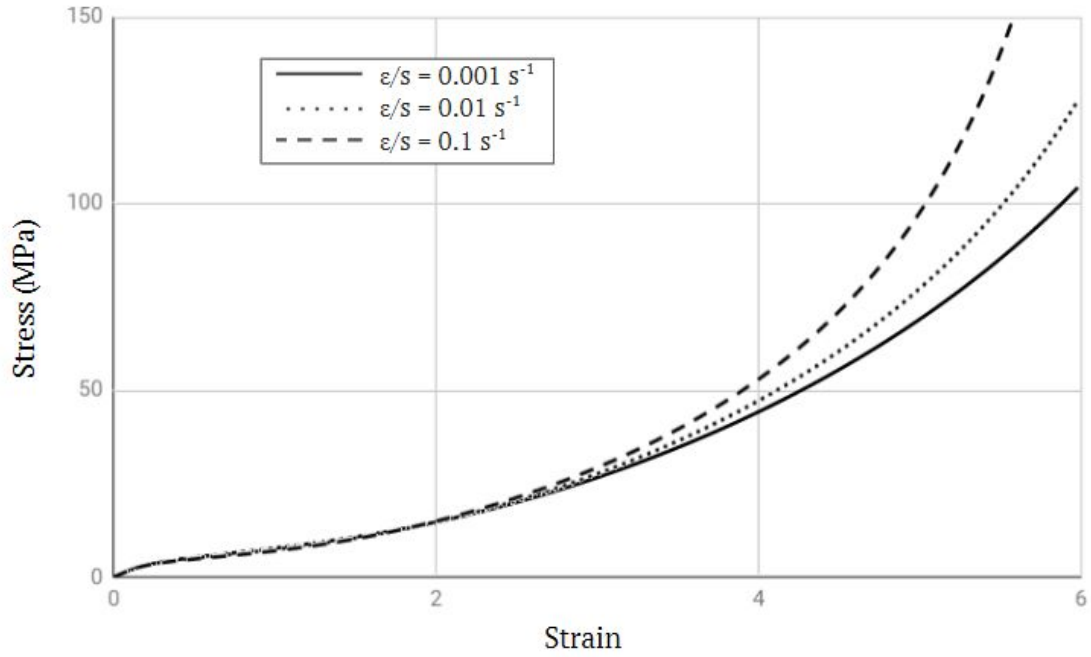

Figure 6.6 The model simulation representing the stress-strain behaviour of Pellethane® 2363-80AE at different strain rates.

The proposed model successfully captures the stress response for both the 0.001 and 0.01 s^{-1} strain rates using a viscous factor of 130. The model, however, overestimates the stress response for the 0.1 s^{-1} strain rate. The proposed model assumes infinite heat transfer and therefore constant specimen temperature, which is not representative of reality. As the strain rate increases the heat produced has less time to dissipate resulting in higher specimen temperatures. Higher temperatures, result in lowered chain network viscosity and lowered force required to dissociate hydrogen bonds, both of which reduce the stress response to a particular strain. This may be the reason why the model overestimates the stress response when strained at a rate of 0.1 s^{-1}. To highlight this phenomenon, extension tests were conducted at 0.75 s^{-1} and compared to that of 0.1 s^{-1} as presented in figure 6.7. This dependence on strain rate emphasises the importance of selecting an appropriate test waveform type when conducting fatigue tests.

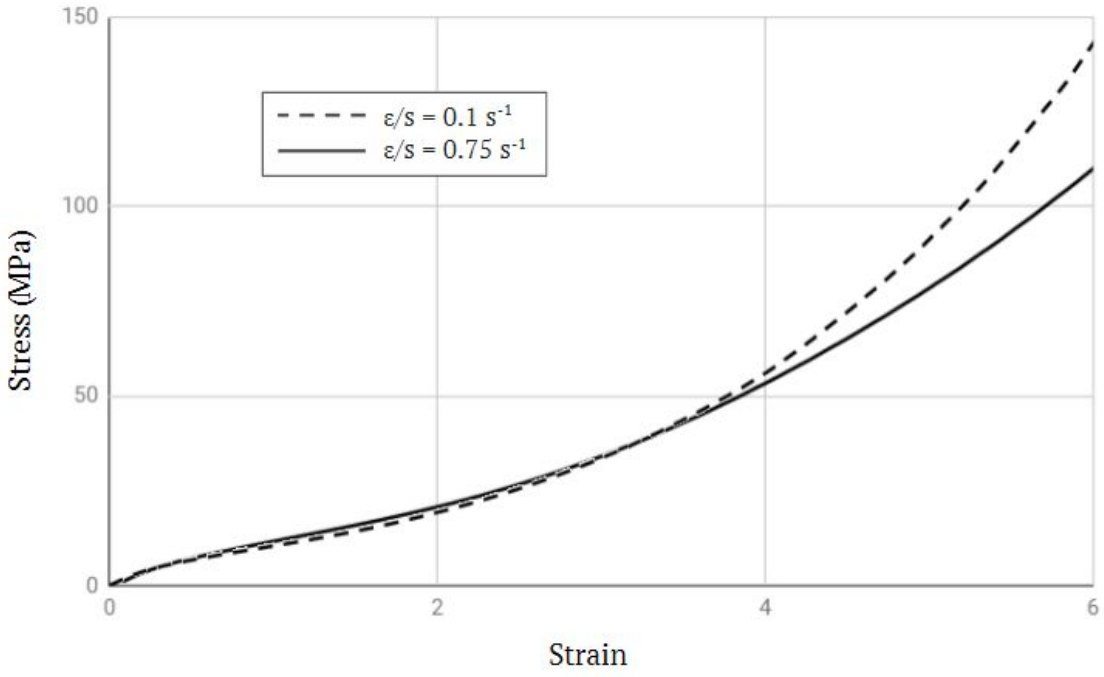

Figure 6.7: Experimental data exhibiting the counter-intuitive reduction in stress response to strain at relatively high strain rates.

In figure 6.7 the higher strain rate produces a lowered stress response to the same strains due to the increased specimen temperature. It can be deduced that there is an inflexion point where a specific strain rate produces the maximum possible stress response (in this case somewhere between 0.1 and 0.75 s^{-1}). The environmental conditions affect both the test specimen temperature and heat transfer, making them important factors to consider when conducting fatigue tests.

6.2 Machine Results and Discussion

This section presents and assesses the test results required to both verify the performance of and demonstrate the capabilities of the developed microtensile specimen fatigue tester. This section focuses on the linear actuator control for generic disturbances, standard waveforms and customised waveforms. Thereafter the force response data acquisition and accuracy is assessed, as well as the control of the testing environment. Finally, the machine is validated with a simulated use test demonstrating all the design features as a whole.

6.2.1 Motion Control

The Proportional, Integrative and Derivative coefficients are adjustable as described in the experimental design chapter. Firstly the unloaded system was subjected to low PID coefficients with the corresponding trimpot set to 9,9 and 9 respectively. This overdamped condition is presented in figure 6.8.

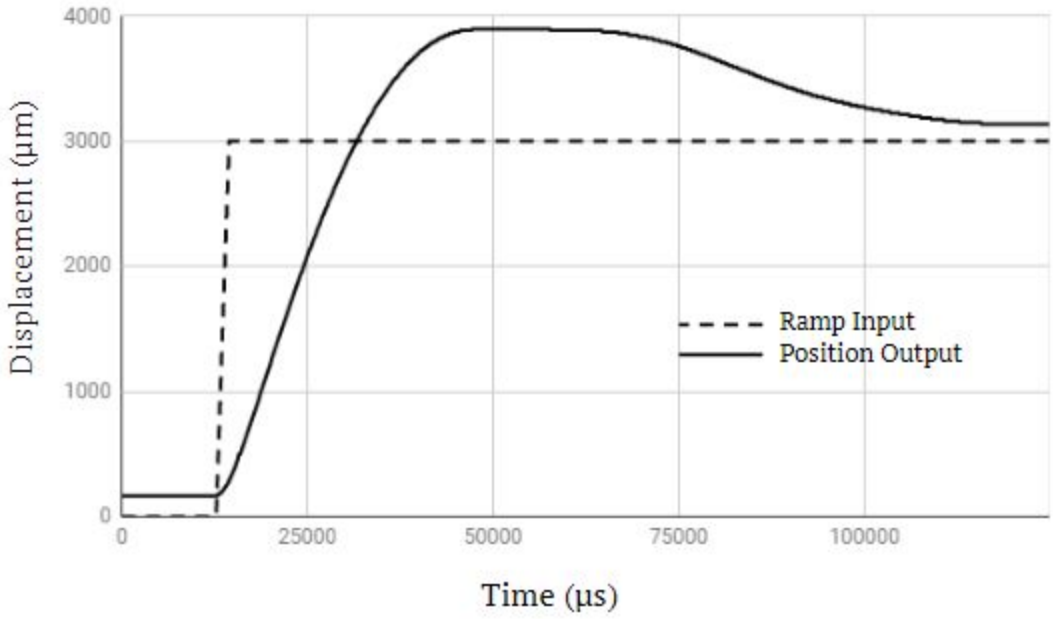

Figure 6.8: The overdamped fatigue tester response to a rapid ramp function with the PID coefficients of 9, 9 and 9 respectively.

Thereafter the PID coefficients were adjusted up to 11, 11 and 11 respectively, to reduce the system damping. This resulted in an underdamped system presented in figure 6.9.

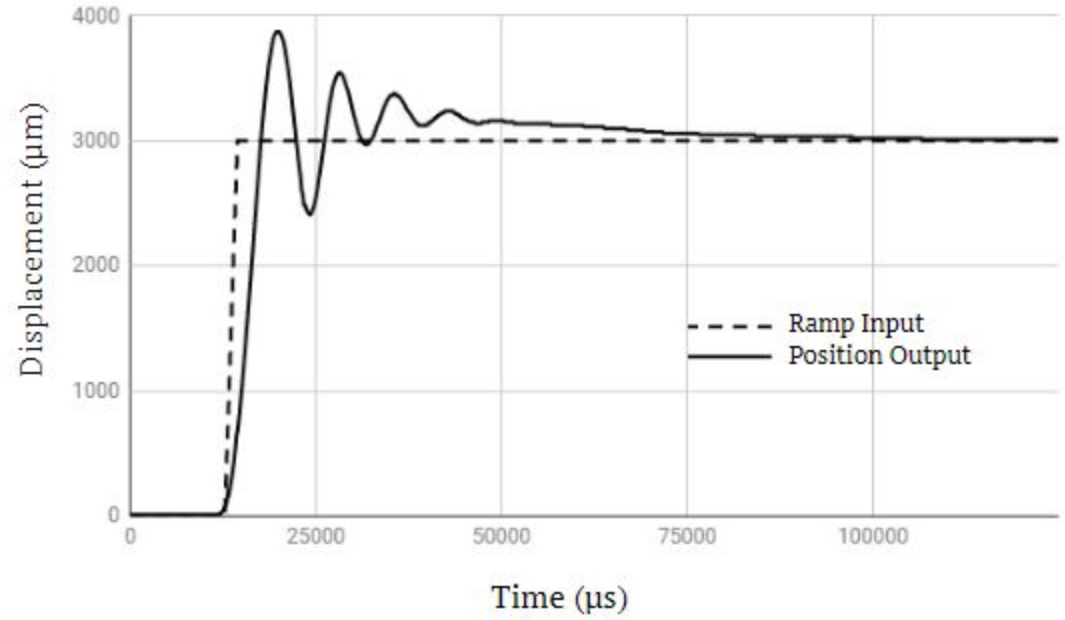

Figure 6.9: The underdamped fatigue tester response to a rapid ramp function with the PID coefficients of 11, 11 and 11 respectively.

PID coefficients of 10, 10 and 10 were consequently chosen in an attempt to find the critically damped condition, this response to the ramp function is presented in figure 6.10.

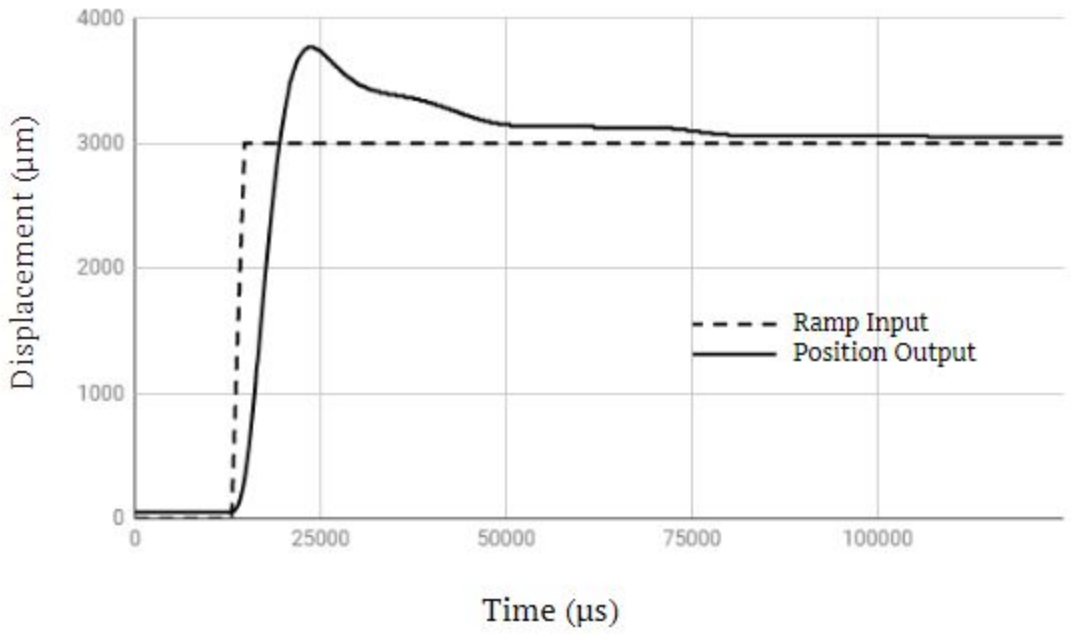

Figure 6.10: The critically damped fatigue tester response to a rapid ramp function with the PID coefficients of 10, 10 and 10 respectively.

Further improvements in both settling-time and overshoot were subsequently achieved by testing small PID coefficient permutations from the 10, 10 and 10 conditions. Proportional, integrative and derivative coefficients of 9.5, 9.5 and 9.5 produced the optimum response as presented in figure 6.11.

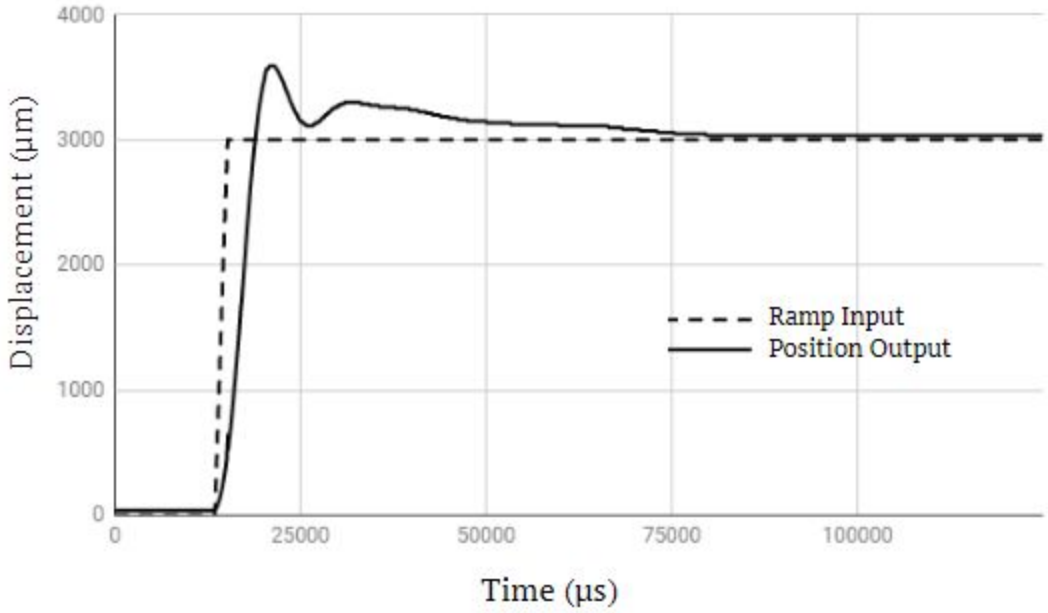

Figure 6.11: The refined critically damped fatigue tester response to a rapid ramp function with the PID coefficients of 9.5, 9.5 and 9.5 respectively.

The system response to the virtually instant ramp function provides insight into the motor's maximum speed capability which is well over what is prescribed in the user needs for the fatigue tester (20 Hz, 6 mm). It was further shown that the appreciable setpoint overshoot did decrease as the ramp function velocity decreased. The relatively long settling time presented in figure 6.11, would theoretically be eliminated by increasing the integrative coefficient. This system proved to be very sensitive to these integrative changes and slight reductions in settling time was invariably coupled with multiple oscillations which was deemed unfavourable in the fatigue testing application. It must be noted that these motor control tests were conducted in the unloaded condition and when loaded with test samples less overshoot is expected during the critical extending stroke.

6.2.2 Motion Capabilities

The onboard waveform selection inputs were utilised to assess the ability to generate the three test waveforms; Triangular Sinusoidal and Square. These test results are presented in figure 6.12, figure 6.13 and figure 6.14, respectively.

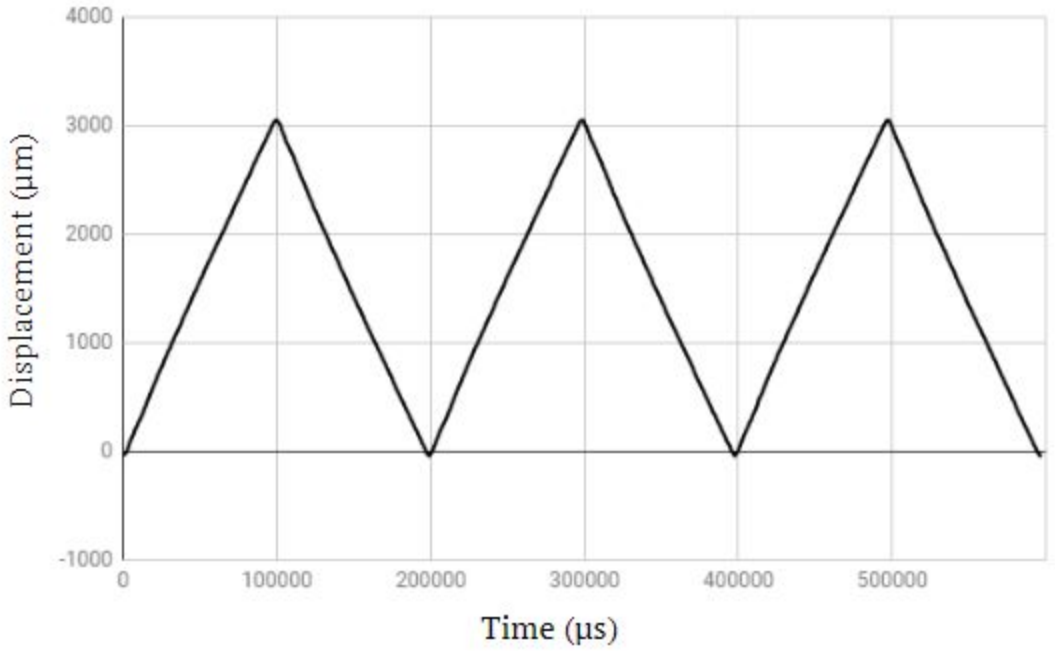

Figure 6.12: The fatigue tester's positional recording during an unloaded triangular waveform actuation with the test parameters of 3 mm amplitude and 5 Hz test frequency.

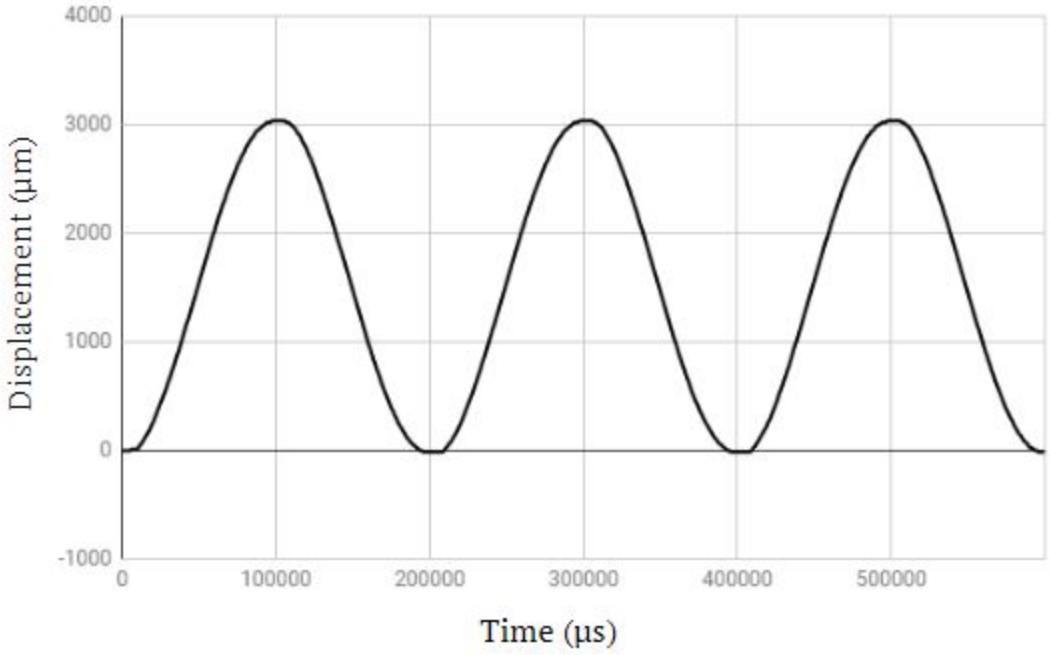

Figure 6.13: The fatigue tester's positional recording during an unloaded sinusoidal waveform actuation with the test parameters of 3 mm amplitude and 5 Hz test frequency.

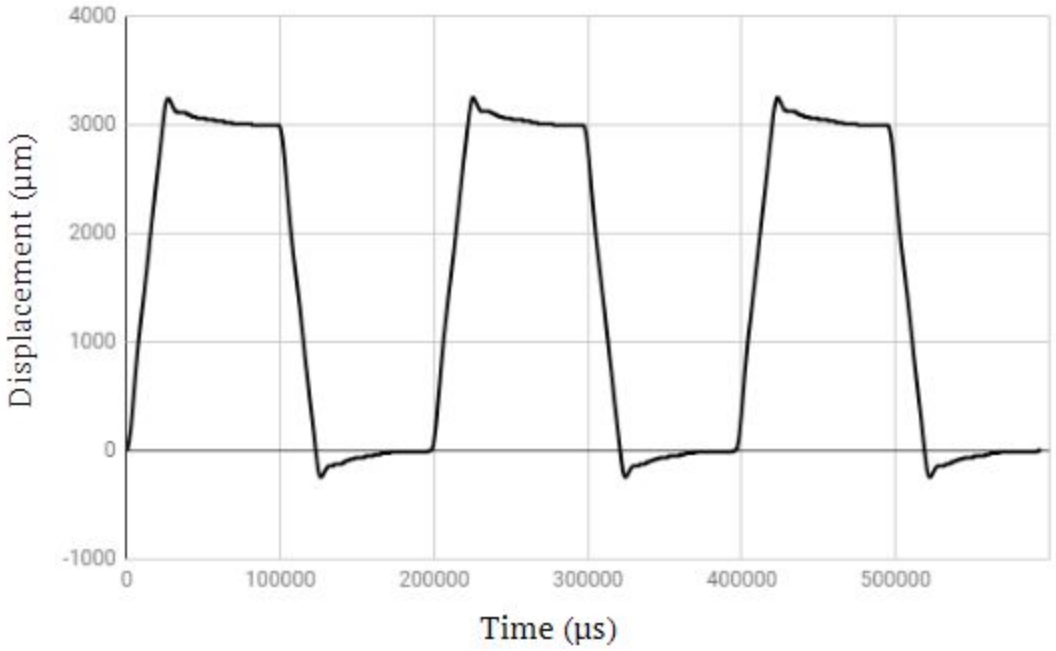

Figure 6.14: The fatigue tester's positional recording during an unloaded square waveform actuation with the test parameters of 3 mm amplitude and 5 Hz test frequency.

At the test parameters utilised to demonstrate the different waveforms (3 mm at 5 Hz) both the triangular and sinusoidal waveforms follow the setpoint with high accuracy, exhibiting merely 1.6 and 1.2% overshoot respectively. The Square waveform, however, is designed in such a way to always maximise the ramp function speed whilst remaining within 10% overshoot, in this case, 8.3% overshoot is observed.

The waveforms are tested at the most demanding unloaded conditions to assess the full parameter input range, both the triangular and sinusoidal waveform can perform across the full range at the maximum test frequency of 20 Hz. Where the triangular and sinusoidal waveform exhibits 9.7% and 6.4% overshoot respectively. To preserve the minimum 50% rest duty cycle in the square waveform the maximum test frequency is limited to 10 Hz. The sinusoidal waveform is a low impulse repetitive waveform and therefore is expected to present the least overshoot, figure 6.15 presents the displacement output at the maximum test conditions (6 mm, 20 Hz). The negligible waveform shape distortion observed in figure 6.15 and relatively lower positional overshoot makes the sinusoidal shape the advised waveform for high-frequency fatigue and durability tests.

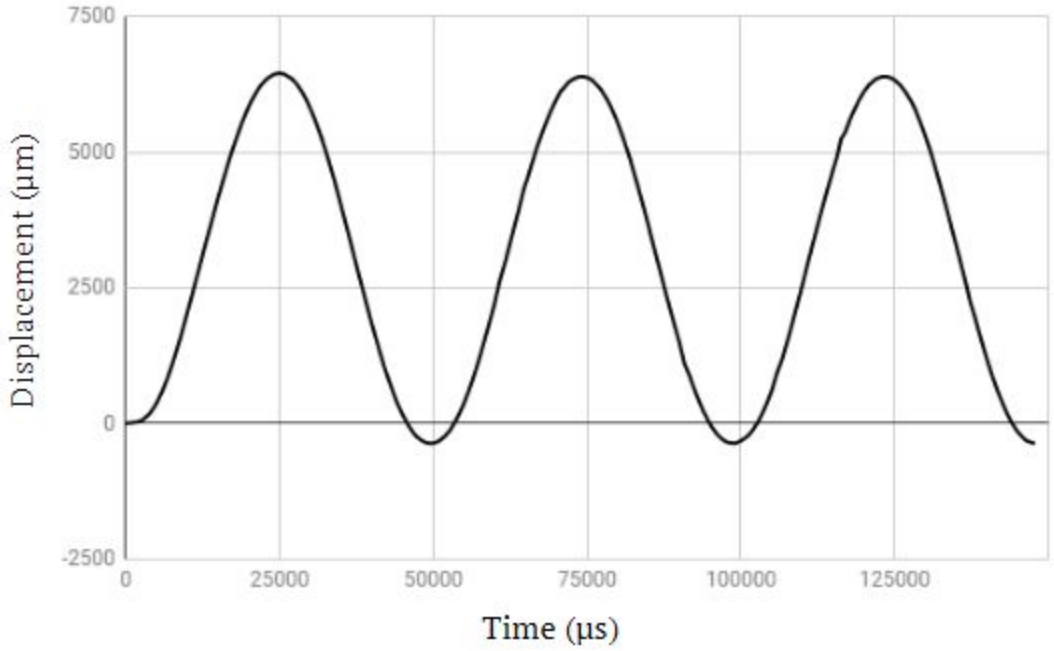

Figure 6.15: The sinusoidal test waveform at the maximum setting for both amplitude and frequency.

6.2.3 Custom Waveform

The feature to simulate custom waveforms is demonstrated in figure 6.16. As described in the experimental design chapter, this repetitive custom waveform represents the strain within a high-risk area in an aortic valve leaflet design during the cardiac cycle. This simulated custom waveform is derived from only 8 points in time within a cardiac cycle, this number can be increased to improve the waveform resolution. This customisable function can be tailored to any repetitive strain for simulation. A customised waveform is of particular relevance when working with materials that present viscous properties, where strain rate is a significant factor to the stress response and ultimately fatigue life.

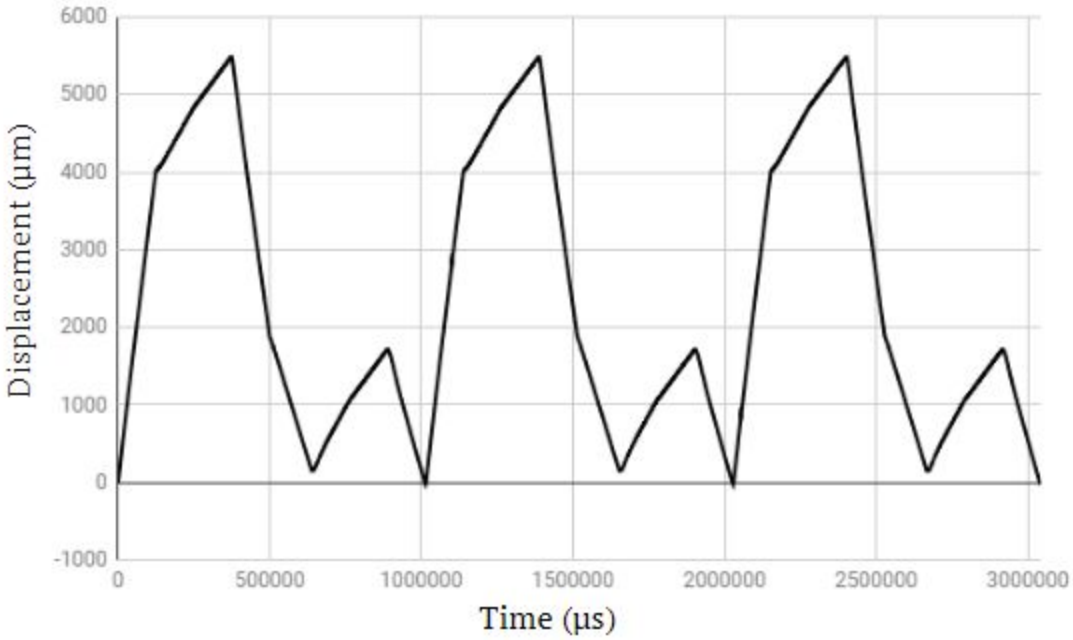

Figure 6.16: The fatigue tester's positional recording during an unloaded custom waveform test.

6.2.4 Data Acquisition Accuracy

During the calibration of the load cells, the steady-state measurement of calibrated lab weights showed an accumulative error of less than 0.2% after digital filtering. However, without the digital filtering and in real-time measurement, significant noise in the force reading data was observed as demonstrated in figure 6.17.

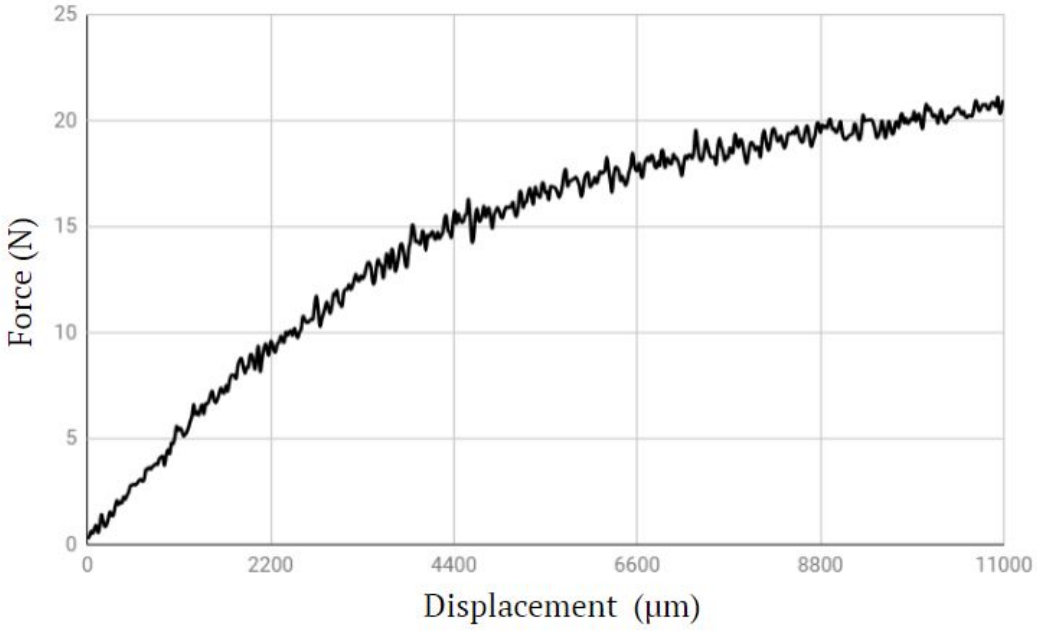

Figure 6.17: The unfiltered force vs displacement curve of a Pellethane® 2363-80AE specimen.

The customised load cell filters as presented in the machine design chapter were designed to accept a step frequency that dictates the filter bandwidth. This frequency was digitally generated by Arduino 1 and commonly connected to each of the 12 load cell filter's bandwidths dictating input pin. This feature did not function as intended due to the summed input impedance across all the common filter bandwidth pins. Therefore the load cell system does not include adequate analogue filtering, hence, the excessive load cell noise presented in figure 6.17.

Digital filtering was applied to the developed fatigue tester data to reduce noise. After which the fatigue tester and a certified 5544 Instron tensile tester was compared in terms of force readings as presented in figure 6.18. Analysing the force error, as per the method described in the experimental design chapter, provides an average error of 8.2%.

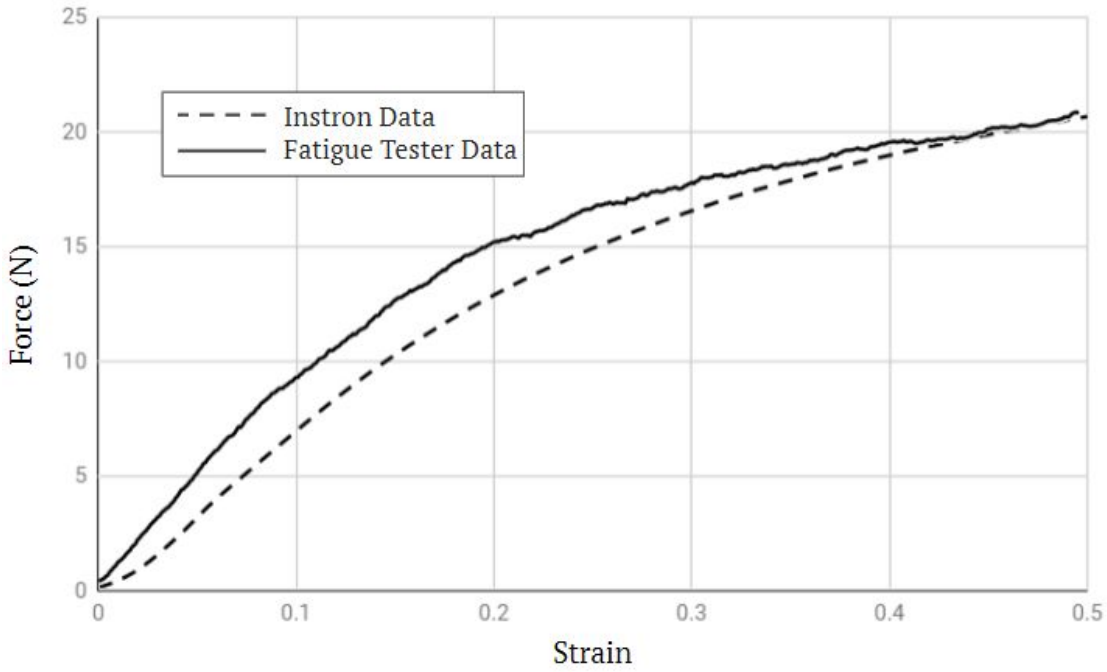

Figure 6.18: The Instron and fatigue tester's recorded force measurements during the extension of a Pellethane® 2363-80AE micro tensile dogbone specimen.

This error can be partially accounted for when the displacement vs time curves are assessed as presented in figure 6.19. The Instron's mechanical system does not allow for rapid acceleration like that of the fatigue testers voice coil, resulting in the Instron lagging the fatigue testers velocity for the first 0.1 s. As discussed throughout this report, the stress-strain behaviour is dependant on the strain rate or extension velocity which may account for the deviation in the force response between the two systems.

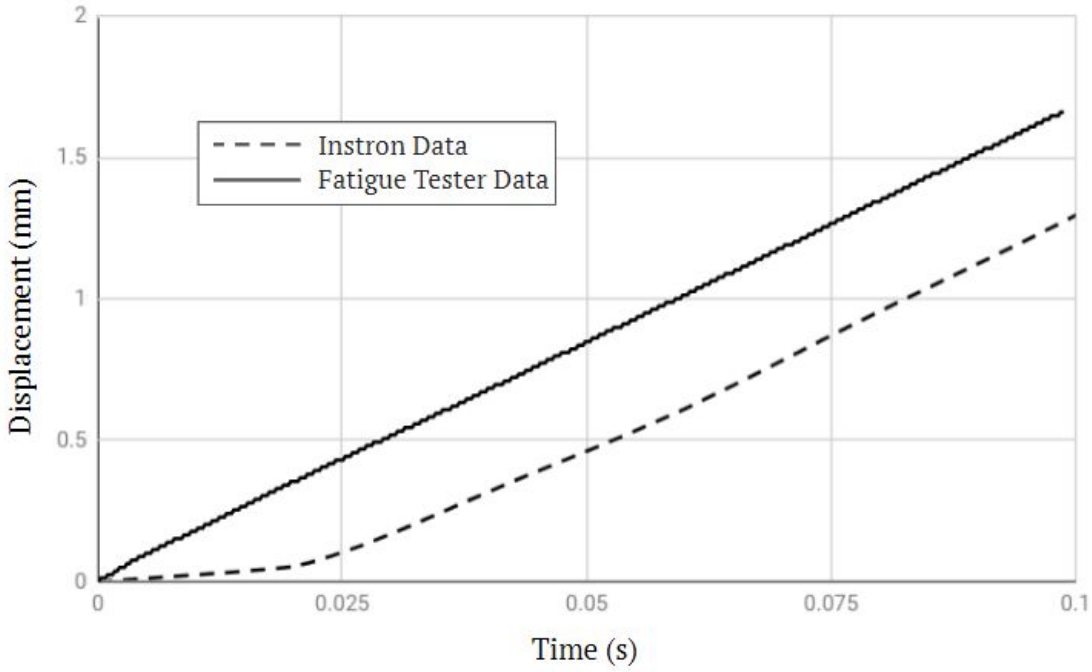

Figure 6.19: *The initial extension position comparison between the fatigue tester and the Instron.*

6.2.5 Environmental Control

The fluid bath test environment was assessed for splashing across a range of test frequency at the maximum standard amplitude of 6 mm with a triangular waveform, these results are presented in table 6.3, where the grading descriptions can be seen in the experimental design chapter.

Table 6.3: The grade of fluid disturbances at specific test frequencies.

Test Frequency (Hz)	Fluid Disturbance Grade
1	Negligible
5	Negligible
10	Mild
15	Mild
20	Moderate

The fluid in the test environment presented surprisingly little disturbance across the test frequencies with no apparent resonance matching to cause significant splashing. Although the fluid disturbances were surprisingly docile, even at high test frequencies, it is advised to limit the frequency parameter to 15 Hz when doing extended fatigue tests in corrosive solutions, to avoid damage to the load cells and fatigue tester base.

The temperature heating and environmental control system was tested, as described in the experimental design chapter. Figure 6.20 presents the time to heat up the environmental fluid to the maximum prescribed temperature of 50 °C.

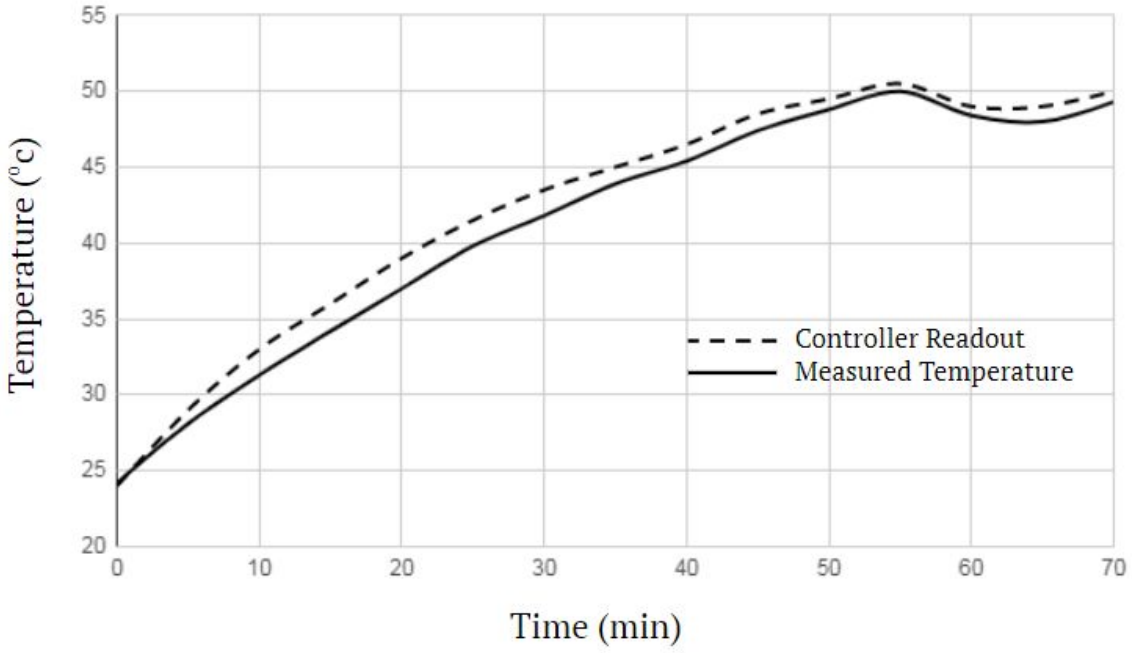

Figure 6.20: The environmental fluid bath temperature during heat up measured both externally and via the controller's feedback system.

The controller readout unintuitively measured slightly higher than the thermometer reading, despite the thermometers central position over the heating pad versus the controller's feedback sensor positioned on the perimeter of the fluid bath (not directly above the heating pad). The discrepancy is possibly due to the removal of the thermometer during momentary temperature readout. Despite this slight discrepancy, the temperature controller in conjunction with the heating pad successfully rose the environmental fluid to 50 °C in an hour and maintained the temperature within 2.5 °C of the setpoint. Note it will take an estimated 20 min to get to the commonly prescribed temperature of 37 °C, this lead time should be considered when setting up a test. To reduce the heat up lead time, preheated fluid may be added to the environmental fluid bath leaving the control system to merely maintain the test environment temperature. To avoid thermal shock to the fluid bath it is imperative to ensure that there is liquid in the fluid bath before initiating the heat up process.

6.2.6 Simulated Use

The simulated use test is initiated to evaluate and validate the fatigue tester as a whole system. Table 6.4 provides the checklist summary of the assessed aspects with the corresponding comments.

Table 6.4: The summary of the auxiliary outcomes of the simulated use test.

Subject of Assessment	**Commentary**
Sample loading	Fatigue tests typically require infrequent reloading, therefore, the relatively lengthy loading step is deemed adequate.
Test specimen pre-tensioning	Individually adjustable specimen tension proved essential to zero test samples despite imperfect specimen loading.
Parameter selection (GUI)	The LCD prompts guided the push-button controlled parameter selection and test initiation as intended.
Environmental chamber positioning	The placement and fastening of the test environmental chamber required two operators, deemed sufficient for infrequent use.
Specimen slippage	No test specimen slippage within the dogbone clamps was observed upon post-test inspection.
Data storage	The test data was correctly recorded and stored on the SD card in the correct file location for post-test analysis.

The simulated use test processed output data provides the average peak force decay of the test specimens as time progress as presented in figure 6.21, as well as the typical peak stress versus a number of cycles fatigue assessment visualisation as presented in figure 6.22.

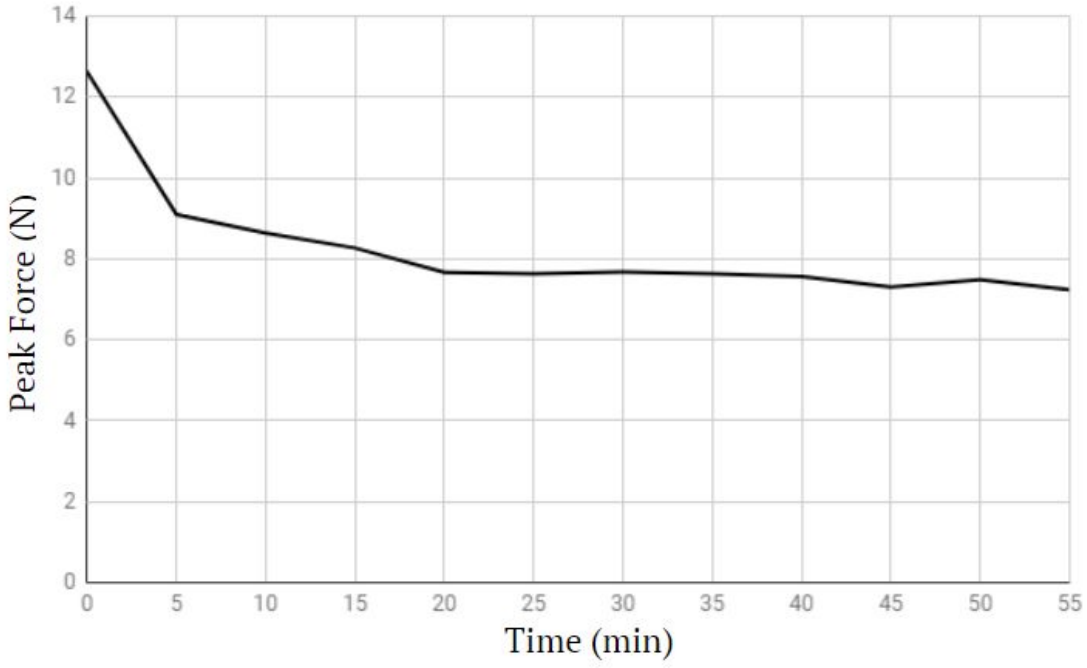

Figure 6.21: *The peak force decay with time of Pellethane® 2363-80AE, tested with a sinusoidal waveform at a frequency of 5 Hz and amplitude of 6 mm.*

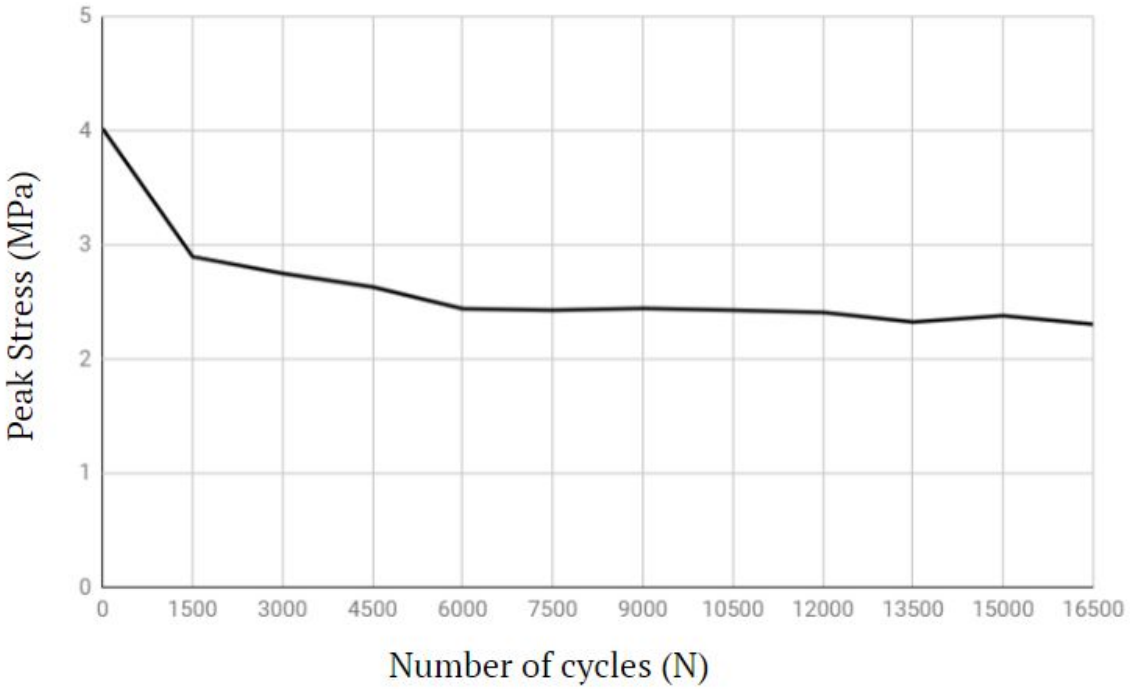

Figure 6.22: The peak stress decay with the number of cycles of Pellethane® 2363-80AE, tested with a sinusoidal waveform at a frequency of 5 Hz and amplitude of 6 mm.

It can be observed that under the specific test conditions (6 mm, 5 Hz, sinusoidal) the peak stress starts to plateau after approximately 6000 cycles. Although this test setup would provide invaluable insight into material durability, it is important to note that in the specific application of the aortic heart valves, the valve leaflets are not subjected to a constant repetitive strain but rather constant stress due to chaining pressure.

7 Conclusion

This investigation aims to develop two critical tools to guide the design and verification of materials tailored for flexible heart valve applications. The first of which is an analytical model to accurately describe the stress-strain behaviour of suitable flexible heart valve materials, specifically thermoplastic polyurethane. The second tool is a multi-stationed micro-tensile specimen fatigue tester to assess the durability of the developed materials.
This chapter supplies separate conclusions on both the material model and the fatigue tester, highlighting both the significance and the limitations within these tools. Finally, this chapter is closed with a concluding statement pertaining to the project as a whole.

7.1 Material Model

The presentation of the equilibrium stress-strain model simulations and experimental data in chapter 6 reveals that the proposed material model extension significantly improves the stress prediction accuracy at higher strains. Additionally exhibiting an exceptional match to the experimental data throughout the strain range. This model extension successfully includes the evolution of the number of monomers between crosslinks during material straining, as described in chapter 2.

The inclusion of an evolving number of monomers between crosslinks created a base to include the theory of entanglement into the material model, ultimately capturing the strain rate dependence. This allowed for the unification of the equilibrium and viscous response into a single interdependent network of expression. This strain rate encompassing model successfully predicted the stress response to different strain rates with high accuracy at the lower strain rates as presented in chapter 6.

7.1.1 Limitations of the model

The proposed model may overestimate the dissociation of hard segment or softening effect. The assessment of the experimental cyclic loading presented continued signs of softening beyond the model's predictions.

The viscous effect model inclusion overestimates the stress response at high strain rates due to an unaccounted for, increase in internal temperature.

7.1.2 Model’s contribution to scientific knowledge

The novel concept of disassociated hard segments contributing to the free chain length and thus causing an increase in the average number of monomers between crosslinks, has improved the understanding of topological interaction within thermoplastic polyurethane material. This

concept can potentially be extended to more material types where crosslinking is achieved through reversible non-covalent bonds.

The proposed unified equilibrium and viscous model will provide a more accurate backbone for finite element modelling in dynamic, rate dependent environments.

In chapter 2, the geometric method developed to convert macroscopic stretch into chain stretch allows for the enhanced understanding of the material mechanics, aiding researchers to develop materials with specific features and applications in mind.

7.2 Fatigue Tester Machine

The machine is able to accurately produce both triangular and sinusoidal displacement test waveforms up to frequencies of 20 Hz with less than 10% positional overshoot, and up to 10 Hz for square waveforms.

The appropriate additional features such as individually adjustable specimen tension and live readout, the externally mounted environmental bath heating source and the onboard SD card storage all combine to create a robust unique and easy to use fatigue testing tool.

The novel feature for custom waveform testing is successfully implemented as demonstrated in chapter 6. This feature allows for application tailored fatigue testing to improve the representation and validity of fatigue data.

7.2.1 Limitations of the fatigue tester

Although well-compensated through digital filtering, the analogue load cell force response signal noise does reduce the accuracy of the obtained data.

7.2.2 Fatigue tester’s contribution to scientific knowledge

The developed fatigue tester will accommodate researchers in understanding the effects of the waveform, frequency, amplitude and temperature on the materials in question, providing critical insight into material durability and the mechanisms of fatigue failure.

7.3 General Conclusion

The material model accurately unifies the equilibrium and viscous stress-strain behaviour of thermoplastic polyurethane materials. This model provides a deeper understanding of the molecular chain mechanics within thermoplastic polyurethane and other polymeric materials of a similar nature. The fatigue tester machine was successfully designed, assembled and programmed to fulfil the critical user needs. With the inclusion of the customisable waveform feature, the fatigue tester machine is capable of providing invaluable material durability

information. It is thus concluded that two essential scientific tools have been successfully developed to guide the design and verification of materials tailored for flexible heart valve applications.

8 Recommendations

This chapter presents the proposed model extensions, machine design upgrades and future tests to further validate the material model. The implementation of these recommendations would improve the developed tools to accommodate the design and testing of suitable materials for an aortic heart valve and many more similar applications.

8.1 Model Extension

In the material model section, the conjecture of streamlining is introduced. The phenomenon of softening is when the hard segment disassociation caused by prior extension softens the material for subsequent extensions, therefore creating a loading history dependence. As an analogous concept, it is suggested that the viscous response is also dependant on the loading history and that the disentanglement interactions also reduce in subsequent extensions of the material. It is thus recommended to further investigate this conjecture, potentially improving the overall understanding of the viscous behaviour exhibited by the materials in use and polymers in general.

The material model proposed assumes infinite heat dissipation and therefore incorrectly predicts the material stress-strain response at high strain rates where heat generation and lack of dissipation become significant. It is recommended to incorporate the temperature component into the material, by determining how the temperature affects the material viscosity and the hard segment disassociation force. An improved understanding of the temperature dependence to a materials stress-strain behaviour would facilitate an improved representation of data when testing at higher frequencies. The test design could compensate for increased heat generation at higher frequencies by increasing heat dissipation through the cooling of the specimen's environment.

8.2 Machine Upgrade

To improve the overall fatigue tester's accuracy, it is recommended to utilise the capacitor dictating bandwidth function, as opposed to the currently utilised step signal function input. This should reduce the load cell noise observed during live recording and therefore improve force measurement accuracy. Secondly, it is recommended that the positional setpoint overshoot is compensated by digitally offsetting the setpoint until the output position perfectly matches the selected amplitude.

To improve the fatigue tester's flexibility it is recommended to fit the load cell signal amplifiers with an adjustable potentiometer as opposed to a fixed resistor, therefore allowing the operator to tune the amplification according to the expected load. This will ultimately increase the test load range without compromising on the resolution during measurement of smaller loads.

To improve the fatigue tester's ease of use, it is recommended to accommodate onboard creation of custom waveforms through the machine GUI, as opposed to the current method that requires code manipulation, restricting this function to skilled operators. Secondly, it is recommended to simplify the height adjustable environmental chamber platform, to avoid requiring two operators for positioning.

To improve the square waveform test range to the prescribed 20 Hz it is recommended to digitally simulate rounded edges on the square waveform to reduce the impulse and thus positional overshoot in the square waveform.

To increase the fatigue tester's scope it is recommended to develop a stress-controlled fatigue testing feature. This would require averaging the stress among identical specimens and with a staged approach adjusting the extension in an attempt to maintain relatively constant peak stress throughout the specimen's fatigue life. Stress-controlled fatigue testing is more representative in cases where materials are subjected to cyclic pressures as in the scenario of aortic heart valve leaflets.

As an additional feature, it is recommended to include a software data check to detect specimen breakage, and detect failure onset or initiation by following predetermined failure trends. Pausing the fatigue tests at signs of failure onset would provide the opportunity to observe the crack initiation site before the catastrophic failure occurs. This information would provide critical insight to guide the material development for the aortic heart valve leaflets.

8.3 Supplementary Testing

Additional testing is recommended where a matrix of varying test parameters in waveform, amplitude and frequency is to be compared. During these tests, hysteresis, peak stress and residual strain should be assessed. These results should guide the test parameter selection to best represent the intended application when setting up fatigue life tests. This data should also be used to further validate the proposed viscous model presented in this report.

Heart valve leaflets could be produced from an array of material and therefore it is recommended to extend the testing to a variety of thermoplastic polymers. This will also provide a basis to assess the material model across a range of materials with similar topological construction.

9 References

Ang, K., Chong, G. and Li, Y. (2005). PID control system analysis, design, and technology. *IEEE Transactions on Control Systems Technology*, 13(4), pp.559-576.

Arruda, E. and Boyce, M. (1993). A three-dimensional constitutive model for the large stretch behavior of rubber elastic materials. *Journal of the Mechanics and Physics of Solids*, 41(2), pp.389-412.

Brei, T. (2019). *How low pressure transducers work*. [online] Sure Controls. Available at: https://www.surecontrols.com/how-low-pressure-transducers-work/ [Accessed 6 Feb. 2019].

Chen, Y., Fuh, C. and Tung, P. (2005). Application of voice coil motors in active dynamic vibration absorbers. *IEEE Transactions on Magnetics*, 41(3), pp.1149-1154.

Coleman, M. and Painter, P. (1998). *Fundamentals of Polymer Science.* 2nd ed. CRC Press, pp.1-60.

Cypress Semiconductor Corporation (2010). *Quadrature Decoder*. [online] Cypress Semiconductor Corporation. Available at: https://www.cypress.com/file/131871/download [Accessed 6 Feb. 2019].

Czech, P., Okrasa, L., Méchin, F., Boiteux, G. and Ulanski, J. (2006). Investigation of the polyurethane chain length influence on the molecular dynamics in networks crosslinked by hyperbranched polyester. *Polymer*, 47(20), pp.7207-7215.

Delphi Technologies Inc (1997). *Rotary position transducer and method*. US6374664B1.

Dynapar.com. (2019). *Quadrature Encoder - Dynapar*. [online] Available at: https://www.dynapar.com/technology/encoder_basics/quadrature_encoder/ [Accessed 5 Feb. 2019].

Edwards, S. and Vilgis, T. (1988). The tube model theory of rubber elasticity. *Reports on Progress in Physics*, 51(2), pp.243-297.

Ekelof, S. (2001). The genesis of the Wheatstone bridge. *Engineering Science & Education Journal*, 10(1), pp.37-40.

Emerywinslow.com. (2019). *Emery Winslow Scale Company - Industrial Scales - Hydrostatic Load Cells For Harsh Environments*. [online] Available at: http://www.emerywinslow.com/technology.html [Accessed 6 Feb. 2019].

Estes, G., Seymour, R. and Cooper, S. (1971). Infrared Studies of Segmented Polyurethane Elastomers. II. Infrared Dichroism. *Macromolecules*, 4(4), pp.452-457.

Flory, P. (1949). The Configuration of Real Polymer Chains. *The Journal of Chemical Physics*, 17(3), pp.303-310.

Freltas, L., Burgert, J. and Stadler, R. (1987). Thermoplastic elastomers by hydrogen bonding. *Polymer Bulletin*, 17(5).

Gallagher Custom Polyurethane Molding. (2019). *Polyurethane Coefficient of Friction*. [online] Available at: https://gallaghercorp.com/polyurethane-coefficient-of-friction/ [Accessed 21 Jan. 2019].

Head, S., Çelik, M. and Kappetein, A. (2017). Mechanical versus bioprosthetic aortic valve replacement. *European Heart Journal,* 38(28), pp.2183-2191.

Hepburn, C. (1982). *Polyurethane elastomers*. 2nd ed. London, Applied Science Publishers, 1982: Elsevier.

Huber, J., Fleck, N. and Ashby, M. (1997). The selection of mechanical actuators based on performance indices. *Proceedings of the Royal Society of London. Series A: Mathematical, Physical and Engineering Sciences*, 453(1965), pp.2185-2205.

Janssen, R., de Kanter, D., Govaert, L. and Meijer, H. (2008). Fatigue Life Predictions for Glassy Polymers: A Constitutive Approach. *Macromolecules*, 41(7), pp.2520-2530.

Jedynak, R. (2017). New facts concerning the approximation of the inverse Langevin function. *Journal of Non-Newtonian Fluid Mechanics*, 249, pp.8-25.

Jones, M. (1995). *A practical introduction to electronic circuits*. 1st ed. New York: Cambridge University Press, pp.145-159.

Karam, H. (1959). Flow Properties of Linear Polymers. *Industrial & Engineering Chemistry*, 51(7), pp.851-853.

Keim, R. (2018). *Understanding and Implementing Charge Amplifiers for Piezoelectric Sensor Systems*. [online] Available at: https://www.allaboutcircuits.com/technical-articles/understanding-and-implementing-charge-amplifiers-for-piezoelectric-sensor-s/ [Accessed 6 Feb. 2019].

Kuhn, W. and Grün, F. (1942). Beziehungen zwischen elastischen Konstanten und Dehnungsdoppelbrechung hochelastischer Stoffe. *Kolloid-Zeitschrift*, 101(3), pp.248-271.

Lemire, M., Boni, L. and Furnish, B. (2007). *The difference between electromechanic, fluid-power, and linear-motor actuation*. [online] Machine Design. Available at: https://www.machinedesign.com/archive/difference-between-electromechanic-fluid-power-and-linear-motor-actuation [Accessed 3 Feb. 2019].

Lim, W., Lloyd, G. and Bhattacharyya, S. (2017). Mechanical and surgical bioprosthetic valve thrombosis. *Heart*, pp.heartjnl-2017-311856.

Maganti, K., Rigolin, V., Sarano, M. and Bonow, R. (2010). Valvular Heart Disease: Diagnosis and Management. *Mayo Clinic Proceedings*, 85(5), pp.483-500.

Mayer, J. (1994). High-resolution of rotary encoder analog quadrature signals. *IEEE Transactions on Instrumentation and Measurement*, 43(3), pp.494-498.

Miehe, C. and Keck, J. (2000). Superimposed finite elastic–viscoelastic–plastoelastic stress response with damage in filled rubbery polymers. Experiments, modelling and algorithmic implementation. *Journal of the Mechanics and Physics of Solids*, 48(2), pp.323-365.

Mueller, A. (2011). *Recent advances in robust control*. 1st ed. Rijeka, Croatia: InTech, p.82.

Mullins, L. and Tobin, N. (1966). Stress Softening in Rubber Vulcanizates. Part I. Use of a Strain Amplification Factor to Describe Elastic Behavior of Filler-Reinforced Vulcanized Rubber. *Rubber Chemistry and Technology*, 39(4), pp.799-813.

Mullins, L. (1969). Softening of Rubber by Deformation. *Rubber Chemistry and Technology*, 42(1), pp.339-362.

Musumeci, L., Jacques, N., Hego, A., Nchimi, A., Lancellotti, P. and Oury, C. (2018). Prosthetic Aortic Valves: Challenges and Solutions. *Frontiers in Cardiovascular Medicine*, 5.

Nakayama, Y. (2018). *Introduction to fluid mechanics*. Amsterdam: Butterworth-Heinemann.

Nyce, D. (2019). *Linear Position Sensors: Theory and Application*. 1st ed. Wiley.

Petrovic, Z., Ferguson, J., 1991. Polyurethane Elastomers. *Progress in Polymer Science*, 16, pp.695-836.

Polymerdatabase.com. (2019). *Flow Properties of Polymers*. [online] Available at: http://polymerdatabase.com/polymer%20physics/Viscosity2.html [Accessed 3 Feb. 2019].

PCB GROUP COMPANY (2019). *Load Cell Handbook, A Technical Overview and Selection Guide*. [online] PCB Group, Inc. Available at: http://www.pcb.com/contentstore/MktgContent/LinkedDocuments/Load_Torque/LT-LoadCellHandbook_LowRes.pdf [Accessed 5 Feb. 2019].

Qi, H. and Boyce, M. (2004). Constitutive model for stretch-induced softening of the stress-stretch behavior of elastomeric materials. *Journal of the Mechanics and Physics of Solids*, 52(10), pp.2187-2205.

Qi, H. and Boyce, M. (2005). Stress-strain behavior of thermoplastic polyurethanes. *Mechanics of Materials*, 37(8), pp.817-839.

Sophphx.caltech.edu. (2019). *TLC555 LinCMOS™ Timer.* [online] Available at: http://www.sophphx.caltech.edu/Physics_5/Data_sheets/tlc555.pdf [Accessed 10 Oct. 2019].

Tainstruments.com. (2015). *ElectroForce® 3200 Series III Test Instrument*. [online] Available at: http://www.tainstruments.com/wp-content/uploads/ElectroForce_3200_SeriesIII.pdf [Accessed 4 Feb. 2019].

Tibazarwa, K., Volmink, J. and Mayosi, B. (2008). Incidence of acute rheumatic fever in the world: a systematic review of population-based studies. *Heart*, 94(12), pp.1534-1540.

Tolomatic, Inc. (2014). How to select the best linear actuator type for valve automation in process industries. [online] Available at: https://www.tolomatic.com/info-center/resource-details/selecting-linear-actuators-for-valve-automation [Accessed 8 Apr. 2017].

Vaseghi, S. (2000). *Advanced digital signal processing and digital noise reduction*. 4th ed. Chichester: Wiley.

Wittenberg, E., Meyer, A., Eggers, S. and Abetz, V. (2018). Hydrogen bonding and thermoplastic elastomers – a nice couple with temperature-adjustable mechanical properties. *Soft Matter*, 14(14), pp.2701-2711.

World Health Organization. (2019). *71st World Health Assembly adopts resolution calling for greater action on rheumatic heart disease*. [online] Available at: https://www.who.int/ncds/management/rheumatic-heart-disease-resolution/en/ [Accessed 3 Feb. 2019].

Yau, M., Ei-Ghoneimi, Y.A., Armstrong, S., Ivanov, J. and David, T.E. (2000). Mitral valve repair and replacement in rheumatic disease. *Journal of Thoracic and Cardiovascular Surgery,* 119, pp. 53-60.

Zaman, M., Rouf, M., Haque, S., Khan, L., Chowdhury, N., Razzaque, S., Yoshiike, N. and Tanaka, H. (1998). Does rheumatic fever occur usually between the ages of 5 and 15 years?. *International Journal of Cardiology*, 66(1), pp.17-21.

Appendices

Appendix A

Arduino Code

Arduino 1 (Driving)

```
// libraries to be included
#include <LiquidCrystal.h>

LiquidCrystal lcd(31, 33, 29, 27, 25, 23); //Set up LCD screen

//gui push buttons
const int EB = 49;// check allocation if unresponsive
const int UB = 51;
const int DB = 47;
const int LB = 53;
const int RB = 45;
const int SPB = 39;
const int PB = 41;
const int STB = 43;

const int DP = 3;  //Direction pin
const int SP = 2; //Step pin

//global variables
int AMP = 3000;    //default 3mm, 0.1 increments
int FRE = 10;   // frequency default 10Hz, 1Hz increments
int WAV = 1;     // waveform 1-Triangular 2-Sinusoidal 3-Square
int NS = 1; // number of steps
int DT = 1000; // delay time
int DTM = 50;
int DTR = 5000;
float SDT[600];
float T[600];


int Sres = 127; //use 10 res to keep within ints
float pi = 3.14159;

void setup() {
  Serial.begin(9600);
```

```
 pinMode(SP, OUTPUT);
 pinMode(DP, OUTPUT);
 lcd.begin(16, 2);
 lcd.clear();
 lcd.print("INITILISING");
 lcd.setCursor(0, 1);
 lcd.print("PROCESSOR 1");
 delay(4500);
 pinMode(STB, INPUT_PULLUP);
 pinMode(SPB, INPUT_PULLUP);
 pinMode(PB, INPUT_PULLUP);
 pinMode(RB, INPUT_PULLUP);
 pinMode(UB, INPUT_PULLUP);
 pinMode(EB, INPUT_PULLUP);
 pinMode(DB, INPUT_PULLUP);
 pinMode(LB, INPUT_PULLUP);

 REG_PMC_PCER1 |= PMC_PCER1_PID36;                 // Enable PWM
 REG_PIOB_ABSR |= PIO_ABSR_P16;                    // Set PWM pin peripheral type A or B, in this
case B
 REG_PIOB_PDR |= PIO_PDR_P16;                      // Set PWM pin to an output
 REG_PWM_CLK = PWM_CLK_PREA(0) | PWM_CLK_DIVA(42);    // Set the PWM clock rate to
2MHz (84MHz/42)
 REG_PWM_CMR0 = PWM_CMR_CALG | PWM_CMR_CPRE_CLKA;     // Enable dual slope PWM
and set the clock source as CLKA
 REG_PWM_CPRD0 = 200;                              // Set the PWM frequency 2MHz/(2 * 20000) = 50Hz
 REG_PWM_CDTY0 = 100;                               // Set the PWM duty cycle to 1500 - centre the
servo
 REG_PWM_ENA = PWM_ENA_CHID0;
}

void loop()
{
 StopPinInsert();
}

void StopPinInsert()
{
 lcd.clear();
 lcd.print("INSERT MOTOR");
 lcd.setCursor(0, 1);
 lcd.print("STOP PIN");
 delay(3000);
```

```
  while (1)
  {
    if (!digitalRead(EB))
    {
      LoadSamples();
    }
  }
}

void LoadSamples()
{
  lcd.clear();
  lcd.print("LOAD TEST");
  lcd.setCursor(0, 1);
  lcd.print("SAMPLES");
  delay(3000);
  while (1)
  {
    if (!digitalRead(EB))
    {
      MeasureSamples();
    }
  }
}

void MeasureSamples()
{
  lcd.clear();
  lcd.print("USE LOAD CELL");
  lcd.setCursor(0, 1);
  lcd.print("SWITCHES");
  delay(3000);
  lcd.clear();
  lcd.print("PRESS ENTER");
  lcd.setCursor(0, 1);
  lcd.print("ONCE ADJUSTED");
  while (1)
  {
    if (!digitalRead(EB))
    {
      SetTemp();
    }
    if (!digitalRead(SPB))
```

```
   {
    LoadSamples();
   }
  }
}

void SetTemp()
{
 lcd.clear();
 lcd.print("SHIFT THE HEATER");
 lcd.setCursor(0, 1);
 lcd.print("TEST ENVIRONMENT");
 delay(3000);
 lcd.clear();
 lcd.print("SET THE TEST");
 lcd.setCursor(0, 1);
 lcd.print("TEMPERATURE");
 while (1)
 {
  if (!digitalRead(EB))
  {
   Parameterselect();
  }
  if (!digitalRead(SPB))
  {
   MeasureSamples();
  }
 }
}
void Parameterselect()
{ //PARAMETER SELECT INSTRUCTIONS
 lcd.clear();
 lcd.print("SELECT THE TEST");
 lcd.setCursor(0, 1);
 lcd.print("PARAMETERS");
 delay(3000);
 lcd.clear();
 lcd.print("ADJUST THE TEST");
 lcd.setCursor(0, 1);
 lcd.print("PARAMETERS");
 delay(3000);
 lcd.clear();
 lcd.print("CONFIRM FINAL");
```

```
 lcd.setCursor(0, 1);
 lcd.print("TEST SELECTION");
 delay(3000);

 AMPselect();

}

void AMPselect() { // add selection limits
 bool c = 1;
 while (1) {
  if (c)
  {
   c = 0;
   lcd.clear();
   lcd.print("AMPLITUDE");
   lcd.setCursor(0, 1);
   lcd.print(String(AMP) + " um");
   delay(500);
  }
  if ((!digitalRead(UB)))
  {
   c = 1;
   AMP = AMP + 100;
   if (AMP > 6000) {
    AMP = 6000;
    lcd.clear();
    lcd.print("ERROR: MAXIMUM OF");
    lcd.setCursor(0, 1);
    lcd.print("6000 um");
    delay(3000);
   }
  }
  if ((!digitalRead(DB)))
  {
   c = 1;
   AMP = AMP - 100;
   if (AMP == 900) { //set minimum amplitude to 1mm (compatible with microsecond delay)
    AMP = 1000;
    lcd.clear();
    lcd.print("ERROR: MINIMUM OF");
    lcd.setCursor(0, 1);
    lcd.print("1000 um");
```

```
      delay(3000);
     }
    }
    if ((!digitalRead(LB)))
    {
     WAVselect();
    }
    if ((!digitalRead(RB)))
    {
     FREselect();
    }
    if ((!digitalRead(EB)))
    {
     CheckTemp();
    }
    if ((!digitalRead(SPB)))
    {
     SetTemp();
    }
  }
}
void FREselect() { // add selection limits
  bool c = 1;
  while (1) {
    if (c)
    {
     c = 0;
     lcd.clear();
     lcd.print("FREQUENCY");
     lcd.setCursor(0, 1);
     lcd.print(String(FRE) + " Hz");
     delay(500);
    }
    if ((!digitalRead(UB)))
    {
     c = 1;
     FRE = FRE + 1;
     if (FRE > 20) {
      FRE = 20;
      lcd.clear();
      lcd.print("ERROR: MAXIMUM OF");
      lcd.setCursor(0, 1);
      lcd.print("20 Hz");
```

```
      delay(3000);
     }
    }
    if ((!digitalRead(DB)))
    {
     c = 1;
     FRE = FRE - 1;
     if (FRE == 0) {
      FRE = 1;
      lcd.clear();
      lcd.print("ERROR: MINIMUM OF");
      lcd.setCursor(0, 1);
      lcd.print("1 Hz");
      delay(3000);
     }
    }
    if ((!digitalRead(LB)))
    {
     AMPselect();
    }
    if ((!digitalRead(RB)))
    {
     WAVselect();
    }
    if ((!digitalRead(EB)))
    {
     CheckTemp();
    }
    if ((!digitalRead(SPB)))
    {
     SetTemp();
    }
  }
}

void WAVselect() { // add selection limits
  bool c = 1;
  while (1) {
    if (c)
    {
      c = 0;
      switch (WAV) {
        case 1:
```

```
      lcd.clear();
      lcd.print("WAVEFORM");
      lcd.setCursor(0, 1);
      lcd.print("TRIANGULAR");
      break;
    case 2:
      lcd.clear();
      lcd.print("WAVEFORM");
      lcd.setCursor(0, 1);
      lcd.print("SINUSOIDAL");
      break;
    case 3:
      lcd.clear();
      lcd.print("WAVEFORM");
      lcd.setCursor(0, 1);
      lcd.print("SQUARE");
      break;
  }
  delay(500);
}
if ((!digitalRead(UB)))
{
  c = 1;
  WAV = WAV + 1;
  if (WAV == 4) {
    WAV = 1;
  }
}
if ((!digitalRead(DB)))
{
  c = 1;
  WAV = WAV - 1;
  if (WAV == 0) {
    WAV = 3;
  }
}
if ((!digitalRead(LB)))
{
  FREselect();
}
if ((!digitalRead(RB)))
{
  AMPselect();
```

```
   }
   if ((!digitalRead(EB)))
   {
    CheckTemp();
   }
   if ((!digitalRead(SPB)))
   {
    SetTemp();
   }
  }
}

void CheckTemp()
{
 lcd.clear();
 lcd.print("CONFIRM STABLE");
 lcd.setCursor(0, 1);
 lcd.print("TEMPERATURE");
 delay(3000);
 while (1)
 {
  if (!digitalRead(EB))
  {
   StopPinRemove();
  }
  if (!digitalRead(SPB))
  {
   Parameterselect();
  }
 }
}

void StopPinRemove()
{
 lcd.clear();
 lcd.print("PREPARING FOR");
 lcd.setCursor(0, 1);
 lcd.print("TESTING");
 delay(3000);
 lcd.clear();
 lcd.print("REOMOVE THE");
 lcd.setCursor(0, 1);
 lcd.print("MOTOR STOP PIN");
```

```
 delay(3000);
 while (1)
 {
  if (!digitalRead(STB))
  {
   DriveSetup();
  }
  if (!digitalRead(SPB))
  {
   CheckTemp();
  }
 }
}

void DriveSetup()
{
 lcd.clear();
 lcd.print("SETTING UP");
 lcd.setCursor(0, 1);
 lcd.print("MOTOR DRIVER");
 delay(3000);

 switch (WAV)
 {
  case 1:
   NS = (int)(AMP * 10 / Sres); // To keep it using int Sres is 125 not 12.5
   DT = (int)(((1000000 / (4 * FRE)) / NS) - 2.6); //-2.6 to compensate for the 2.6 Delay of digital
write
    delay(280);
    TRIdrive();
    break;
  case 2:
   NS = (int)(AMP * 10 / Sres);
   T[0] = 0;
   for (int c = 1; c <= NS; c++)
   {
    float i = c;
    float TNS = NS;
    T[c] = (acos(1 - 2 * i / TNS) / (2 * pi * FRE)) * 1000000; //o get it into micro seconds
    SDT[c - 1] = T[c] - T[c - 1] - 5.2; // -2.6 to compensate for the 2.6 Delay of digital write, /2 to
allow for up and down
   }
   delay(280);
```

```
    SINdrive();
    break;
   case 3:
    NS = (int)(AMP * 10 / Sres);
    DTM = 50;//min valve for acceptable overshoot 6.3 max on 6mm setting
    DTR = (int)((1000 / (2 * FRE)) - (((DTM + 2.6) * 2) * NS));
    delay(280);
    SQRdrive();
    break;
  }
}

void TRIdrive()
{
 lcd.clear();
 lcd.print("MOTOR IN");
 lcd.setCursor(0, 1);
 lcd.print("OPPERATION");
 for (int i = 0; i < 4; i++)
 {
  digitalWrite(DP, HIGH);
  for (int c = 0; c < NS; c++)
  {
   digitalWrite(SP, HIGH);
   delayMicroseconds(DT);
   digitalWrite(SP, LOW);
   delayMicroseconds(DT);
  }
  digitalWrite(DP, LOW);
  for (int c = 0; c < NS; c++) // repeat in opposite direction
  {
   digitalWrite(SP, HIGH);
   delayMicroseconds(DT);
   digitalWrite(SP, LOW);
   delayMicroseconds(DT);
  }
 }

 StopPinInsert();
}

void SINdrive() {
 lcd.clear();
```

```
 lcd.print("MOTOR IN");
 lcd.setCursor(0, 1);
 lcd.print("OPPERATION");

 for (int i = 0; i < 18000; i++)
 {
  digitalWrite(DP, HIGH);
  for (int c = 0; c < NS; c++)
  {
   delayMicroseconds(SDT[c]);
   digitalWrite(SP, HIGH);
   digitalWrite(SP, LOW);
  }
  digitalWrite(DP, LOW);
  for (int c = 0; c < NS; c++) // repeat in oppersite direction
  {
   delayMicroseconds(SDT[c]);
   digitalWrite(SP, HIGH);
   digitalWrite(SP, LOW);
  }
 }
 StopPinInsert();
}

void SQRdrive() {
 lcd.clear();
 lcd.print("MOTOR IN");
 lcd.setCursor(0, 1);
 lcd.print("OPPERATION");

 DT = 382;
 NS = 866;
 digitalWrite(DP, HIGH);
 for (int c = 0; c < NS; c++)
 {
  digitalWrite(SP, HIGH);
  delayMicroseconds(DT);
  digitalWrite(SP, LOW);
  delayMicroseconds(DT);
 }


  //square waveform
```

```
  for (int i = 0; i < 4; i++)
  {
  digitalWrite(DP, HIGH);
  for (int c = 0; c < NS; c++)
  {
   digitalWrite(SP, HIGH);
   delayMicroseconds(DTM);//max speed
   digitalWrite(SP, LOW);
   delayMicroseconds(DTM);
  }
  delay(75);//time spent at restat the top
  delayMicroseconds(172);
  digitalWrite(DP, LOW);
  for (int c = 0; c < NS; c++) // repeat in opposite direction
  {
   digitalWrite(SP, HIGH);
   delayMicroseconds(DTM);
   digitalWrite(SP, LOW);
   delayMicroseconds(DTM);
  }
  delay(75);//time spent at restat the top
  delayMicroseconds(172);

 //Custom wave

  for (int i = 0; i < 4; i++)
  {
   digitalWrite(DP, HIGH);
   for (int c = 0; c < 311; c++)//1
   {
    digitalWrite(SP, HIGH);
    delayMicroseconds(198);//max speed
    digitalWrite(SP, LOW);
    delayMicroseconds(198);
   }
   digitalWrite(DP, HIGH);
   for (int c = 0; c < 69; c++) //2
   {
    digitalWrite(SP, HIGH);
    delayMicroseconds(903);
    digitalWrite(SP, LOW);
    delayMicroseconds(903);
   }
```

```
digitalWrite(DP, HIGH);
for (int c = 0; c < 52; c++)//3
{
 digitalWrite(SP, HIGH);
 delayMicroseconds(1199);//max speed
 digitalWrite(SP, LOW);
 delayMicroseconds(1199);
}
digitalWrite(DP, LOW);
for (int c = 0; c < 278; c++) //4
{
 digitalWrite(SP, HIGH);
 delayMicroseconds(222);
 digitalWrite(SP, LOW);
 delayMicroseconds(222);
}
digitalWrite(DP, LOW);
for (int c = 0; c < 140; c++)//5
{
 digitalWrite(SP, HIGH);
 delayMicroseconds(444);//max speed
 digitalWrite(SP, LOW);
 delayMicroseconds(444);
}
digitalWrite(DP, HIGH);
for (int c = 0; c < 69; c++) //6
{
 digitalWrite(SP, HIGH);
 delayMicroseconds(903);
 digitalWrite(SP, LOW);
 delayMicroseconds(903);
}
digitalWrite(DP, HIGH);
for (int c = 0; c < 52; c++)//7
{
 digitalWrite(SP, HIGH);
 delayMicroseconds(1199);//max speed
 digitalWrite(SP, LOW);
 delayMicroseconds(1199);
}
digitalWrite(DP, LOW);
for (int c = 0; c < 135; c++) //8
{
```

```
      digitalWrite(SP, HIGH);
      delayMicroseconds(460);
      digitalWrite(SP, LOW);
      delayMicroseconds(460);
    }
   }

  StopPinInsert();
}
```

Arduino 2 (Recording)

```
// libaries to be included
#include <LiquidCrystal.h>
#include <SPI.h>
#include <SD.h>

//Set up LCD screen
LiquidCrystal lcd(31, 33, 29, 27, 25, 23);

//GUI push buttons
const int EB = 49;
const int UB = 51;
const int DB = 47;
const int LB = 53;
const int RB = 45;
const int SPB = 39;
const int PB = 41;
const int STB = 43;

//Shared Error pin
//const int EP = 28;

//Decoder logic read
const int Decoder[] = {52, 40, 42, 44, 46, 48, 50, 38};

//Decoder control
const int EO = 34;
const int DReset = 32;
const int DSel = 36;

//SD card control
const int CS = 4;

//Load cell identifiers
const int LC_Select[] = {13, 12, 11, 10, 9, 8, 7, 6, 5, 3, 2, 22};

//Loadcell analog read pins need to chack pin allocation
const int LC[] = {A0, A1, A2, A3, A4, A5, A6, A7, A8, A9, A10, A11};

//load cell values initialise
int LC_Offset[11]; //only 11 because there is one reference
```

```
int LC_Ave[11];
int LC_Ref = 0;
float LC_Force = 0;
int LCval[500][2];

//Decoded Position
bool PosB[8];
int Pos[500];

//Timers
double T0mic = 0;
double T0mil = 0;
double Tmil = 0;
double Tmic[500];

//global variables
int AMP = 3000;    //default 3mm, 0.1 increments
int FRE = 10;   // frequency default 10Hz, 1Hz increments
int WAV = 1;     // waveform 1-Triangular 2-Sinusoidal 3-Square
float M = 0.008;

int Sres = 254; //use factor 10 res to keep within ints

int NumCycles = 0;

void setup() {
  Serial.begin(9600);
  lcd.begin(16, 2);
  lcd.clear();
  lcd.print("INITIALISING");
  lcd.setCursor(0, 1);
  lcd.print("PROCESSOR 2");
  delay(3000);

  //Push buttons
  pinMode(STB, INPUT_PULLUP);
  pinMode(SPB, INPUT_PULLUP);
  pinMode(PB, INPUT_PULLUP);
  pinMode(RB, INPUT_PULLUP);
  pinMode(UB, INPUT_PULLUP);
  pinMode(EB, INPUT_PULLUP);
  pinMode(DB, INPUT_PULLUP);
  pinMode(LB, INPUT_PULLUP);
```

```
 //Error pin
 pinMode(EP, INPUT);

 //decoder data explicitly disabling internal pull ups
 for (int i = 0; i < 8 ; i++)
 {
  pinMode(Decoder[i], INPUT);
 }

 pinMode(EO, OUTPUT);
 pinMode(DReset, OUTPUT);
 pinMode(DSel, OUTPUT);
 digitalWrite(EO, HIGH);
 digitalWrite(DReset, HIGH);
 digitalWrite(DSel, HIGH);

 //load cell identifiers switches
 for (int i = 0; i < 12 ; i++) {
  pinMode(LC_Select[i], INPUT_PULLUP);
 }

 //load cell readpins left as inputs Zero them on start up.
 //LCref is the average of 20 samples
 for (int i = 0; i < 20; i++)
 {
  LC_Ref = LC_Ref + analogRead(LC[11]); //sum of 20 measurements
  delay(10);
 }
 LC_Ref = int(LC_Ref / 20); // average of the 20 measurements

 for (int i = 0; i < 11; i++)
 {
  for (int c = 0; c < 20; c++)
  {
   LC_Ave[i] = LC_Ave[i] + analogRead(LC[i]); //sum of 20 measurements
   delay(10);
  }
  LC_Ave[i] = int(LC_Ave[i] / 20); // average of the 20 measurements
  LC_Offset[i] = LC_Ave[i] - LC_Ref;
 }

Serial.print(LC_Ref);
```

```
  if (!SD.begin(CS)) {
    lcd.clear();
    lcd.print("SC CARD FAILED");
    lcd.setCursor(0, 1);
    lcd.print("NOT PRESENT");
    // don't do anything more:
    return;
  }
}

void loop()
{
  StopPinInsert();
}

//Prompt instruction on LCD
void StopPinInsert()
{
  lcd.clear();
  lcd.print("PRESS ENTER");
  lcd.setCursor(0, 1);
  lcd.print("TO CONFIRM");
  delay(3000);
  while (1)
  {
    if (!digitalRead(EB))
    {
      LoadSamples();
    }
  }
}

//Prompt instruction on LCD
void LoadSamples()
{
  lcd.clear();
  lcd.print("PRESS ENTER");
  lcd.setCursor(0, 1);
  lcd.print("ONCE LOADED");
  delay(3000);
  while (1)
  {
    if (!digitalRead(EB))
```

```
   {
    MeasureSamples();
   }
  }
}

//Prompt instruction on LCD and measure each load cells current load
void MeasureSamples()
{
 lcd.clear();
 lcd.print("TO VIEW");
 lcd.setCursor(0, 1);
 lcd.print("PRE-TENSION");
 delay(3000);
 lcd.clear();
 lcd.print("LOAD CELL FORCE");
 lcd.setCursor(0, 1);
 lcd.print("(SELECT)");
 int i = 0;
 while (i < 11)
 {
  LC_Ref = 0;
  for (int i = 0; i < 20; i++)
  {
   LC_Ref = LC_Ref + analogRead(LC[11]); //sum of 20 measurements
   delay(10);
  }
  LC_Ref = int(LC_Ref / 20);

  if (!digitalRead(LC_Select[i]))
  {
   LC_Force = (analogRead(LC[i]) - LC_Ref - LC_Offset[i]) * M;
   lcd.setCursor(0, 1);
   lcd.print("               ");
   lcd.setCursor(0, 1);
   lcd.print("LC " + String((i + 1), 0) + " = " + String(LC_Force, 3) + "N"); // defining the precision
of the flaot to that od 3 decimal points?
   delay(100); //adjust according to preference of refresh rate
   i = 0;
  }
  if (!digitalRead(EB))
  {
   SetTemp();
```

```
    }
    if (!digitalRead(SPB))
    {
     LoadSamples();
    }

    i = i + 1;
    if (i > 10)
    {
     i = 0;
    }
  }
}

void SetTemp()
{
  lcd.clear();
  lcd.print("UP TO THE");
  lcd.setCursor(0, 1);
  lcd.print("DEMARCATED LINE");
  delay(3000);
  lcd.clear();
  lcd.print("PRESS ENTER");
  lcd.setCursor(0, 1);
  lcd.print("ONCE SET");
  while (1)
  {
    if (!digitalRead(EB))
    {
     Parameterselect();
    }
    if (!digitalRead(SPB))
    {
     MeasureSamples();
    }
  }
}
void Parameterselect()
{ //PARAMETER SELECT INSTRUCTIONS
  lcd.clear();
  lcd.print("USING LEFT AND");
  lcd.setCursor(0, 1);
  lcd.print("RIGHT BUTTONS");
```

```
 delay(3000);
 lcd.clear();
 lcd.print("USING THE UP");
 lcd.setCursor(0, 1);
 lcd.print("AND DOWN BUTTONS");
 delay(3000);
 lcd.clear();
 lcd.print("USING THE");
 lcd.setCursor(0, 1);
 lcd.print("ENTER BUTTON");
 delay(3000);

 AMPselect();

}

void AMPselect() { // add selection limits
 bool c = 1;
 while (1) {
  if (c)
  {
   c = 0;
   lcd.clear();
   lcd.print("AMPLITUDE");
   lcd.setCursor(0, 1);
   lcd.print(String(AMP) + " um");
   delay(500);
  }
  if ((!digitalRead(UB)))
  {
   c = 1;
   AMP = AMP + 100;
   if (AMP > 6000) {
    AMP = 6000;
    lcd.clear();
    lcd.print("ERROR: MAXIMUM OF");
    lcd.setCursor(0, 1);
    lcd.print("6000 um");
    delay(3000);
   }
  }
  if ((!digitalRead(DB)))
  {
```

```
    c = 1;
    AMP = AMP - 100;
    if (AMP == 900) { //set minimum amplitude to 1mm (compatible with microsecond delay)
     AMP = 1000;
     lcd.clear();
     lcd.print("ERROR: MINIMUM OF");
     lcd.setCursor(0, 1);
     lcd.print("1000 um");
     delay(3000);
    }
   }
   if ((!digitalRead(LB)))
   {
    WAVselect();
   }
   if ((!digitalRead(RB)))
   {
    FREselect();
   }
   if ((!digitalRead(EB)))
   {
    CheckTemp();
   }
   if ((!digitalRead(SPB)))
   {
    SetTemp();
   }
  }
}
void FREselect() { // add selection limits
 bool c = 1;
 while (1) {
  if (c)
  {
   c = 0;
   lcd.clear();
   lcd.print("FREQUENCY");
   lcd.setCursor(0, 1);
   lcd.print(String(FRE) + " Hz");
   delay(500);
  }
  if ((!digitalRead(UB)))
  {
```

```
    c = 1;
    FRE = FRE + 1;
    if (FRE > 20) {
     FRE = 20;
     lcd.clear();
     lcd.print("ERROR: MAXIMUM OF");
     lcd.setCursor(0, 1);
     lcd.print("20 Hz");
     delay(3000);
    }
   }
   if ((!digitalRead(DB)))
   {
    c = 1;
    FRE = FRE - 1;
    if (FRE == 0) {
     FRE = 1;
     lcd.clear();
     lcd.print("ERROR: MINIMUM OF");
     lcd.setCursor(0, 1);
     lcd.print("1 Hz");
     delay(3000);
    }
   }
   if ((!digitalRead(LB)))
   {
    AMPselect();
   }
   if ((!digitalRead(RB)))
   {
    WAVselect();
   }
   if ((!digitalRead(EB)))
   {
    CheckTemp();
   }
   if ((!digitalRead(SPB)))
   {
    SetTemp();
   }
  }
}
```

```
void WAVselect() { // add selection limits
 bool c = 1;
 while (1) {
  if (c)
  {
   c = 0;
   switch (WAV) {
    case 1:
     lcd.clear();
     lcd.print("WAVEFORM");
     lcd.setCursor(0, 1);
     lcd.print("TRIANGULAR");
     break;
    case 2:
     lcd.clear();
     lcd.print("WAVEFORM");
     lcd.setCursor(0, 1);
     lcd.print("SINUSOIDAL");
     break;
    case 3:
     lcd.clear();
     lcd.print("WAVEFORM");
     lcd.setCursor(0, 1);
     lcd.print("SQUARE");
     break;
   }
   delay(500);
  }
  if ((!digitalRead(UB)))
  {
   c = 1;
   WAV = WAV + 1;
   if (WAV == 4) {
    WAV = 1;
   }
  }
  if ((!digitalRead(DB)))
  {
   c = 1;
   WAV = WAV - 1;
   if (WAV == 0) {
    WAV = 3;
   }
```

```
   }
   if ((!digitalRead(LB)))
   {
    FREselect();
   }
   if ((!digitalRead(RB)))
   {
    AMPselect();
   }
   if ((!digitalRead(EB)))
   {
    CheckTemp();
   }
   if ((!digitalRead(SPB)))
   {
    SetTemp();
   }
  }
}

void CheckTemp()
{
 lcd.clear();
 lcd.print("BY PRESSING THE");
 lcd.setCursor(0, 1);
 lcd.print("ENTER BUTTON");
 delay(3000);
 while (1)
 {
  if (!digitalRead(EB))
  {
   StopPinRemove();
  }
  if (!digitalRead(SPB))
  {
   Parameterselect();
  }
 }
}

void StopPinRemove()
{
 //zero the decoder position register now
```

```
 lcd.clear();
 lcd.print("PREPARING FOR");
 lcd.setCursor(0, 1);
 lcd.print("TESTING");
 digitalWrite(DReset, LOW);//zero the decoder position register now
 delay(500);
 digitalWrite(DReset, HIGH);
 delay(500);
 lcd.clear();
 lcd.print("PRESS START TO");
 lcd.setCursor(0, 1);
 lcd.print("BEGIN TESTING");
 delay(3000);
 while (1)
 {
  if (!digitalRead(STB))
  {
   FileSetup();
  }
  if (!digitalRead(SPB))
  {
   CheckTemp();
  }
 }
}

void FileSetup()
{
 lcd.clear();
 lcd.print("SETTING UP");
 lcd.setCursor(0, 1);
 lcd.print("DATA STORAGE");
 delay(3000);
 File dataFile = SD.open("Test1.txt", FILE_WRITE);
 if (dataFile)
 {
  dataFile.println("Amplitude:");
  dataFile.println(String(AMP));
  dataFile.println("Frequency:");
  dataFile.println(String(FRE));
  dataFile.println("Waveform:");
  dataFile.println(String(WAV));
  dataFile.println("LC No., Time(uS), Position(um), Load(N)");
```

```
  dataFile.close();
 }
 else
 {
  lcd.clear();
  lcd.print("ERROR, SD CARD");
  lcd.setCursor(0, 1);
  lcd.print("NOT FUNCTIONING");
 }
 T0mil = millis();

 RecordingMode();
}

void RecordingMode()
{
 lcd.clear();
 lcd.print("RECORDING DATA");

 Tmil = millis() - T0mil;
 T0mic = micros();
 LC_Ref = 0;

 for (int i = 0; i < 20; i++)
 {
//   LC_Ref = LC_Ref + analogRead(LC[11]); //sum of 20 measurements
  delay(10);
 }
 LC_Ref = int(LC_Ref / 20); // average of the 20 measurements

 for (int i = 0; i < 500; i++)
 {
  digitalWrite(EO, HIGH);
  delayMicroseconds(31);//min required
  Tmic[i] = micros() - T0mic;
  digitalWrite(EO, LOW);
  /*
  for (int c = 0; c < 11 ; c++)
  {
   LCval[i][c] = analogRead(LC[c]);
  }
  */
```

```
   for (int z = 0; z < 8 ; z++)
   {
    PosB[z] = digitalRead(Decoder[z]);
   }
   for (int z = 0; z < 8; z++)
   {
    Pos[i] |= PosB[z] << z;
   }
  }
  WritingData();
}

void WritingData()
{
  lcd.clear();
  lcd.print("SAVING DATA");

  File dataFile = SD.open("Test1.txt", FILE_WRITE); //very slow but everything is already
recorded
  for (int i = 0; i < 500; i++)
  {
   dataFile.println(String(Tmil * 1000 + Tmic[i], 0) + "," + String(Pos[i] * 6.35 , 1) + "," +
String((LCval[i][0] - LC_Ref - LC_Offset[0])*M, 3) + "," + String((LCval[i][1] - LC_Ref -
LC_Offset[1])*M, 3) + "," + String((LCval[i][2] - LC_Ref - LC_Offset[2])*M, 3) + "," +
String((LCval[i][3] - LC_Ref - LC_Offset[3])*M, 3) + "," + String((LCval[i][4] - LC_Ref -
LC_Offset[4])*M, 3) + "," + String((LCval[i][5] - LC_Ref - LC_Offset[5])*M, 3) + "," +
String((LCval[i][6] - LC_Ref - LC_Offset[6])*M, 3) + "," + String((LCval[i][7] - LC_Ref -
LC_Offset[7])*M, 3) + "," + String((LCval[i][8] - LC_Ref - LC_Offset[8])*M, 3) + "," +
String((LCval[i][9] - LC_Ref - LC_Offset[9])*M, 3) + "," + String((LCval[i][10] - LC_Ref -
LC_Offset[10])*M, 3));
  }
  dataFile.close();

 // NumCycles = int(Time[499] * FRE / 1000000);
//  lcd.clear();
//  lcd.print("NUMBER OF CYCLES");
//  lcd.setCursor(0, 1);
//  lcd.print(String(NumCycles));
  for (int i = 0; i < 3000; i++) //wait for 5min
  {
   if (!digitalRead(PB))
   {
```

```
    while (1)
    {
     if (!digitalRead(STB))
     {
      RecordingMode();
     }
     if (!digitalRead(SPB))
     {
      StopPinInsert();
     }
    }
   }
   if (!digitalRead(SPB))
   {
    StopPinInsert();
   }
   /*
   if (!digitalRead(EP))// MOTOR WOULD FREEWHEEL
   {
    lcd.clear();
    lcd.print("USING THE STOP");
    lcd.setCursor(0, 1);
    lcd.print("BUTTON");
    while (1)
    {
     if (!digitalRead(SPB))
     {
      StopPinInsert();
     }
    }
   }
  */
   delay(100);
 }
 RecordingMode();
}
```

Appendix B

Model Simulations Code

Equilibrium Model with Static N

```
clear;
//chain density component
u = 1.55;
//initial number of monomers between crosslinks
N0 =34;
//soft segment decomposition factor
A =20;
//Initial soft segment volumetric fraction
Vs0 = 0.333;
////Saturation soft segment volumetric fraction
Vss = 1;
c = 1;

//strain to 600%
while c < 601
Vs(1)=Vs0;
N(c)=N0;
//Stretch
ST(c) = 1+(c-1)/100;
//Strain
Strain(c) = (c-1)/100;
//Chain lockout length
STlock(c) = sqrt(N(c));
//Amplification Factor
X(c) = 1+3.5*(1-Vs(c))+18*((1-Vs(c))^2);
//Chain stretch
chain(c) = sqrt((1/3)*((ST(c)^2)+(2/ST(c))));
//Amplified chain stretch
Achain(c) = 1+X(c)*(chain(c)-1);
//Inverse Langevin approximation
x = (Achain(c)/sqrt(N(c)));
ILang(c) =
x*(3-1.00651*(x^2)-0.962251*(x^4)+1.47353*(x^6)-0.48953*(x^8))/((1-x)*(1+1.01524*x));
//Stress function, from strain energy function
Stress(c) = (Vs(c))*(X(c))*((u)/3)*(sqrt(N(c))/Achain(c))*ILang(c)*((ST(c))^2-(ST(c)^-1));
```

```
//Evolution of Soft segment, as prescribed boyce
Vs(c+1)=Vss-(Vss-Vs0)*exp((-A)*(Achain(c)-1)/(STlock(c)-Achain(c)));
c = c+1;
end

scf(1);
plot(Strain,Stress)
```

Equilibrium Model with Evolving N

```
clear;
//chain density component
u = 1.55;
//initial number of monomers between crosslinks
N0 =24;
//saturation number of monomers between crosslinks
NS = 44;
//soft segment decomposition factor
A =20;
//Initial soft segment volumetric fraction
Vs0 = 0.333;
////Saturation soft segment volumetric fraction
Vss = 1;
c = 1;

//strain to 600%
while c < 601
Vs(1)=Vs0;
N(1)=N0;
//Stretch
ST(c) = 1+(c-1)/100;
//Strain
Strain(c) = (c-1)/100;
//Chain lockout length
STlock(c) = sqrt(N(c));
//Amplification Factor
X(c) = 1+3.5*(1-Vs(c))+18*((1-Vs(c))^2);
//Chain stretch
chain(c) = sqrt((1/3)*((ST(c)^2)+(2/ST(c))));
//Amplified chain stretch
Achain(c) = 1+X(c)*(chain(c)-1);
//Inverse Langevin approximation
x = (Achain(c)/sqrt(N(c)));
ILang(c) =
x*(3-1.00651*(x^2)-0.962251*(x^4)+1.47353*(x^6)-0.48953*(x^8))/((1-x)*(1+1.01524*x));
//Stress function, from strain energy function
Stress(c) = (Vs(c))*(X(c))*((u)/3)*(sqrt(N(c))/Achain(c))*ILang(c)*((ST(c))^2-(ST(c)^-1));
//Evolution of Soft segment, as prescribed boyce
Vs(c+1)=Vss-(Vss-Vs0)*exp((-A)*(Achain(c)-1)/(STlock(c)-Achain(c)));
//Linear Evolution of N
```

```
N(c+1)=(((NS-N0)/(Vss-Vs0))*Vs(c))+(N0-(((NS-N0)/(Vss-Vs0))*Vs0));
c = c+1;
end

scf(1);
plot(Strain,Stress)
```

Loading History Model

```
clear;
//chain density component
u = 1.55;
//initial number of monomers between crosslinks
N0 =24;
//saturation number of monomers between crosslinks
NS = 44;
//soft segment decomposition factor
A =20;
//Initial soft segment volumetric fraction
Vs0 = 0.333;
////Saturation soft segment volumetric fraction
Vss = 1;
c = 1;

//strain to 600%
while c < 601
Vs(1)=Vs0;
N(1)=N0;
//Stretch
ST(c) = 1+(c-1)/100;
//Strain
Strain(c) = (c-1)/100;
//Chain lockout length
STlock(c) = sqrt(N(c));
//Amplification Factor
X(c) = 1+3.5*(1-Vs(c))+18*((1-Vs(c))^2);
//Chain stretch
chain(c) = sqrt((1/3)*((ST(c)^2)+(2/ST(c))));
//Amplified chain stretch
Achain(c) = 1+X(c)*(chain(c)-1);
//Inverse Langevin approximation
x = (Achain(c)/sqrt(N(c)));
ILang(c) =
x*(3-1.00651*(x^2)-0.962251*(x^4)+1.47353*(x^6)-0.48953*(x^8))/((1-x)*(1+1.01524*x));
//Stress function, from strain energy function
Stress(c) = (Vs(c))*(X(c))*((u)/3)*(sqrt(N(c))/Achain(c))*ILang(c)*((ST(c))^2-(ST(c)^-1));
//Evolution of Soft segment, as prescribed boyce
Vs(c+1)=Vss-(Vss-Vs0)*exp((-A)*(Achain(c)-1)/(STlock(c)-Achain(c)));
//Linear Evolution of N
```

```
N(c+1)=(((NS-N0)/(Vss-Vs0))*Vs(c))+(N0-(((NS-N0)/(Vss-Vs0))*Vs0));
c = c+1;
end

//find Vs and N at 100, 200 and 300% elongation
disp(Vs(100));
disp(N(100));
disp(Vs(200));
disp(N(200));
disp(Vs(300));
disp(N(300));

scf(1);
plot(Strain,Stress)
```

Viscous Model

```
clear;
//chain density component
u = 1.55;
//initial number of monomers between crosslinks
N0 =24;
//saturation number of monomers between crosslinks
NS = 44;
//Strain rate
SR=0.001;
//minimum number of monomers between crosslinks
Nmin = 20;
//soft segment decomposition factor
A =20;
//Initial soft segment volumetric fraction
Vs0 = 0.333;
////Saturation soft segment volumetric fraction
Vss = 1;
c = 1;

//strain to 600%
while c < 601
Vs(1)=Vs0;
N(1)=N0;
//Rate dependant effective N
N(c) = Nmin+(N(c)-Nmin)/(130*SR+1);
//Stretch
ST(c) = 1+(c-1)/100;
//Strain
Strain(c) = (c-1)/100;
//Chain lockout length
STlock(c) = sqrt(N(c));
//Amplification Factor
X(c) = 1+3.5*(1-Vs(c))+18*((1-Vs(c))^2);
//Chain stretch
chain(c) = sqrt((1/3)*((ST(c)^2)+(2/ST(c))));
//Amplified chain stretch
Achain(c) = 1+X(c)*(chain(c)-1);
//Inverse Langevin approximation
x = (Achain(c)/sqrt(N(c)));
```

```
ILang(c) =
x*(3-1.00651*(x^2)-0.962251*(x^4)+1.47353*(x^6)-0.48953*(x^8))/((1-x)*(1+1.01524*x));
//Stress function, from strain energy function
Stress(c) = (Vs(c))*(X(c))*((u)/3)*(sqrt(N(c))/Achain(c))*ILang(c)*((ST(c))^2-(ST(c)^-1));
//Evolution of Soft segment, as prescribed boyce
Vs(c+1)=Vss-(Vss-Vs0)*exp((-A)*(Achain(c)-1)/(STlock(c)-Achain(c)));
//Linear Evolution of N
N(c+1)=(((NS-N0)/(Vss-Vs0))*Vs(c))+(N0-(((NS-N0)/(Vss-Vs0))*Vs0));
c = c+1;
end

scf(1);
plot(Strain,Stress)
```

Appendix C

Circuit Diagrams and PCB Layout

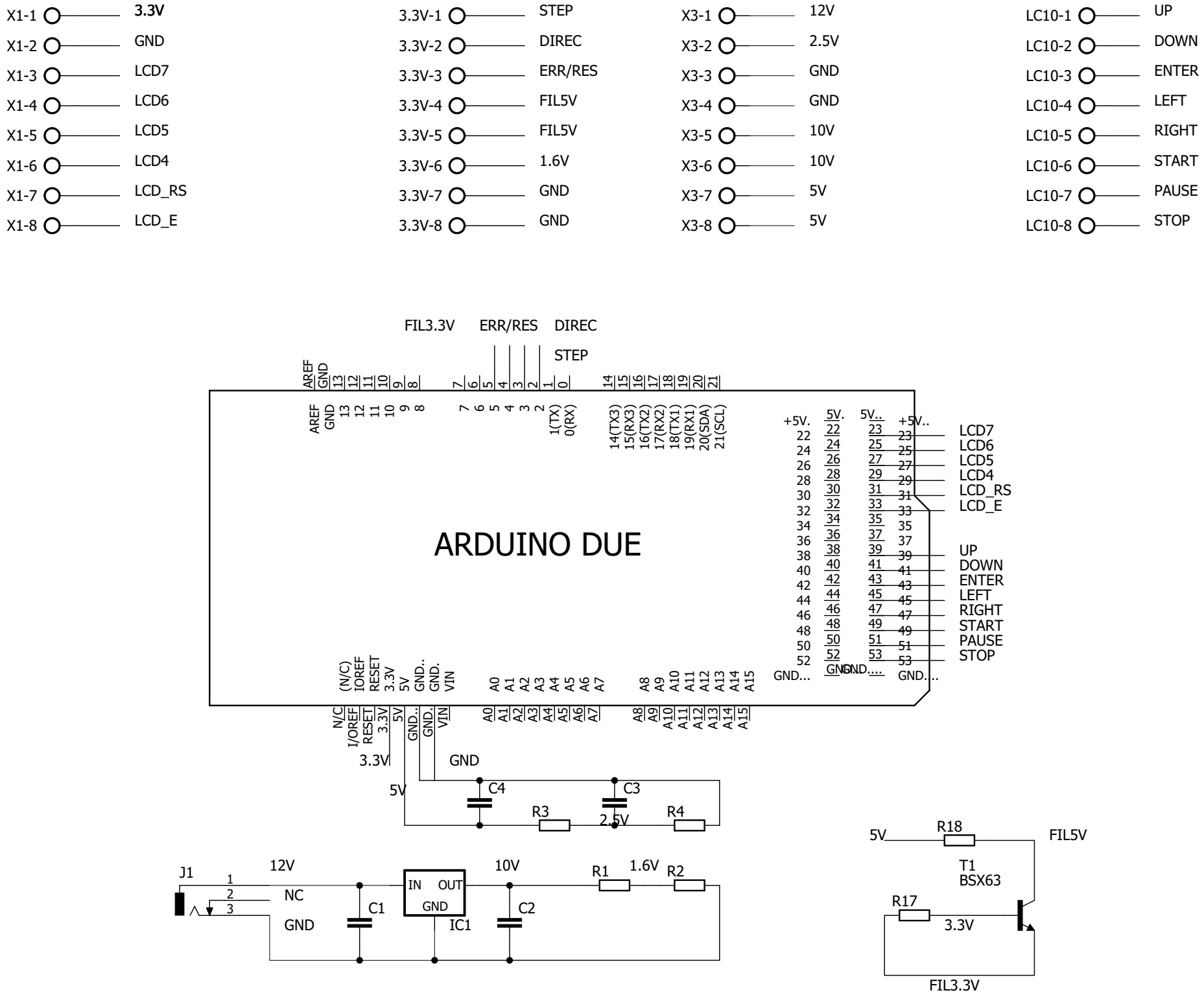

2018-02-28 6:32 PM f=1.20 F:\Power and Drive\Power and drive.sch (Sheet: 1/1)

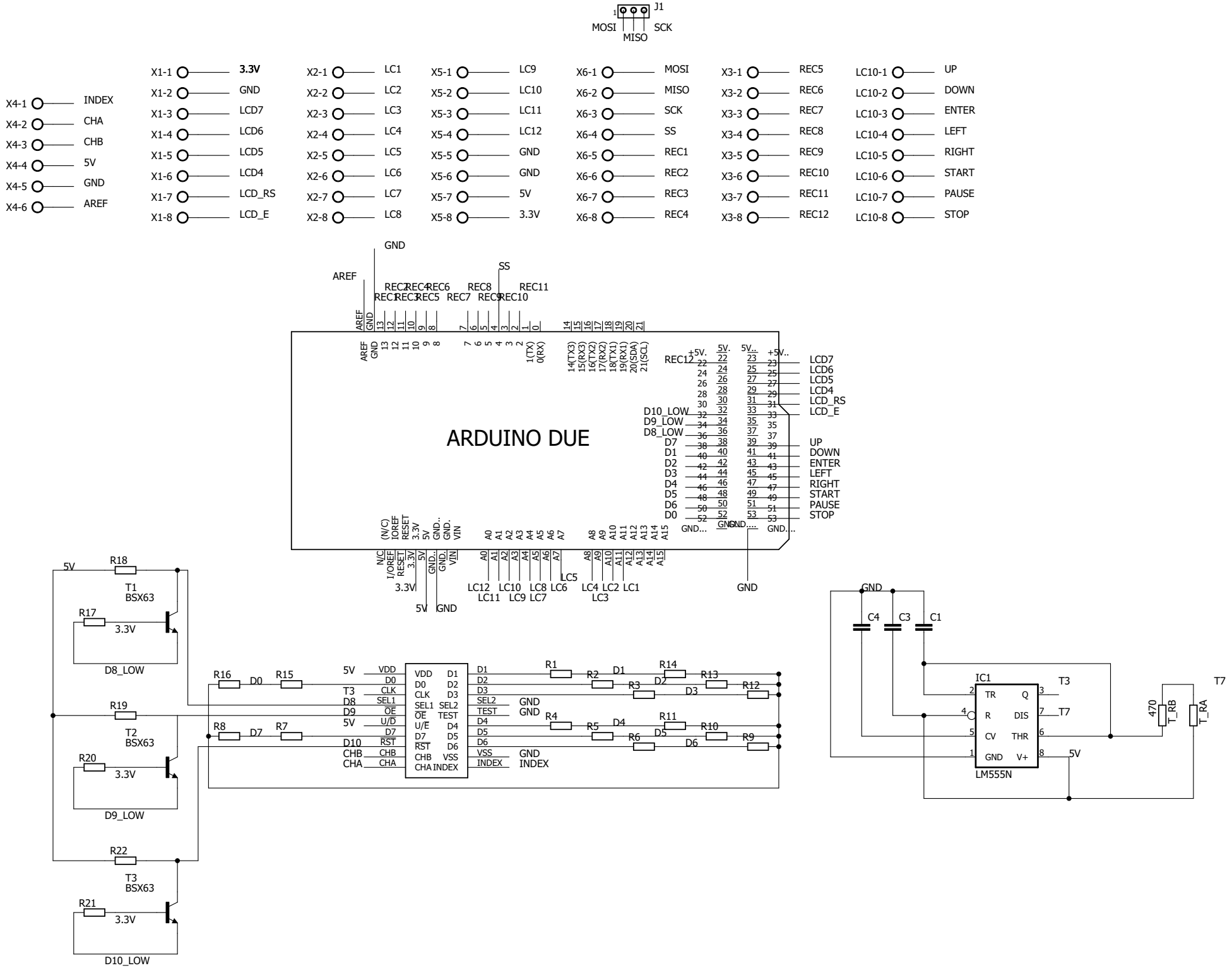

2018-02-28 6:33 PM f=0.86 F:\Recording\Recording.sch (Sheet: 1/1)

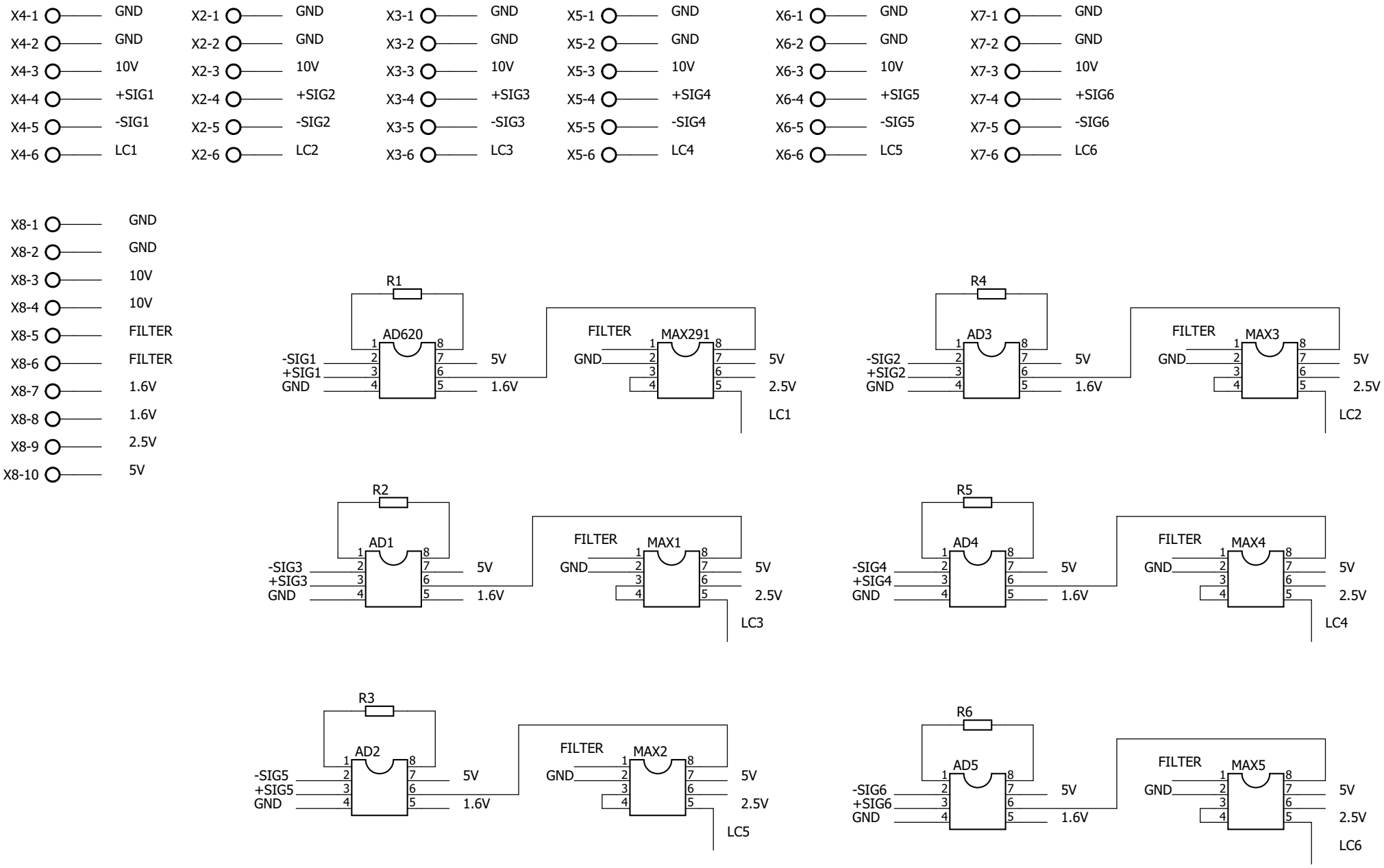
X4-1 GND
X4-2 GND
X4-3 10V
X4-4 +SIG1
X4-5 -SIG1
X4-6 LC1
X2-1 GND
X2-2 GND
X2-3 10V
X2-4 +SIG2
X2-5 -SIG2
X2-6 LC2
X3-1 GND
X3-2 GND
X3-3 10V
X3-4 +SIG3
X3-5 -SIG3
X3-6 LC3
X5-1 GND
X5-2 GND
X5-3 10V
X5-4 +SIG4
X5-5 -SIG4
X5-6 LC4
X6-1 GND
X6-2 GND
X6-3 10V
X6-4 +SIG5
X6-5 -SIG5
X6-6 LC5
X7-1 GND
X7-2 GND
X7-3 10V
X7-4 +SIG6
X7-5 -SIG6
X7-6 LC6
X8-1 GND
X8-2 GND
X8-3 10V
X8-4 10V
X8-5 FILTER
X8-6 FILTER
X8-7 1.6V
X8-8 1.6V
X8-9 2.5V
X8-10 5V
R1
AD620
-SIG1
+SIG1
GND
5V
1.6V
FILTER
MAX291
GND
5V
2.5V
LC1
R4
AD3
-SIG2
+SIG2
GND
5V
1.6V
FILTER
MAX3
GND
5V
2.5V
LC2
R2
AD1
-SIG3
+SIG3
GND
5V
1.6V
FILTER
MAX1
GND
5V
2.5V
LC3
R5
AD4
-SIG4
+SIG4
GND
5V
1.6V
FILTER
MAX4
GND
5V
2.5V
LC4
R3
AD2
-SIG5
+SIG5
GND
5V
1.6V
FILTER
MAX2
GND
5V
2.5V
LC5
R6
AD5
-SIG6
+SIG6
GND
5V
1.6V
FILTER
MAX5
GND
5V
2.5V
LC6

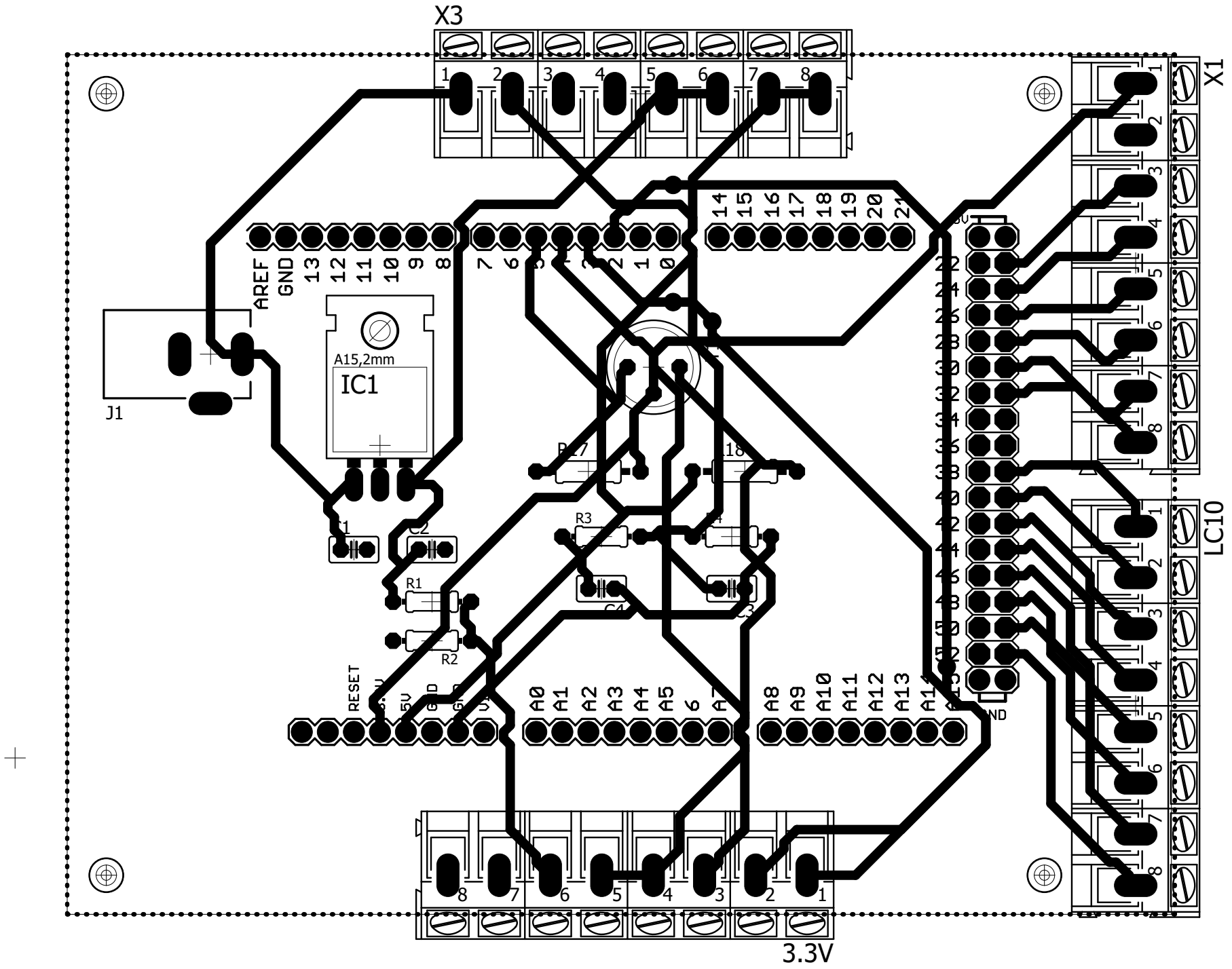
X3
X1
LC10
J1
IC1
A15,2mm
AREF
GND
RESET
3.3V
5V
R1
R2
R3
C1
C2
C3
C4

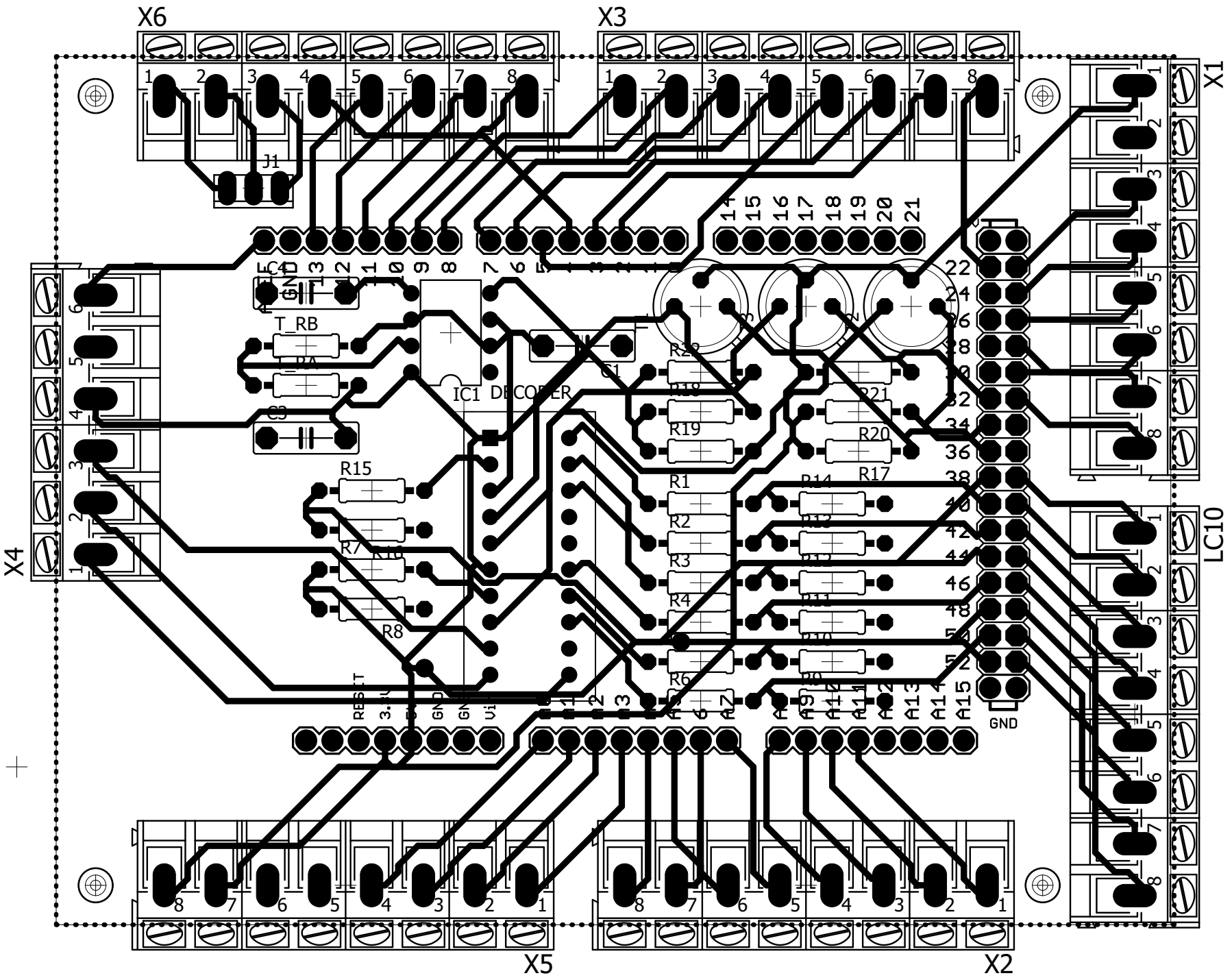
X6
X3
X1
X4
LC10
X5
X2
J1
IC1 DECODER
C1
C3
T_RB
T_DA
R15
R1
R2
R3
R4
R6
R7
R8
R10
R12
R13
R14
R17
R18
R19
R20
R21
GND

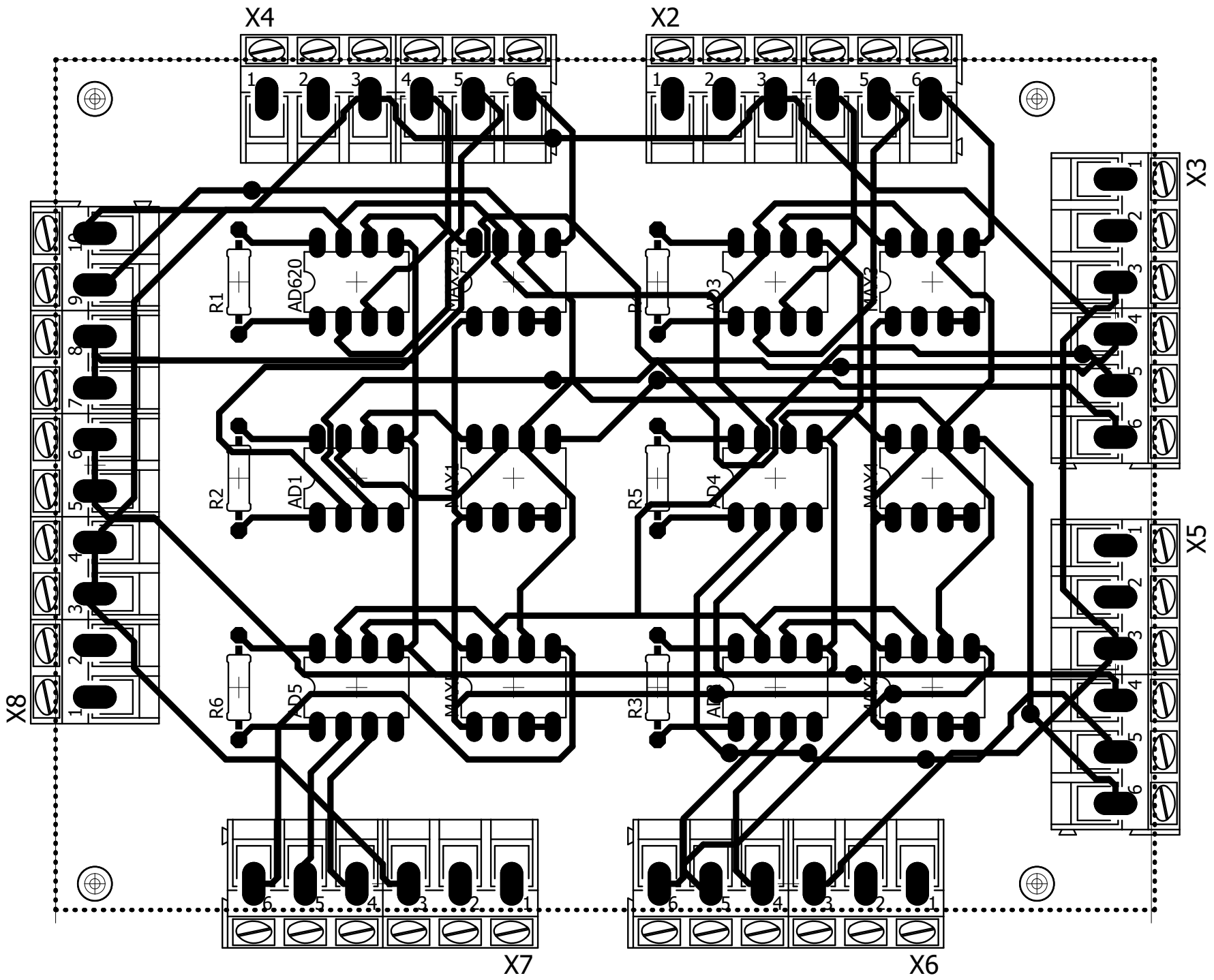
X4
X2
X3
X5
X8
X7
X6
R1
R2
R6
R3
R5
AD620
AD1
AD5
AD3
AD4
MAX2
MAX1
MAX4

Appendix D

Machine Drawings

MATERIAL	ALUMINIUM
QUANTITY	1

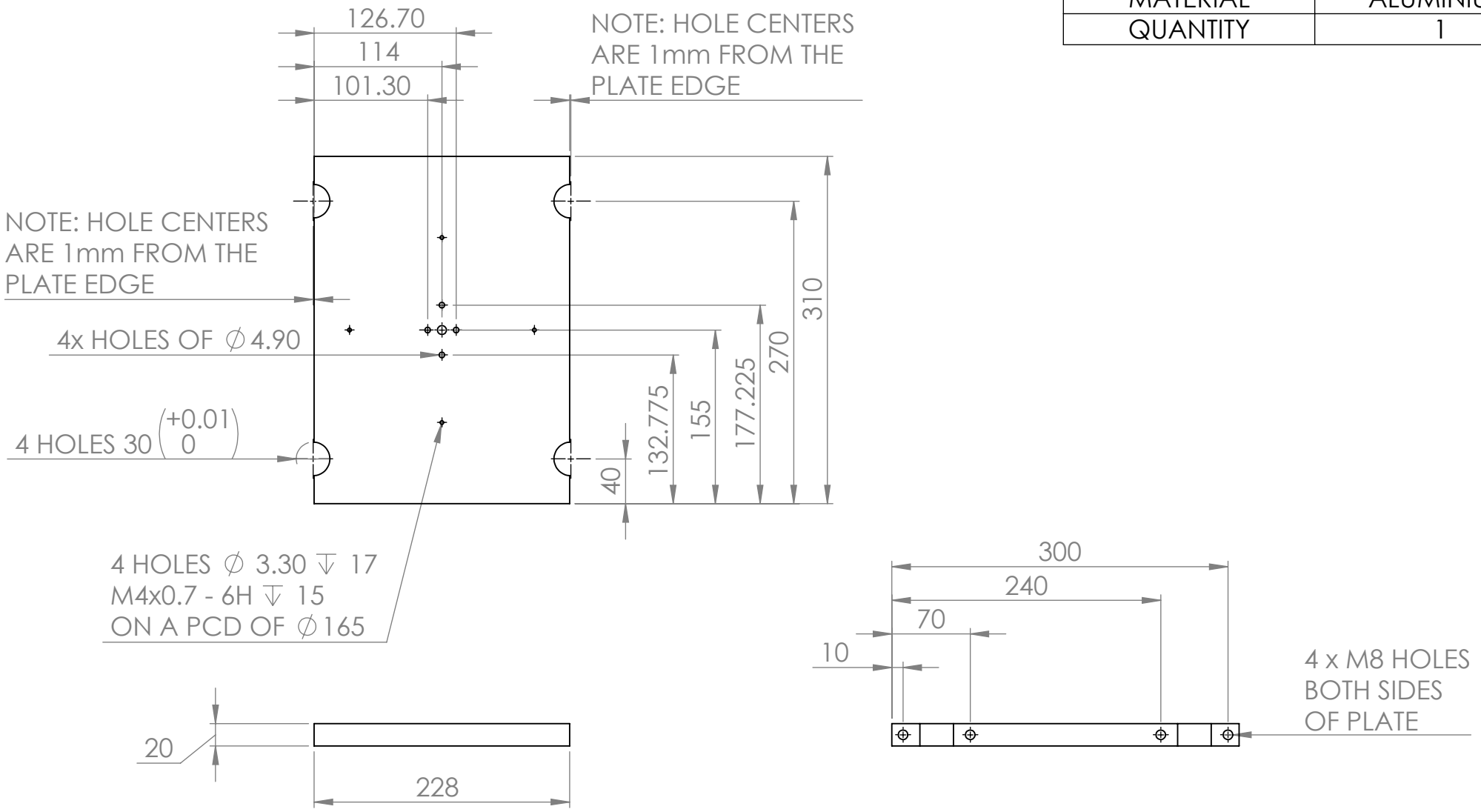

UNLESS OTHERWISE SPECIFIED	
LINEAR TOLERANCE	±0.05
ANGULAR TOLERANCE	±1°

DRAWN BY:	BRADEN VAN BREDA	DATE: 20/07/2015	UNIVERSITY OF CAPE TOWN
CHECKED:			
APPROVED:		REVISION:	P0
TITLE: TOP PLATE		DRAWING NO. FTR - P001	
PROJECTION	SCALE 1:5	ALL DIMENSIONS IN MILLIMETRES	

MATERIAL	ALUMINIUM
QUANTITY	1

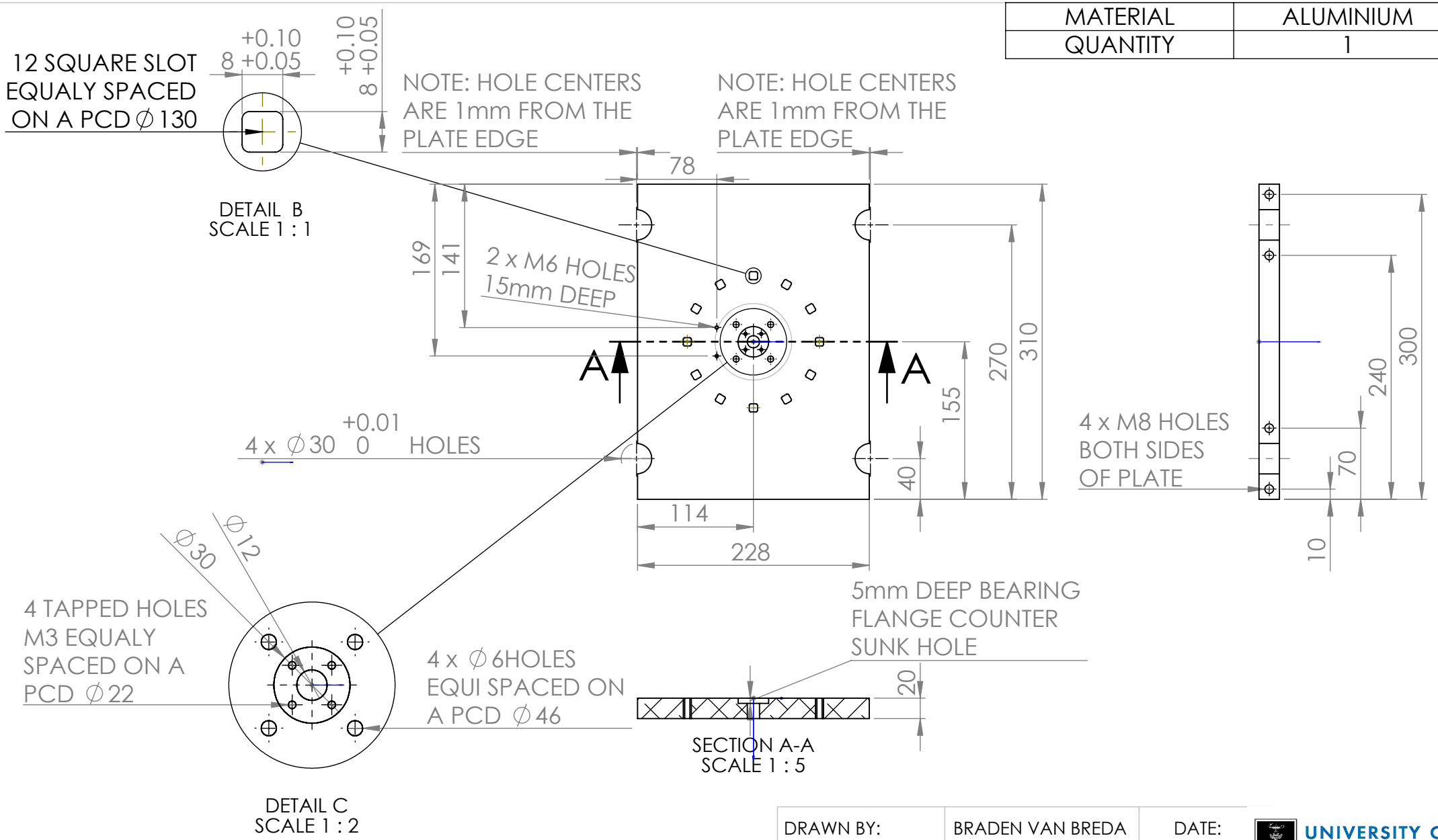

UNLESS OTHERWISE SPECIFIED	
LINEAR TOLERANCE	±0.05
ANGULAR TOLERANCE	±1°

DRAWN BY:	BRADEN VAN BREDA	DATE: 20/07/2015	UNIVERSITY OF CAPE TOWN
CHECKED:			
APPROVED:		REVISION:	P0
TITLE: MIDDLE PLATE		DRAWING NO. FTR - P002	
PROJECTION	SCALE 1:5	ALL DIMENSIONS IN MILLIMETRES	

MATERIAL	STAINLESS STEEL
QUANTITY	1

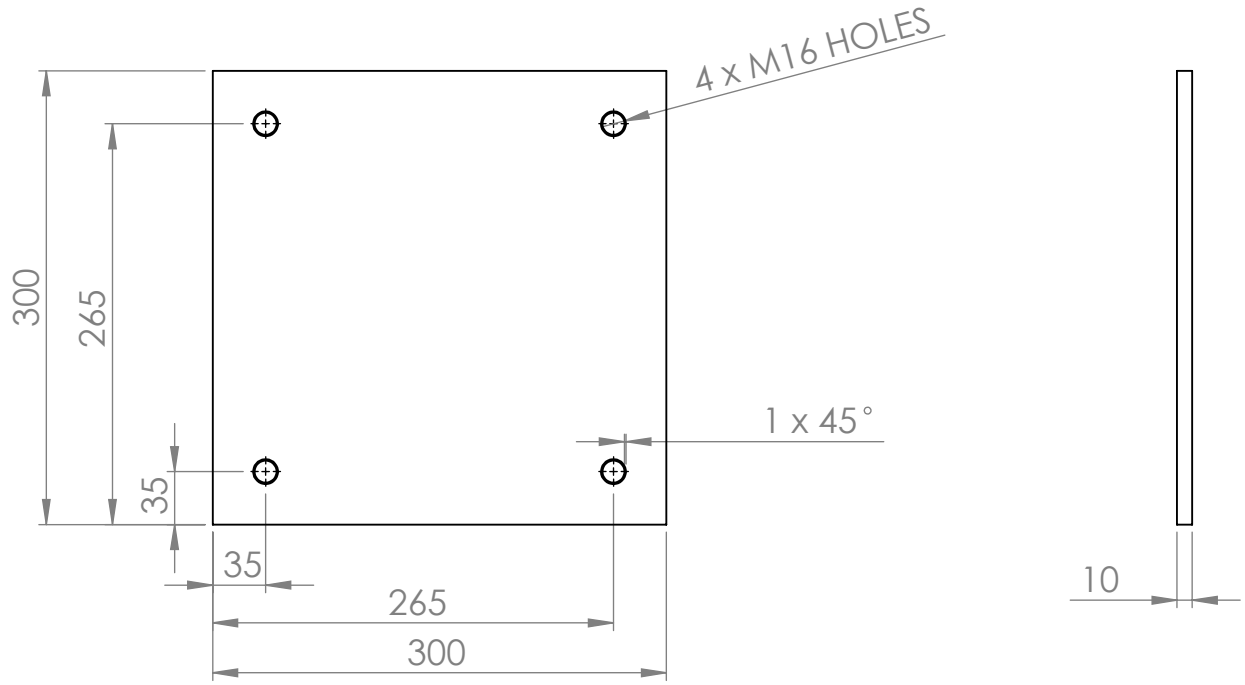

UNLESS OTHERWISE SPECIFIED	
LINEAR TOLERANCE	±0.01
ANGULAR TOLERANCE	±1°

DRAWN BY:	BRADEN VAN BREDA	DATE:	UNIVERSITY OF CAPE TOWN
CHECKED:		20/07/2015	
APPROVED:		REVISION:	P0
TITLE: BOTTOM PLATE		DRAWING NO. FTR - P003	
PROJECTION	SCALE 1:5	ALL DIMENSIONS IN MILLIMETRES	

MATERIAL	STAINLESS STEEL
QUANTITY	4

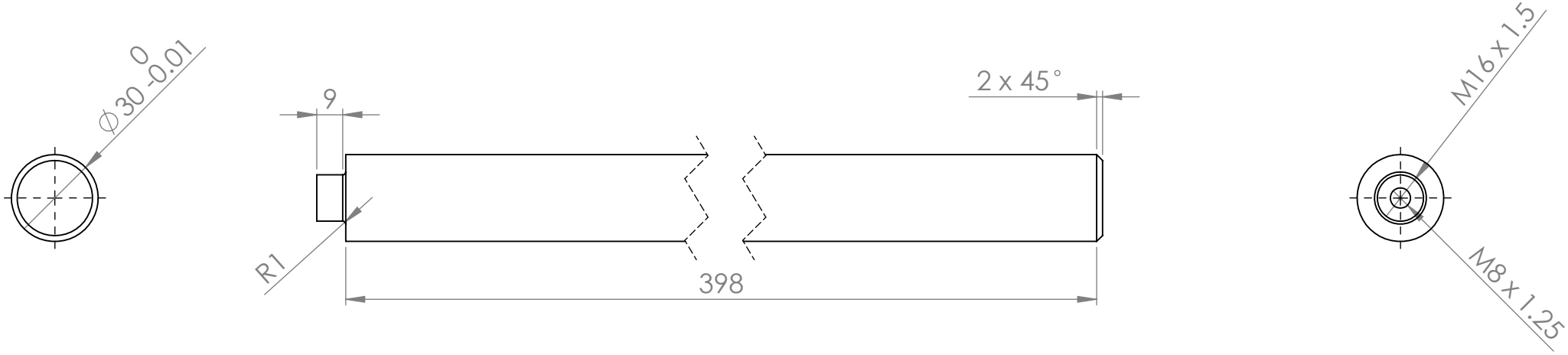

UNLESS OTHERWISE SPECIFIED	
LINEAR TOLERANCE	±0.05
ANGULAR TOLERANCE	±1°

DRAWN BY:	BRADEN VAN BREDA	DATE:	UNIVERSITY OF CAPE TOWN
CHECKED:		20/07/2015	
APPROVED:		REVISION:	P0
TITLE: SUPPORT CYLINDER		DRAWING NO. FTR - P004	
PROJECTION	SCALE 1:2	ALL DIMENSIONS IN MILLIMETRES	

MATERIAL	ALUMINIUM
QUANTITY	1

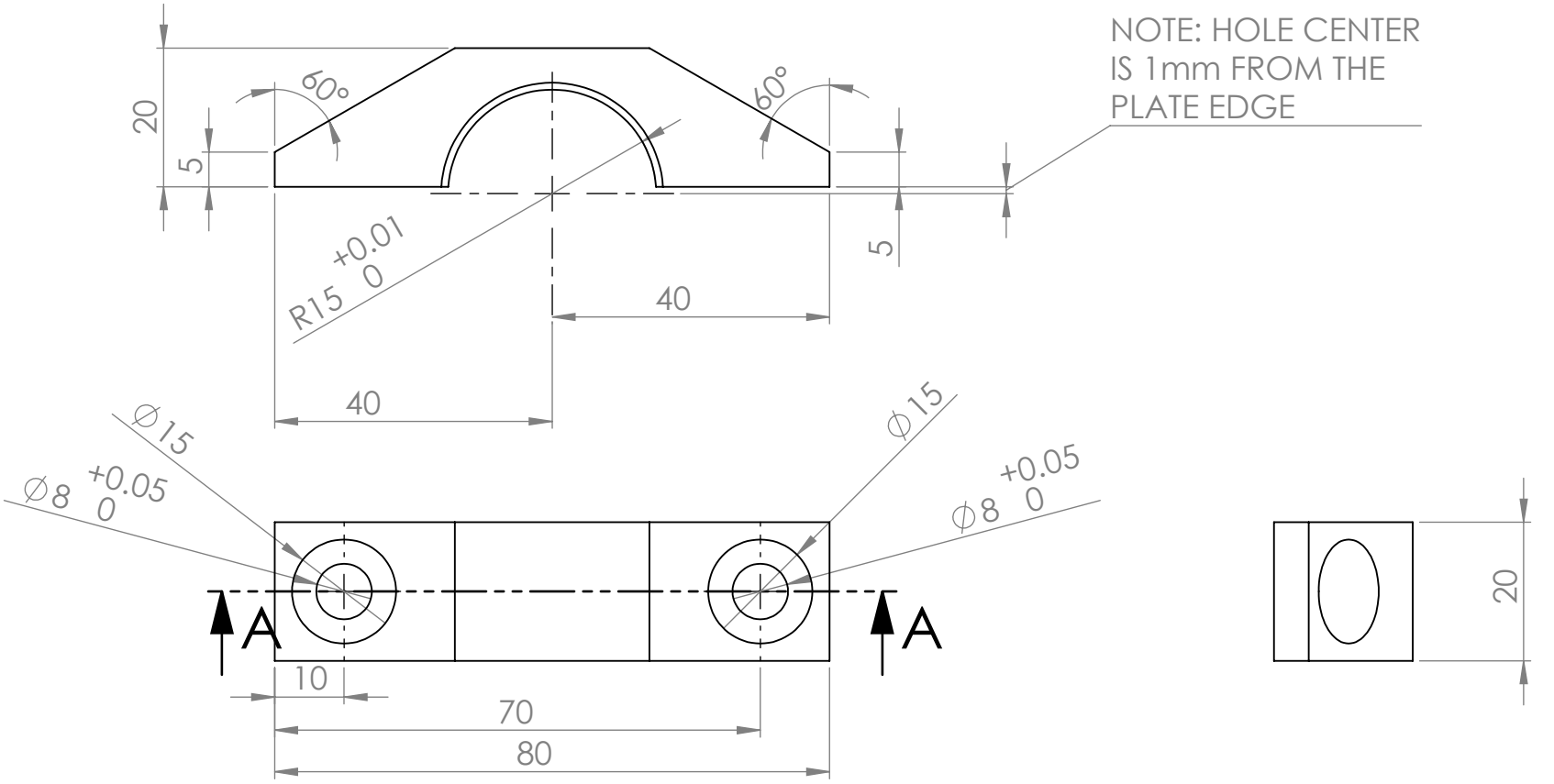

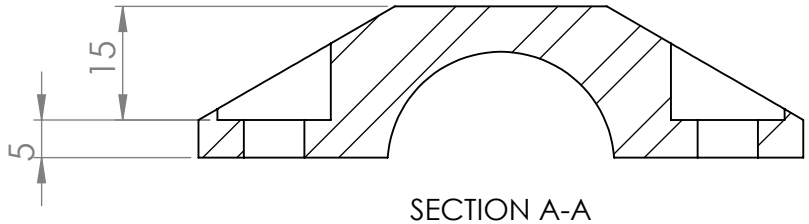

SECTION A-A

UNLESS OTHERWISE SPECIFIED	
LINEAR TOLERANCE	±0.05
ANGULAR TOLERANCE	±1°

DRAWN BY:	BRADEN VAN BREDA	DATE:	UNIVERSITY OF CAPE TOWN
CHECKED:		20/07/2015	
APPROVED:		REVISION:	P0
TITLE: PLATE CLAMPS		DRAWING NO. FTR - P005	
PROJECTION	SCALE 1:1	ALL DIMENSIONS IN MILLIMETRES	

MATERIAL	ALUMINIUM
QUANTITY	1

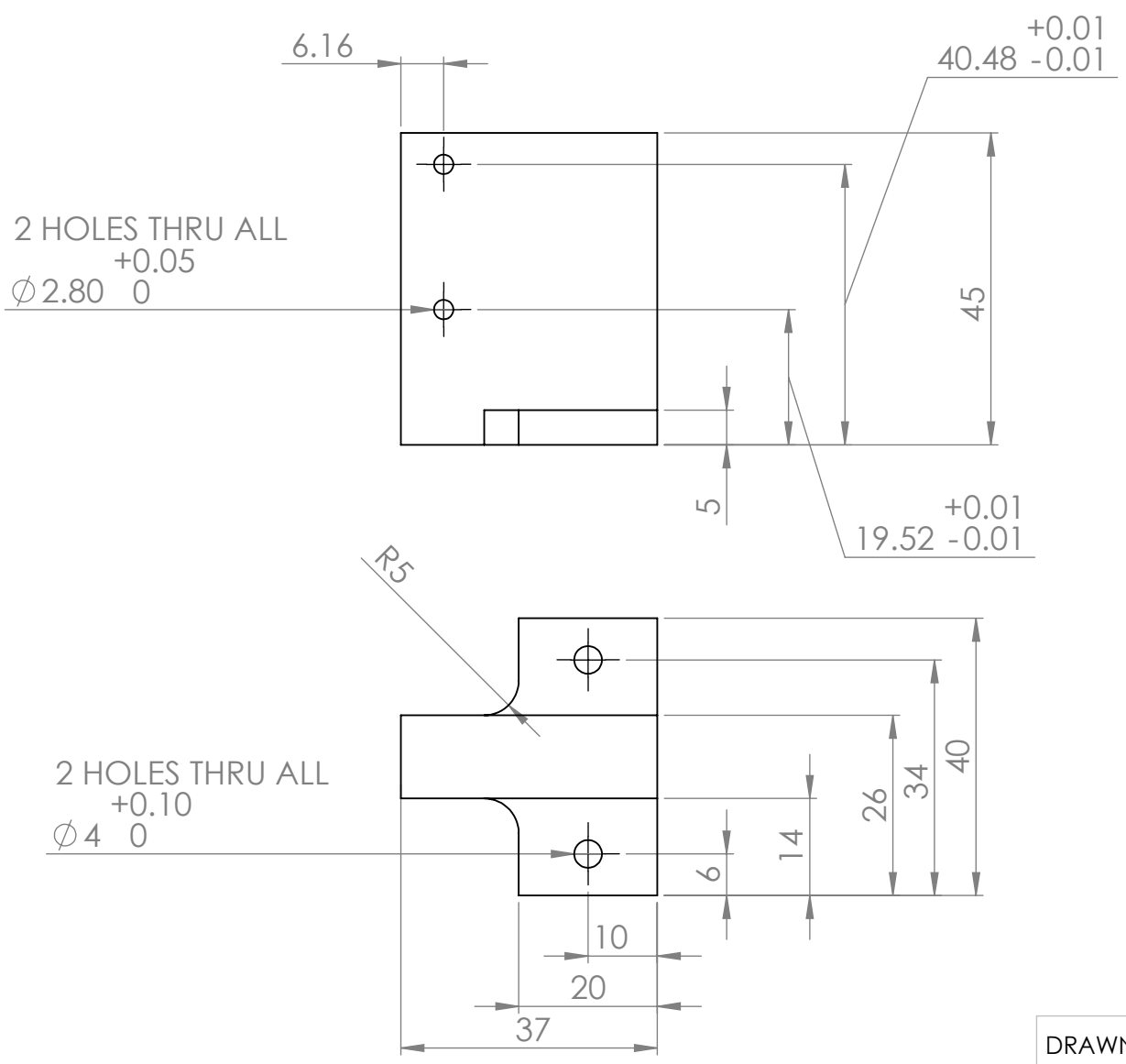

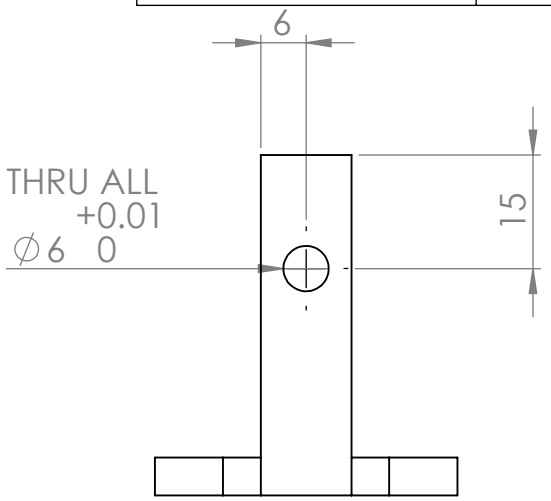

UNLESS OTHERWISE SPECIFIED	
LINEAR TOLERANCE	±0.05
ANGULAR TOLERANCE	±1°

DRAWN BY:	BRADEN VAN BREDA	DATE:	UNIVERSITY OF CAPE TOWN
CHECKED:		20/07/2015	
APPROVED:		REVISION:	P0
TITLE: ENCODER MOUNT		DRAWING NO. FTR - P006	
PROJECTION	SCALE 1:1	ALL DIMENSIONS IN MILLIMETRES	

MATERIAL	STAINLESS STEEL
QUANTITY	1

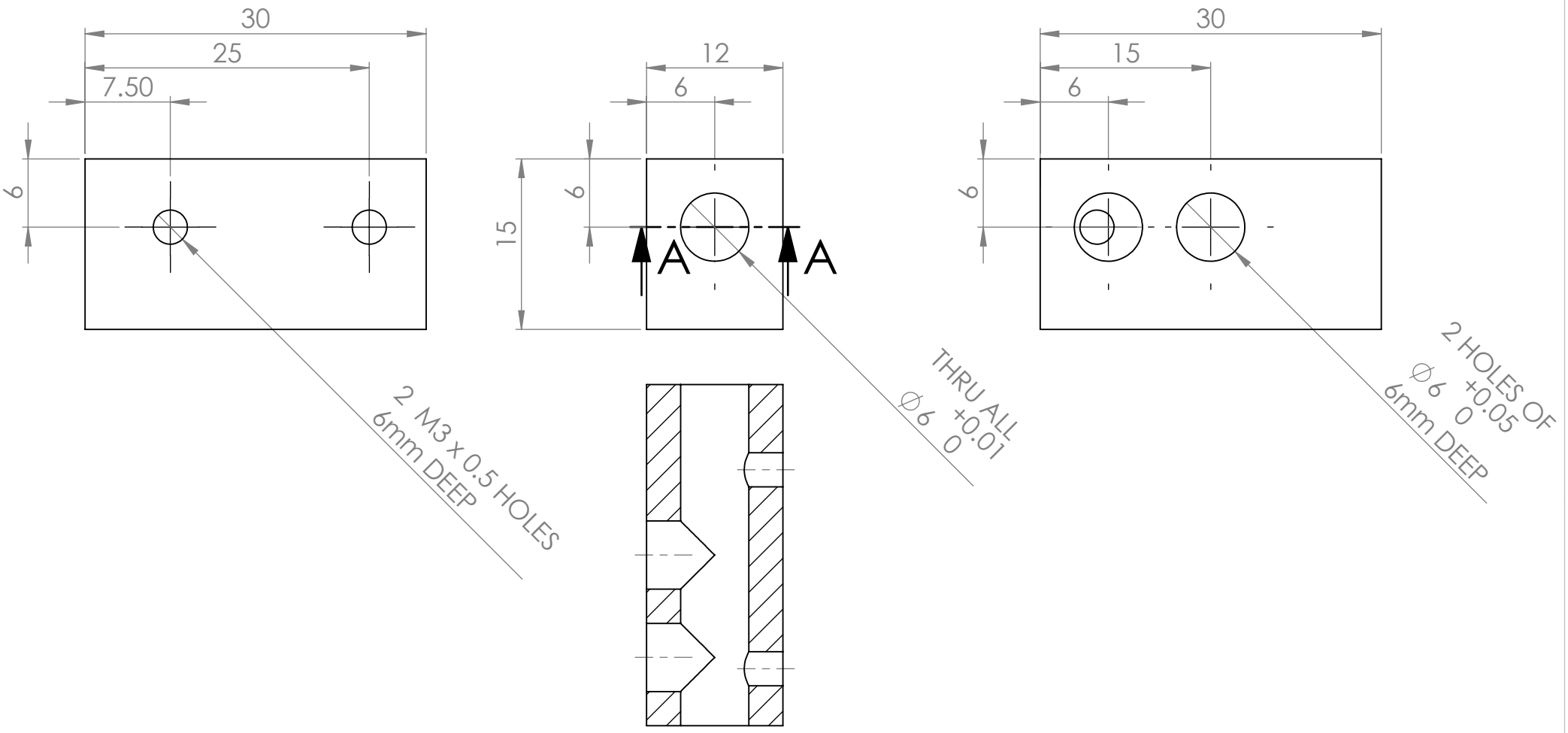

SECTION A-A

UNLESS OTHERWISE SPECIFIED	
LINEAR TOLERANCE	±0.05
ANGULAR TOLERANCE	±1°

DRAWN BY:	BRADEN VAN BREDA	DATE: 20/07/2015	UNIVERSITY OF CAPE TOWN
CHECKED:			
APPROVED:		REVISION:	P0
TITLE: SHAFT COUPLING		DRAWING NO. FTR - P007	
PROJECTION	SCALE 2:1	ALL DIMENSIONS IN MILLIMETRES	

MATERIAL	STAINLESS STEEL
QUANTITY	1

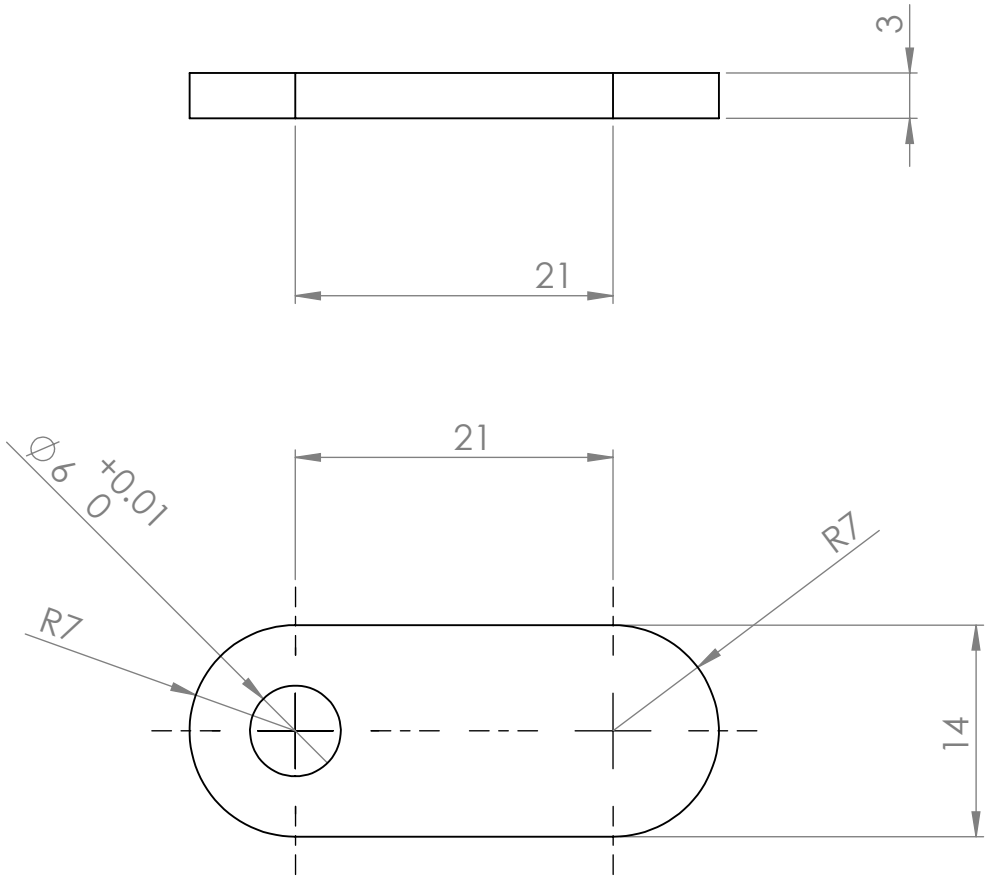

UNLESS OTHERWISE SPECIFIED	
LINEAR TOLERANCE	±0.05
ANGULAR TOLERANCE	±1°

DRAWN BY:	BRADEN VAN BREDA	DATE: 20/07/2015	UNIVERSITY OF CAPE TOWN
CHECKED:			
APPROVED:		REVISION:	P0
TITLE: LOCK HANDLE		DRAWING NO. FTR - P008	
PROJECTION	SCALE 2:1	ALL DIMENSIONS IN MILLIMETRES	

MATERIAL	STAINLESS STEEL
QUANTITY	1

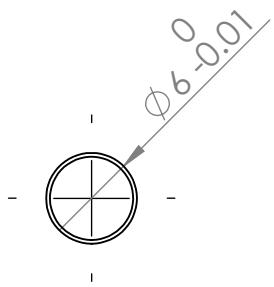

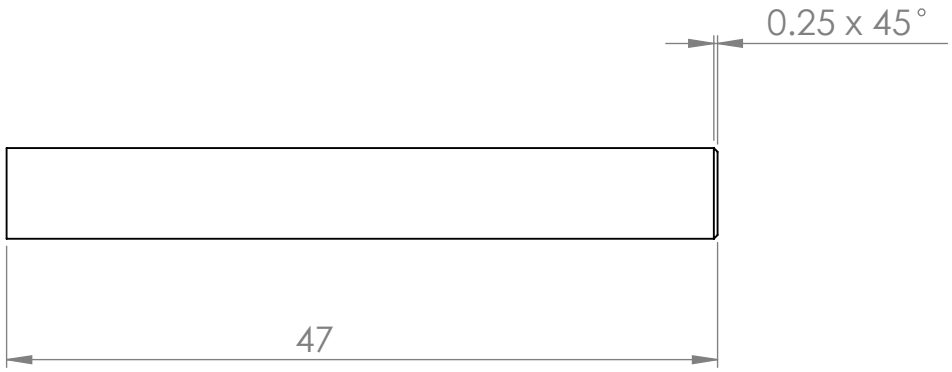

UNLESS OTHERWISE SPECIFIED	
LINEAR TOLERANCE	±0.05
ANGULAR TOLERANCE	±1°

DRAWN BY:	BRADEN VAN BREDA	DATE:	UNIVERSITY OF CAPE TOWN
CHECKED:		20/07/2015	
APPROVED:		REVISION:	P0
TITLE: LOCK ROD		DRAWING NO. FTR - P009	
PROJECTION	SCALE 2:1	ALL DIMENSIONS IN MILLIMETRES	

MATERIAL	STAINLESS STEEL
QUANTITY	12

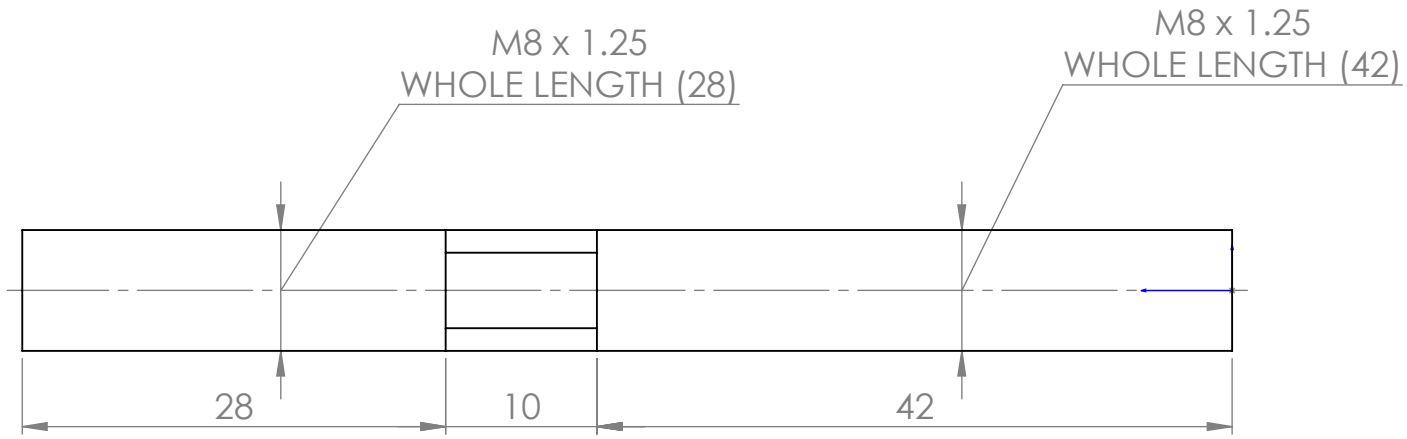

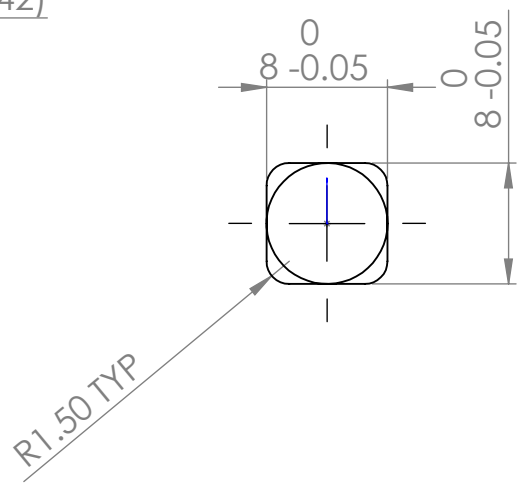

UNLESS OTHERWISE SPECIFIED	
LINEAR TOLERANCE	±0.05
ANGULAR TOLERANCE	±1°

DRAWN BY:	BRADEN VAN BREDA	DATE: 20/07/2015	UNIVERSITY OF CAPE TOWN
CHECKED:			
APPROVED:		REVISION:	P0
TITLE: KEYED BOLT		DRAWING NO. FTR - P010	
PROJECTION	SCALE 2:1	ALL DIMENSIONS IN MILLIMETRES	

MATERIAL	STAINLESS STEEL
QUANTITY	12

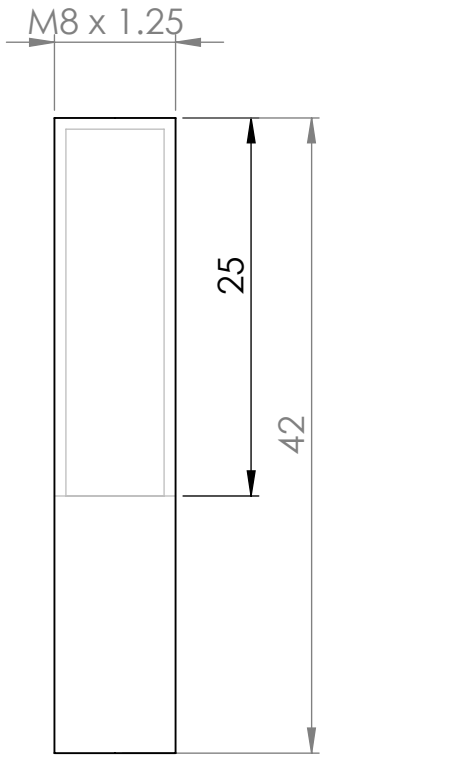

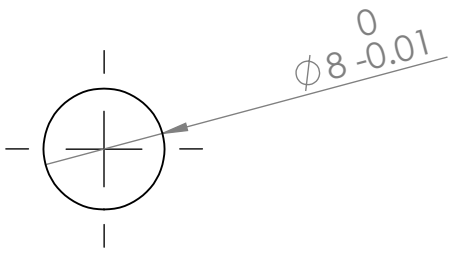

UNLESS OTHERWISE SPECIFIED	
LINEAR TOLERANCE	±0.05
ANGULAR TOLERANCE	±1°

DRAWN BY:	BRADEN VAN BREDA	DATE:	UNIVERSITY OF CAPE TOWN
CHECKED:		20/07/2015	
APPROVED:		REVISION:	P0
TITLE: LOAD CELL TO GRIPS		DRAWING NO. FTR - P011	
PROJECTION	SCALE 2:1	ALL DIMENSIONS IN MILLIMETRES	

MATERIAL	STAINLESS STEEL
QUANTITY	1

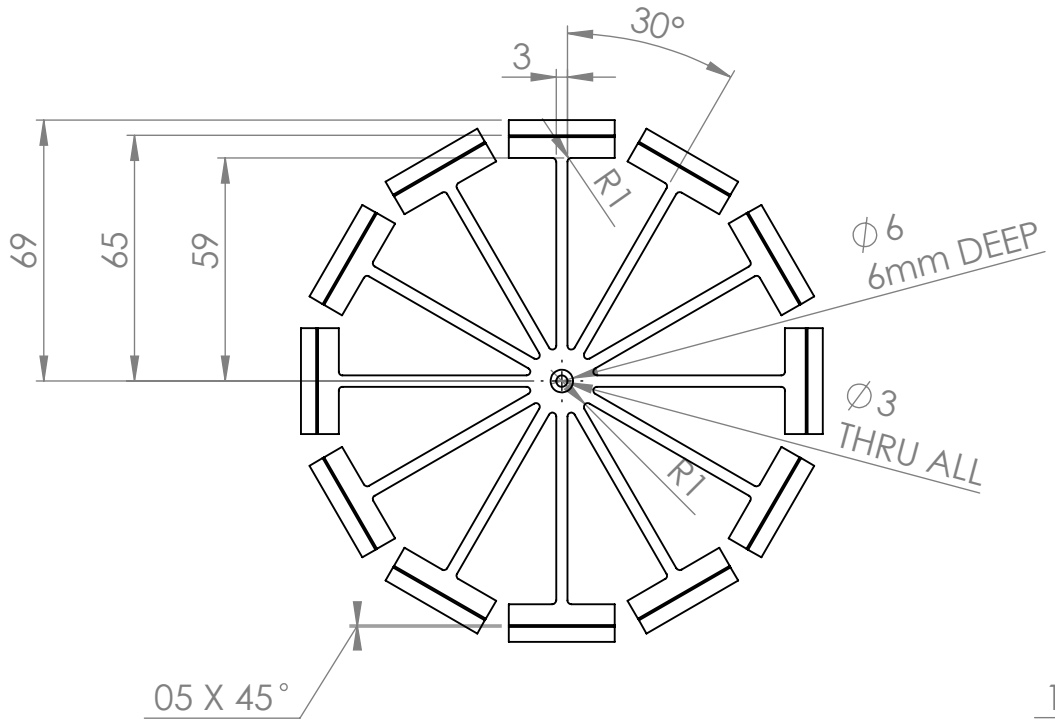

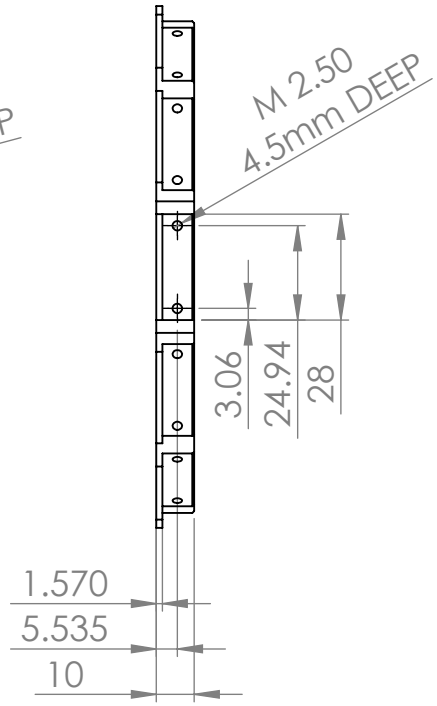

NOTE: 12 IDENTICAL SPOKES EQUI
SPACED 30 DEGREES APART

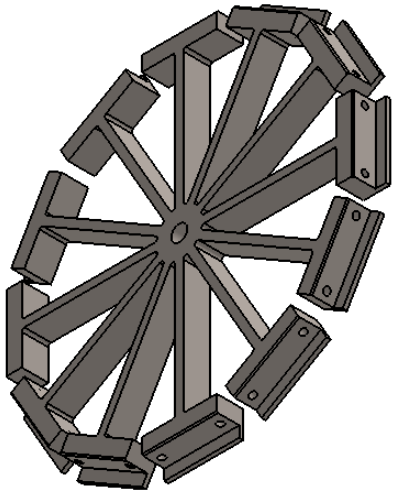

UNLESS OTHERWISE SPECIFIED	
LINEAR TOLERANCE	±0.05
ANGULAR TOLERANCE	±1°

DRAWN BY:	BRADEN VAN BREDA	DATE: 20/07/2015	UNIVERSITY OF CAPE TOWN
CHECKED:			
APPROVED:		REVISION:	P0
TITLE: SPOKE SHAPED CLAMP		DRAWING NO. FTR - P012	
PROJECTION	SCALE 1:2	ALL DIMENSIONS IN MILLIMETRES	

MATERIAL	STAINLESS STEEL
QUANTITY	12

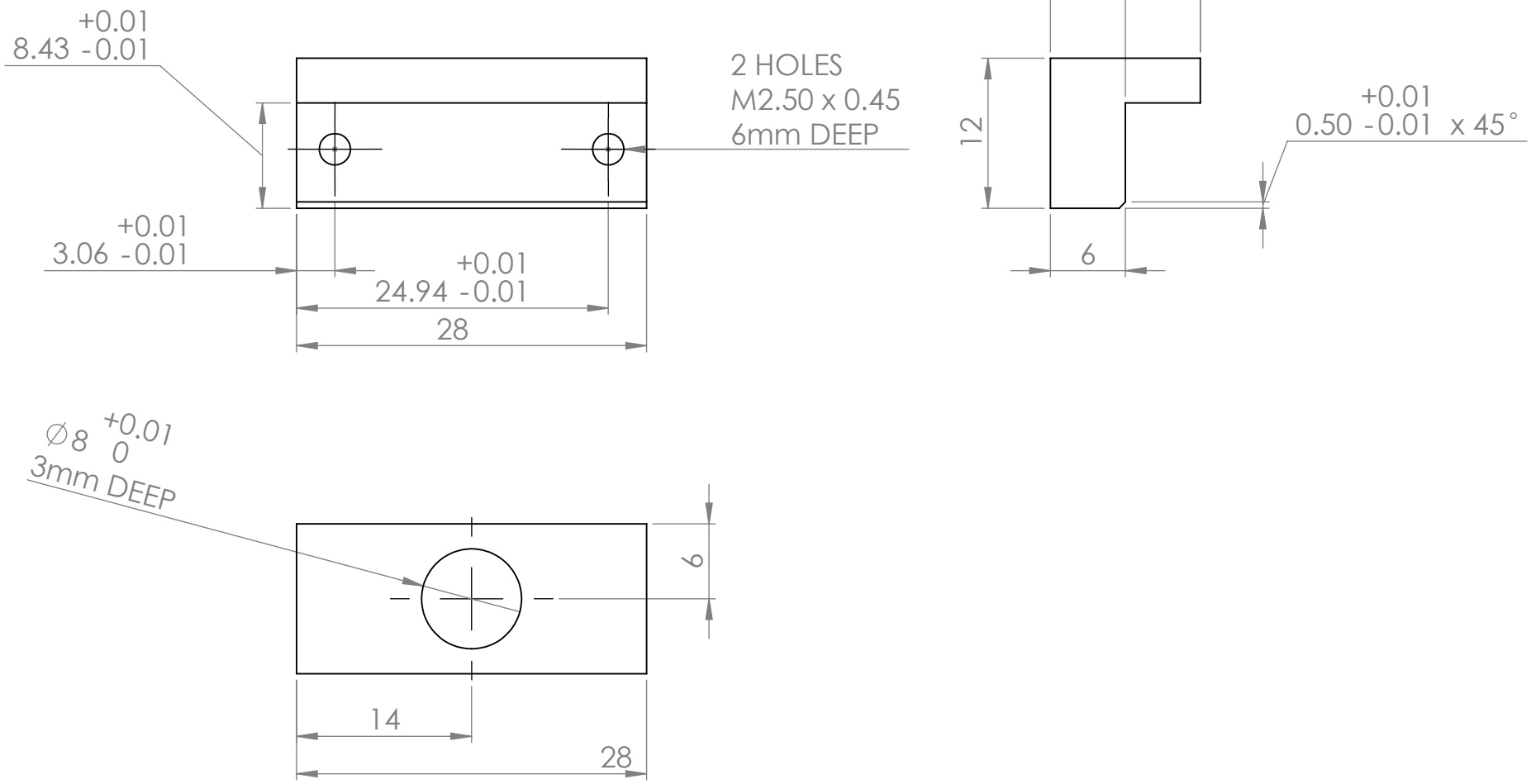

UNLESS OTHERWISE SPECIFIED	
LINEAR TOLERANCE	±0.05
ANGULAR TOLERANCE	±1°

DRAWN BY:	BRADEN VAN BREDA	DATE: 20/07/2015	UNIVERSITY OF CAPE TOWN
CHECKED:			
APPROVED:		REVISION:	P0
TITLE: TOP CLAMP		DRAWING NO. FTR - P013	
PROJECTION	SCALE 2:1	ALL DIMENSIONS IN MILLIMETRES	

MATERIAL	STAINLESS STEEL
QUANTITY	1

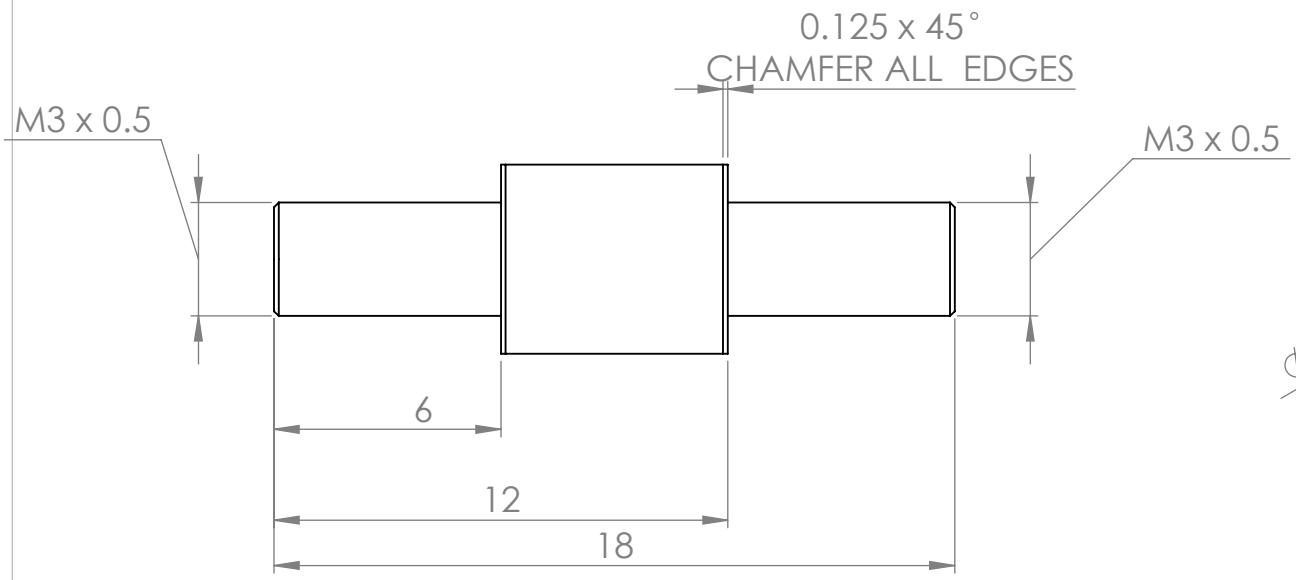

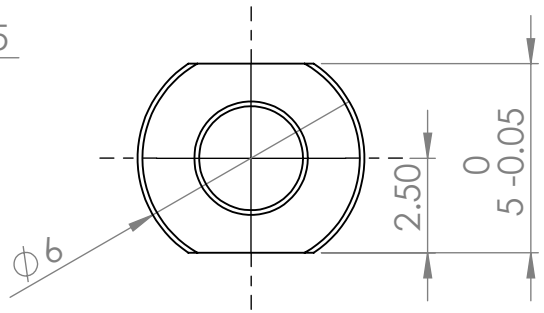

UNLESS OTHERWISE SPECIFIED	
LINEAR TOLERANCE	±0.0.5
ANGULAR TOLERANCE	±1°

DRAWN BY:	BRADEN VAN BREDA	DATE:	UNIVERSITY OF CAPE TOWN
CHECKED:		20/07/2015	
APPROVED:		REVISION:	P0
TITLE: SHAFT EXTENSION		DRAWING NO. FTR - P014	
PROJECTION	SCALE 5:1	ALL DIMENSIONS IN MILLIMETRES	

MATERIAL	STAINLESS
QUANTITY	4

NOTE: BEND RADII CAN VARY
SUBSTANTIALLY AS LONG AS
THE VARIATION IS CONSITENT
FOR ALL 8 BENDS. IE ALL 4 PARTS

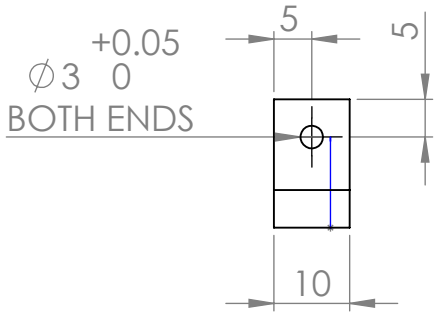

UNLESS OTHERWISE SPECIFIED	
LINEAR TOLERANCE	±0.05
ANGULAR TOLERANCE	±1°

DRAWN BY:	BRADEN VAN BREDA	DATE: 20/07/2015	UNIVERSITY OF CAPE TOWN
CHECKED:			
APPROVED:		REVISION:	P0
TITLE: BENT QLASS BASE		DRAWING NO. FTR - P015	
PROJECTION	SCALE 1:1	ALL DIMENSIONS IN MILLIMETRES	

MATERIAL	STAINLESS STEEL
QUANTITY	24

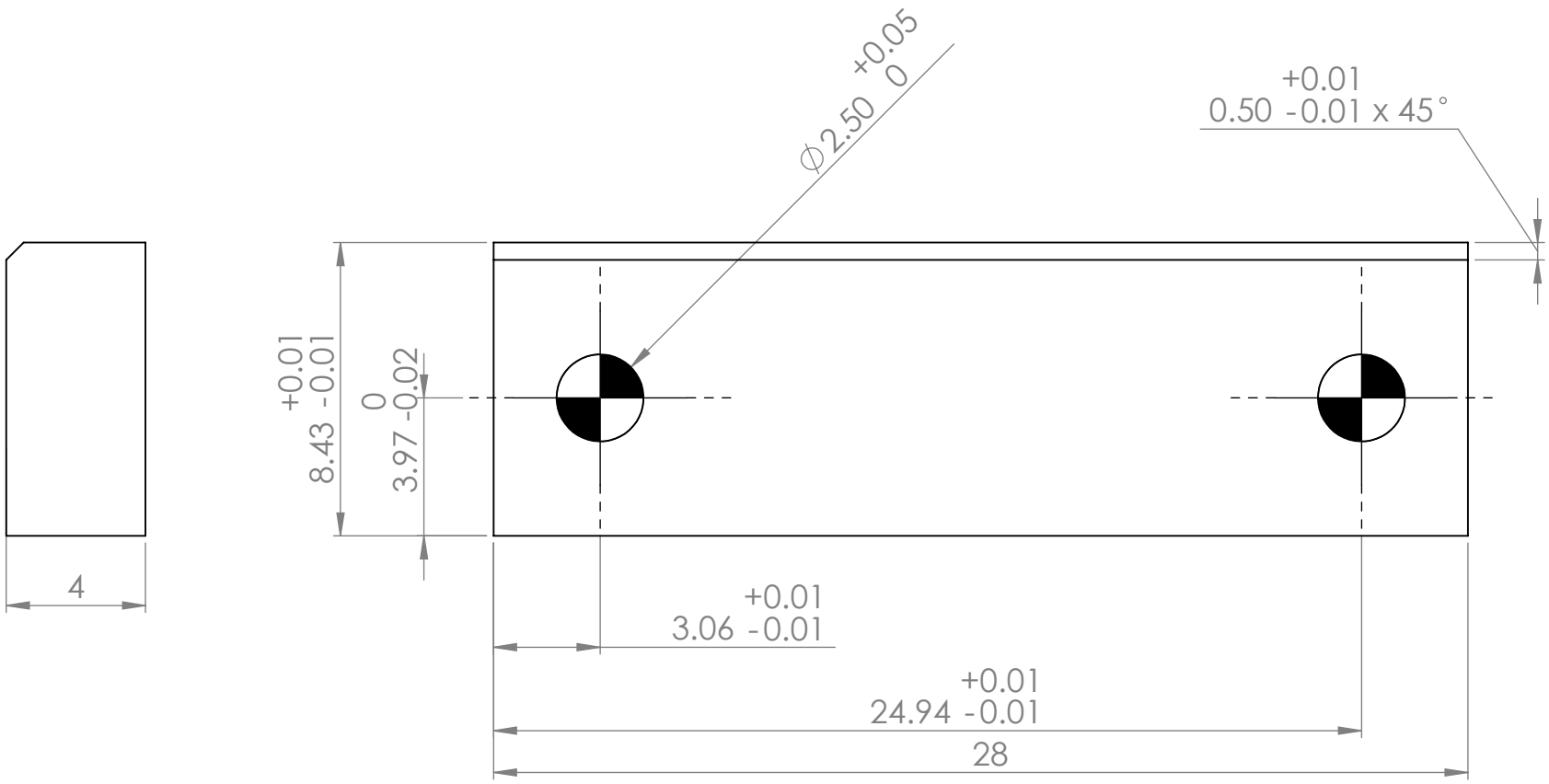

UNLESS OTHERWISE SPECIFIED	
LINEAR TOLERANCE	±0.05
ANGULAR TOLERANCE	±1°

DRAWN BY:	BRADEN VAN BREDA	DATE: 20/07/2015	UNIVERSITY OF CAPE TOWN
CHECKED:			
APPROVED:		REVISION:	P0
TITLE: SHIFTING CLAMP		DRAWING NO. FTR - P016	
PROJECTION	SCALE 5:1	ALL DIMENSIONS IN MILLIMETRES	

MATERIAL	STAINLESS STEEL
QUANTITY	4

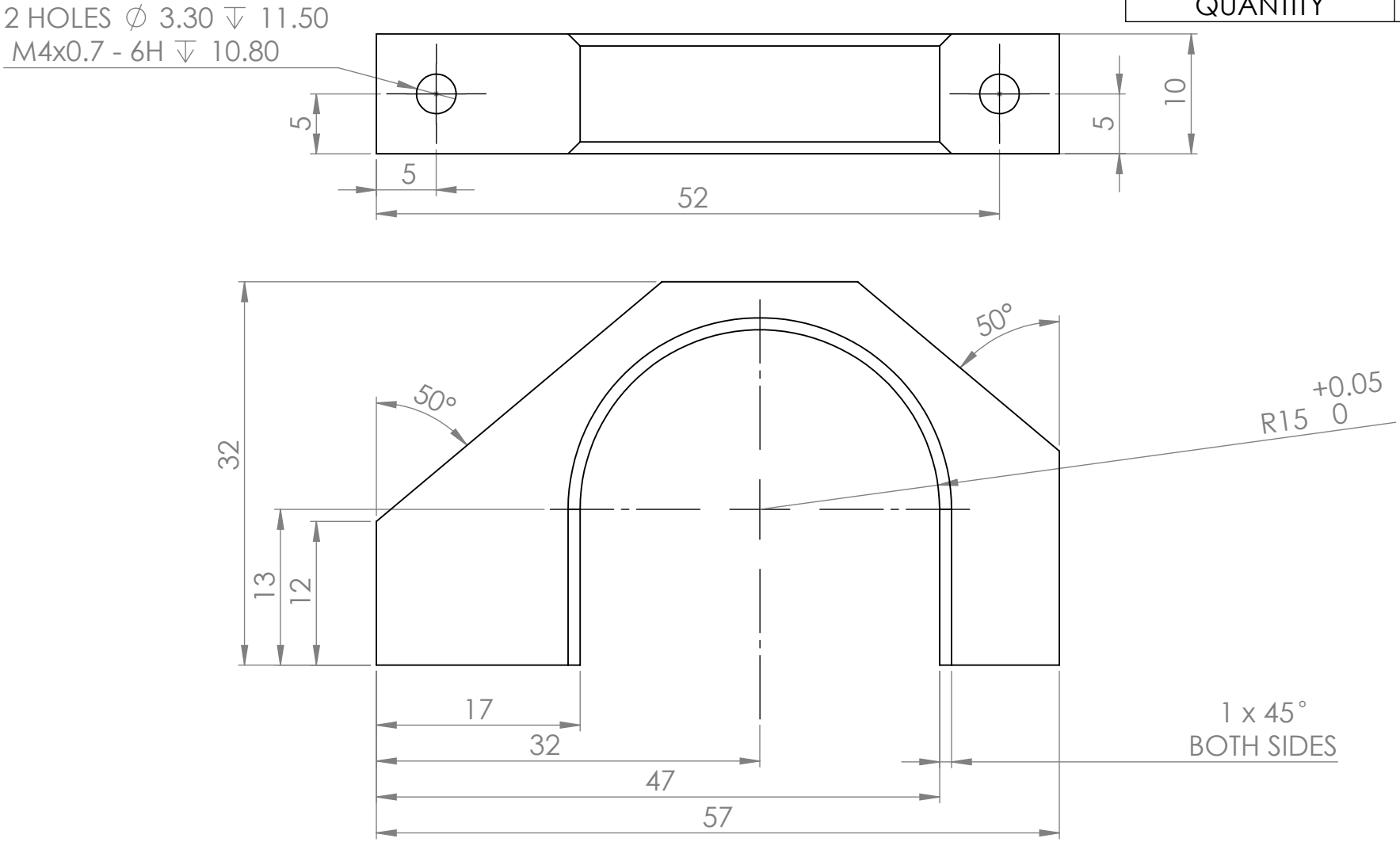

UNLESS OTHERWISE SPECIFIED	
LINEAR TOLERANCE	±0.05
ANGULAR TOLERANCE	±1°

DRAWN BY:	BRADEN VAN BREDA	DATE:	UNIVERSITY OF CAPE TOWN
CHECKED:		20/07/2015	
APPROVED:		REVISION:	P0
TITLE: GLASS HOLDER CLAMP		DRAWING NO. FTR - P018	
PROJECTION	SCALE 1:1	ALL DIMENSIONS IN MILLIMETRES	

MATERIAL	STAINLESS
QUANTITY	4

NOTE: BEND RADII CAN VARY
SUBSTANTIALLY AS LONG AS
THE VARIATION IS CONSITENT
FOR ALL 8 BENDS. IE ALL 4 PARTS

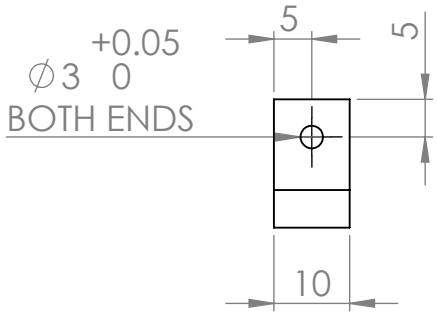

UNLESS OTHERWISE SPECIFIED	
LINEAR TOLERANCE	±0.05
ANGULAR TOLERANCE	±1°

DRAWN BY:	BRADEN VAN BREDA	DATE: 20/07/2015	UNIVERSITY OF CAPE TOWN
CHECKED:			
APPROVED:		REVISION:	P0
TITLE: BENT QLASS BASE		DRAWING NO. FTR - P018	
PROJECTION	SCALE 1:1	ALL DIMENSIONS IN MILLIMETRES	

MATERIAL	STAINLESS STEEL
QUANTITY	2

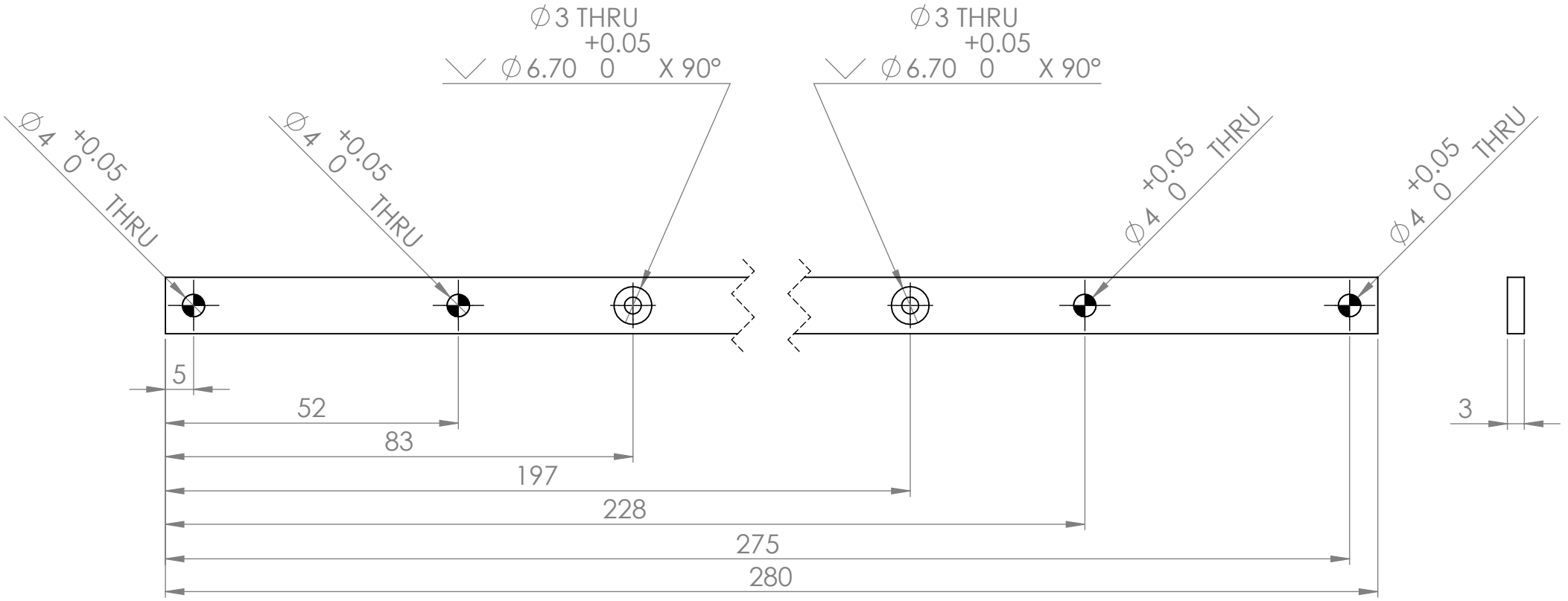

UNLESS OTHERWISE SPECIFIED	
LINEAR TOLERANCE	±0.05
ANGULAR TOLERANCE	±1°

DRAWN BY:	BRADEN VAN BREDA	DATE:	UNIVERSITY OF CAPE TOWN
CHECKED:		20/07/2015	
APPROVED:		REVISION:	P0
TITLE: GLASS HOLDER MAIN		DRAWING NO. FTR - P019	
PROJECTION	SCALE 1:1	ALL DIMENSIONS IN MILLIMETRES	

MATERIAL	RUBBER
QUANTITY	4

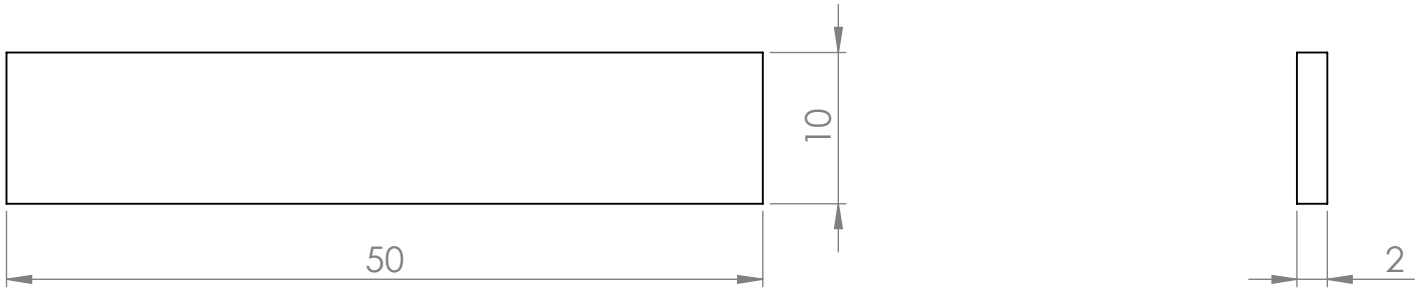

UNLESS OTHERWISE SPECIFIED	
LINEAR TOLERANCE	±0.05
ANGULAR TOLERANCE	±1°

DRAWN BY:	BRADEN VAN BREDA	DATE:	UNIVERSITY OF CAPE TOWN
CHECKED:		20/07/2015	
APPROVED:		REVISION:	P0
TITLE: RUBBER SHORT		DRAWING NO. FTR - P020	
PROJECTION	SCALE 2:1	ALL DIMENSIONS IN MILLIMETRES	

MATERIAL	RUBBER
QUANTITY	2

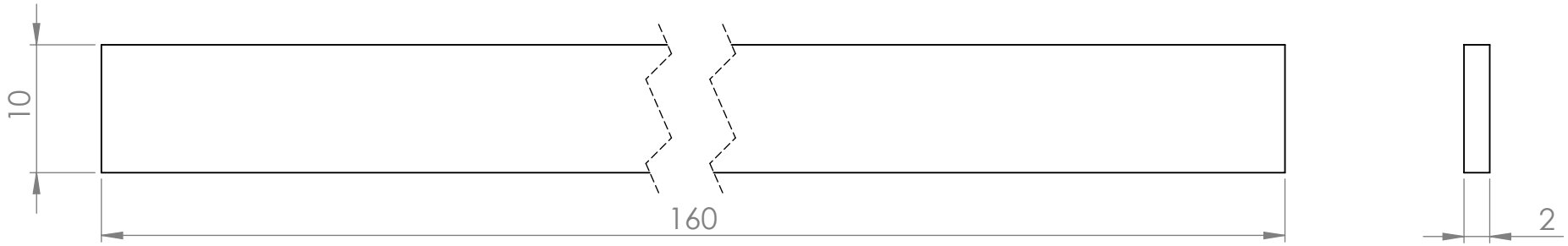

UNLESS OTHERWISE SPECIFIED	
LINEAR TOLERANCE	±0.05
ANGULAR TOLERANCE	±1°

DRAWN BY:	BRADEN VAN BREDA	DATE:	UNIVERSITY OF CAPE TOWN
CHECKED:		20/07/2015	
APPROVED:		REVISION:	P0
TITLE: RUBBER LONG		DRAWING NO. FTR - P021	
PROJECTION	SCALE 2:1	ALL DIMENSIONS IN MILLIMETRES	

MATERIAL	STAINLESS STEEL
QUANTITY	1

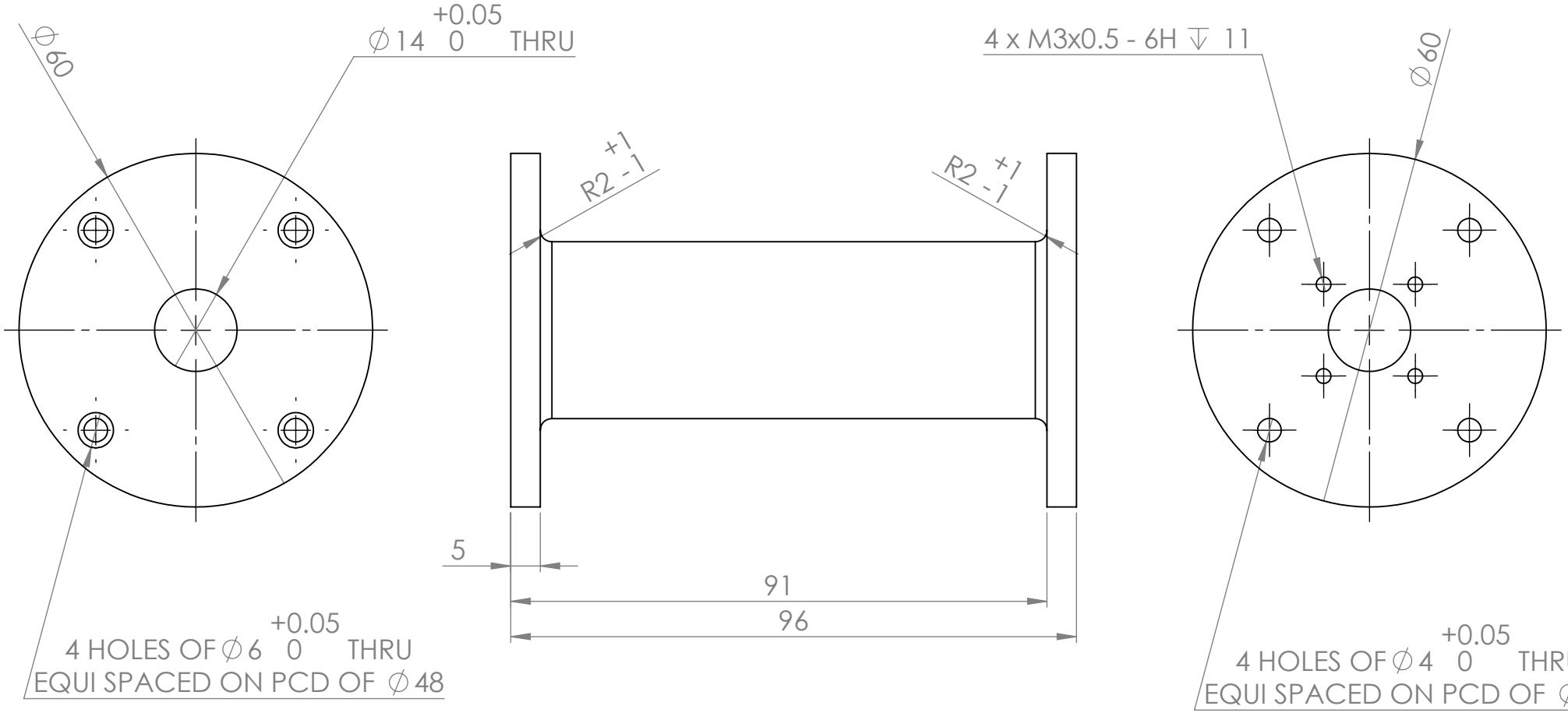

UNLESS OTHERWISE SPECIFIED	
LINEAR TOLERANCE	±0.05
ANGULAR TOLERANCE	±1°

DRAWN BY:	BRADEN VAN BREDA	DATE:	UNIVERSITY OF CAPE TOWN
CHECKED:		20/07/2015	
APPROVED:		REVISION:	P0
TITLE: BEARING SUPPORT		DRAWING NO. FTR - P022	
PROJECTION	SCALE 1:1	ALL DIMENSIONS IN MILLIMETRES	

MATERIAL	PERSPEX
QUANTITY	1

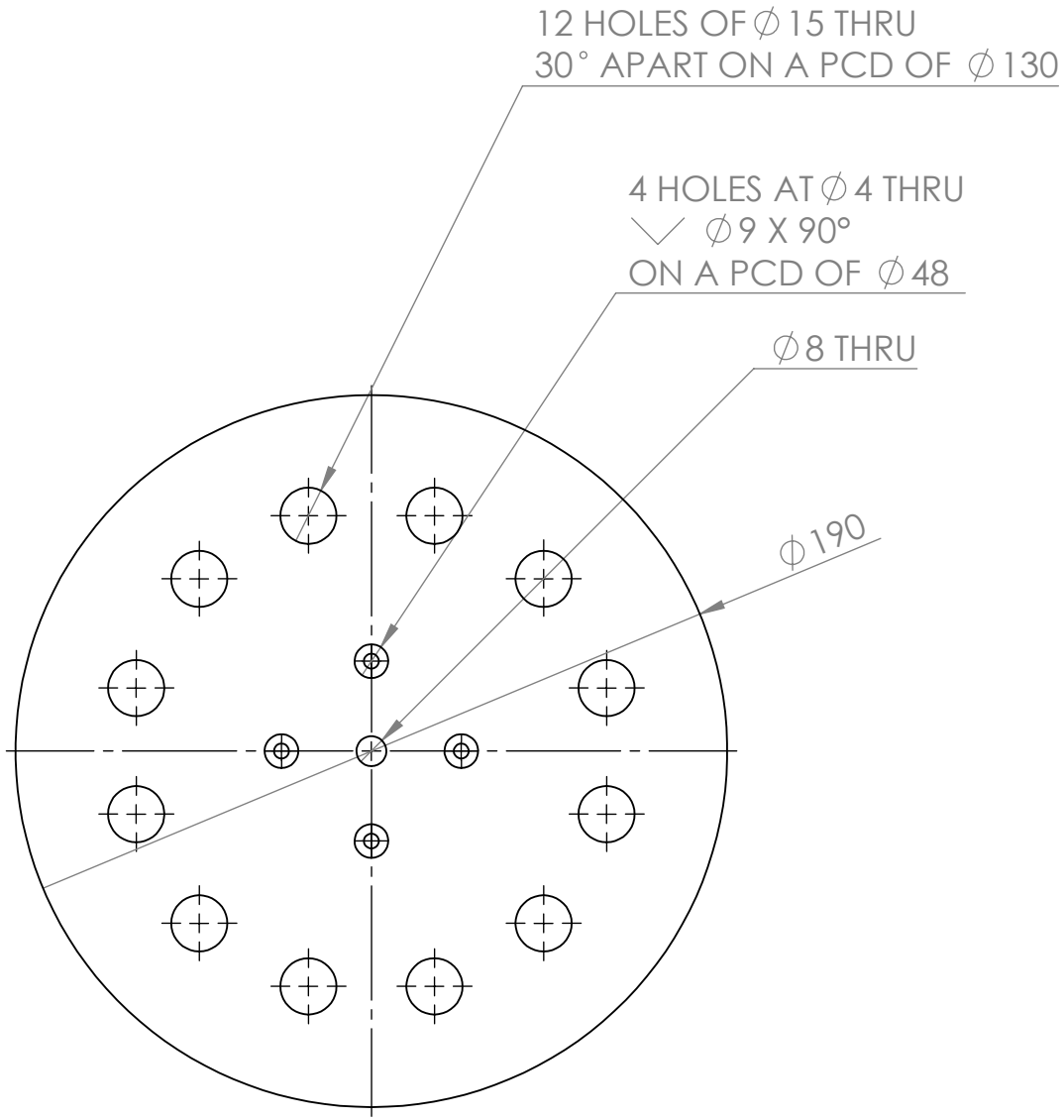

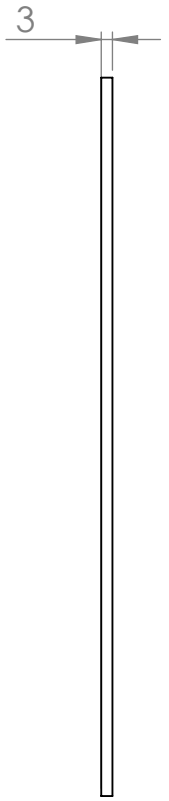

UNLESS OTHERWISE SPECIFIED	
LINEAR TOLERANCE	±0.05
ANGULAR TOLERANCE	±1°

DRAWN BY:	BRADEN VAN BREDA	DATE:	UNIVERSITY OF CAPE TOWN
CHECKED:		20/07/2015	
APPROVED:		REVISION:	P0
TITLE: BOWL COVER		DRAWING NO. FTR - P023	
PROJECTION	SCALE 1:2	ALL DIMENSIONS IN MILLIMETRES	

MATERIAL	PERSPEX
QUANTITY	1

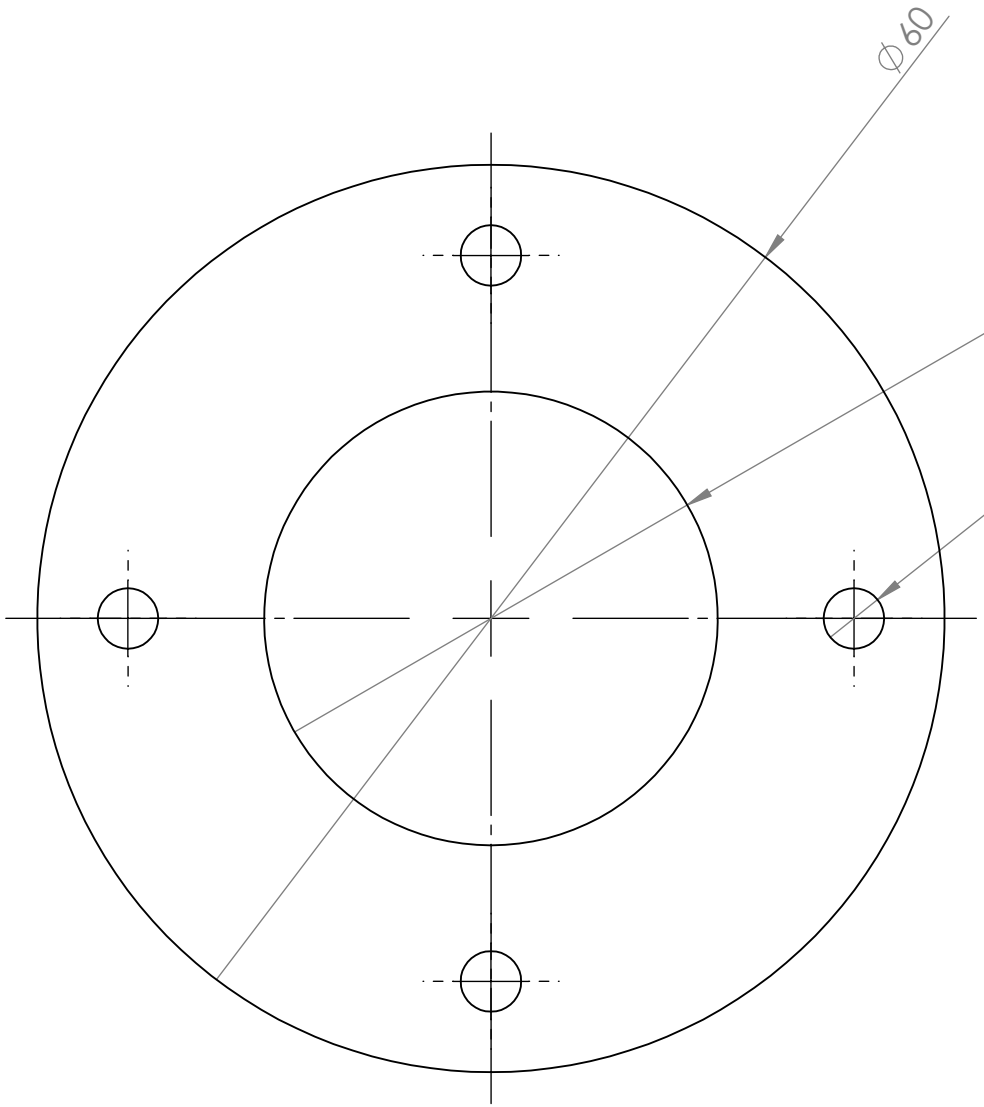

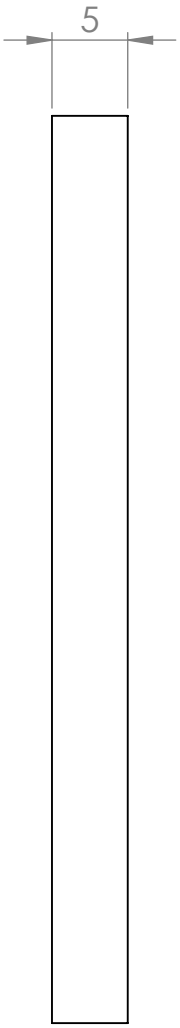

UNLESS OTHERWISE SPECIFIED	
LINEAR TOLERANCE	±0.05
ANGULAR TOLERANCE	±1°

DRAWN BY:	BRADEN VAN BREDA	DATE:	UNIVERSITY OF CAPE TOWN
CHECKED:		20/07/2015	
APPROVED:		REVISION:	P0
TITLE: PERSPEX SPACER		DRAWING NO. FTR - P024	
PROJECTION	SCALE 2:1	ALL DIMENSIONS IN MILLIMETRES	

MATERIAL	PERSPEX
QUANTITY	1

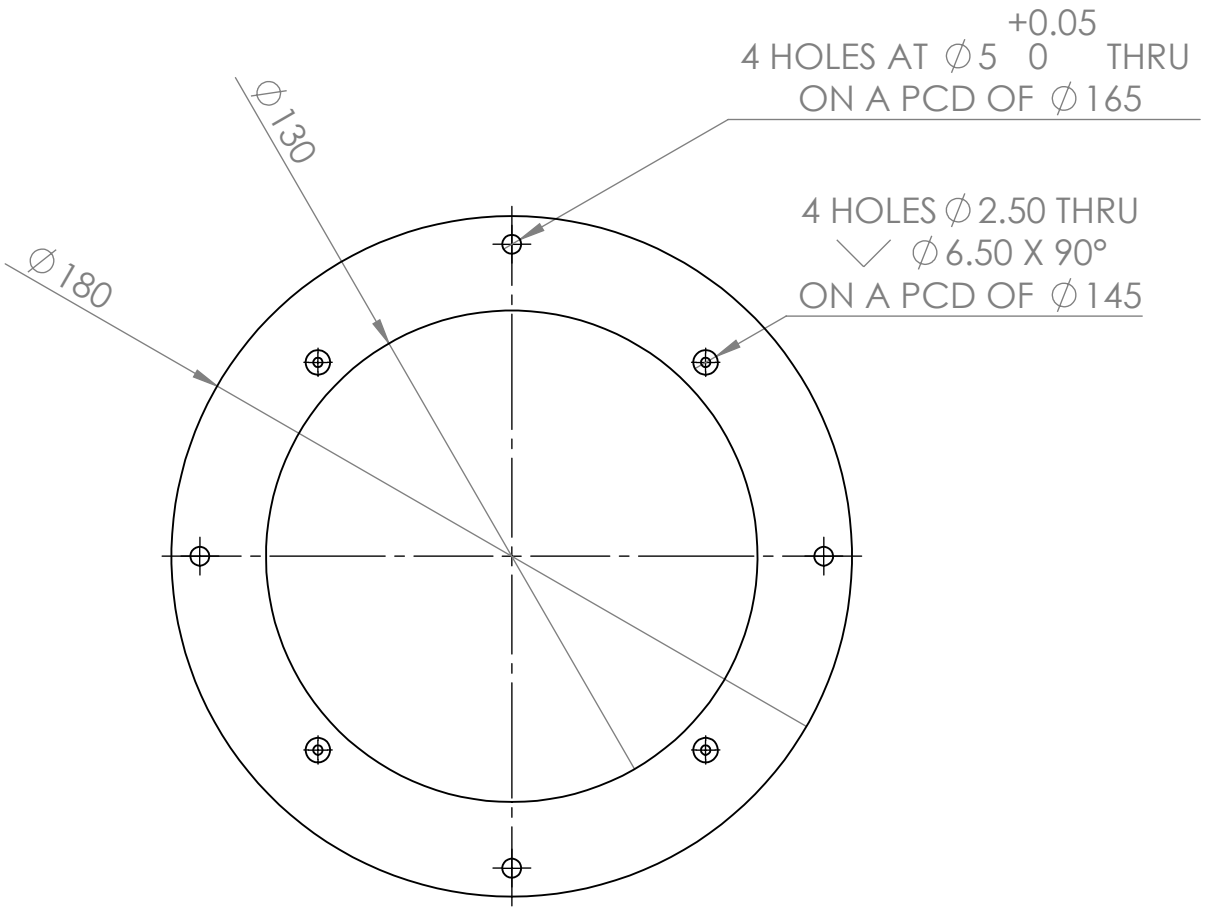

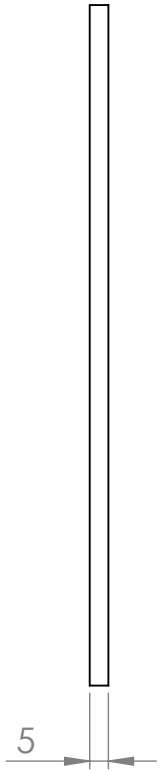

UNLESS OTHERWISE SPECIFIED	
LINEAR TOLERANCE	±0.05
ANGULAR TOLERANCE	±1°

DRAWN BY:	BRADEN VAN BREDA	DATE: 20/07/2015	UNIVERSITY OF CAPE TOWN
CHECKED:			
APPROVED:		REVISION:	P0
TITLE: MOTOR COVER BASE		DRAWING NO. FTR - P025	
PROJECTION	SCALE 1:2	ALL DIMENSIONS IN MILLIMETRES	

MATERIAL	PERSPEX
QUANTITY	1

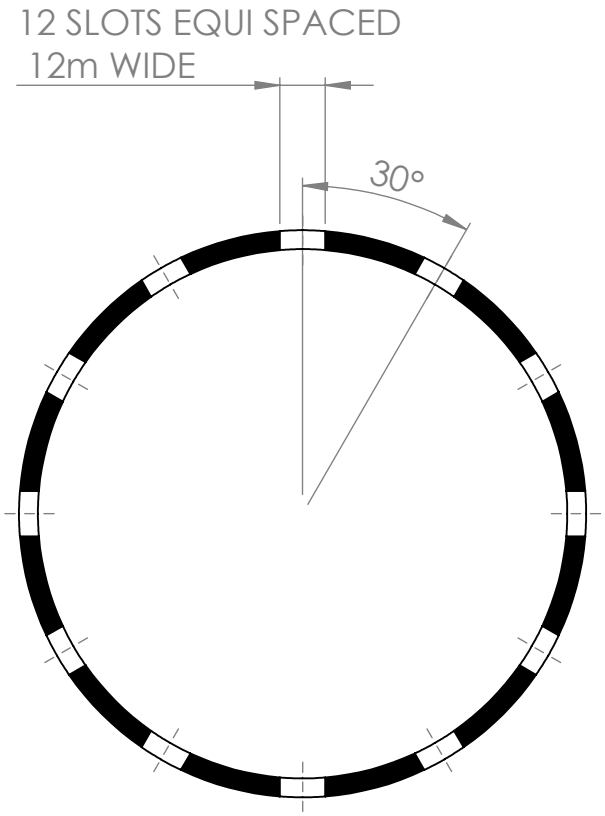

SECTION A-A

SCALE 1 : 2

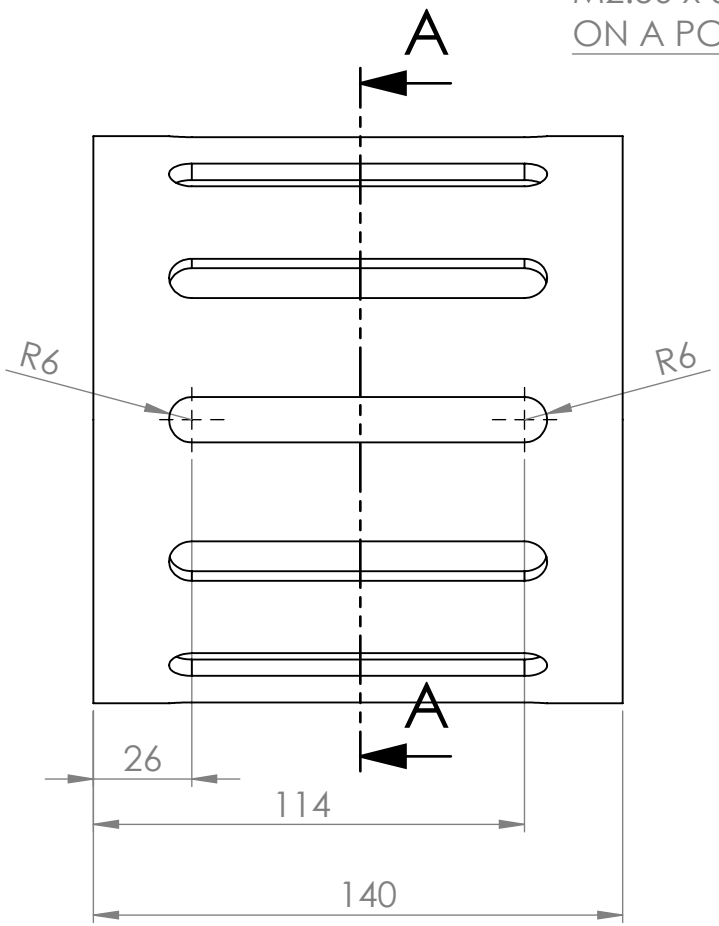

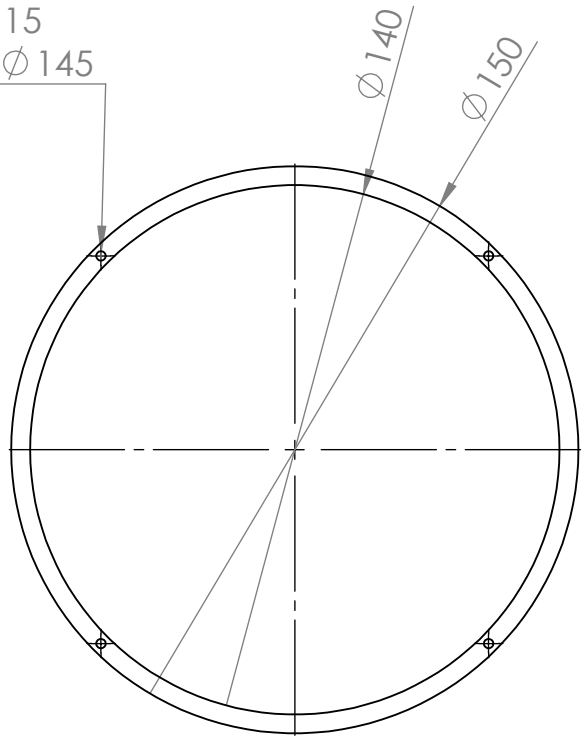

UNLESS OTHERWISE SPECIFIED	
LINEAR TOLERANCE	±0.05
ANGULAR TOLERANCE	±1°

DRAWN BY:	BRADEN VAN BREDA	DATE:	UNIVERSITY OF CAPE TOWN
CHECKED:		20/07/2015	
APPROVED:		REVISION:	P0
TITLE: CYLINDER MOTOR COVER		DRAWING NO. FTR - P026	
PROJECTION	SCALE 1:2	ALL DIMENSIONS IN MILLIMETRES	

MATERIAL	PERSPEX
QUANTITY	1

NOTE: SLOTS ARE MIRRORED
HORIZONTALLY AND VERTICALLY

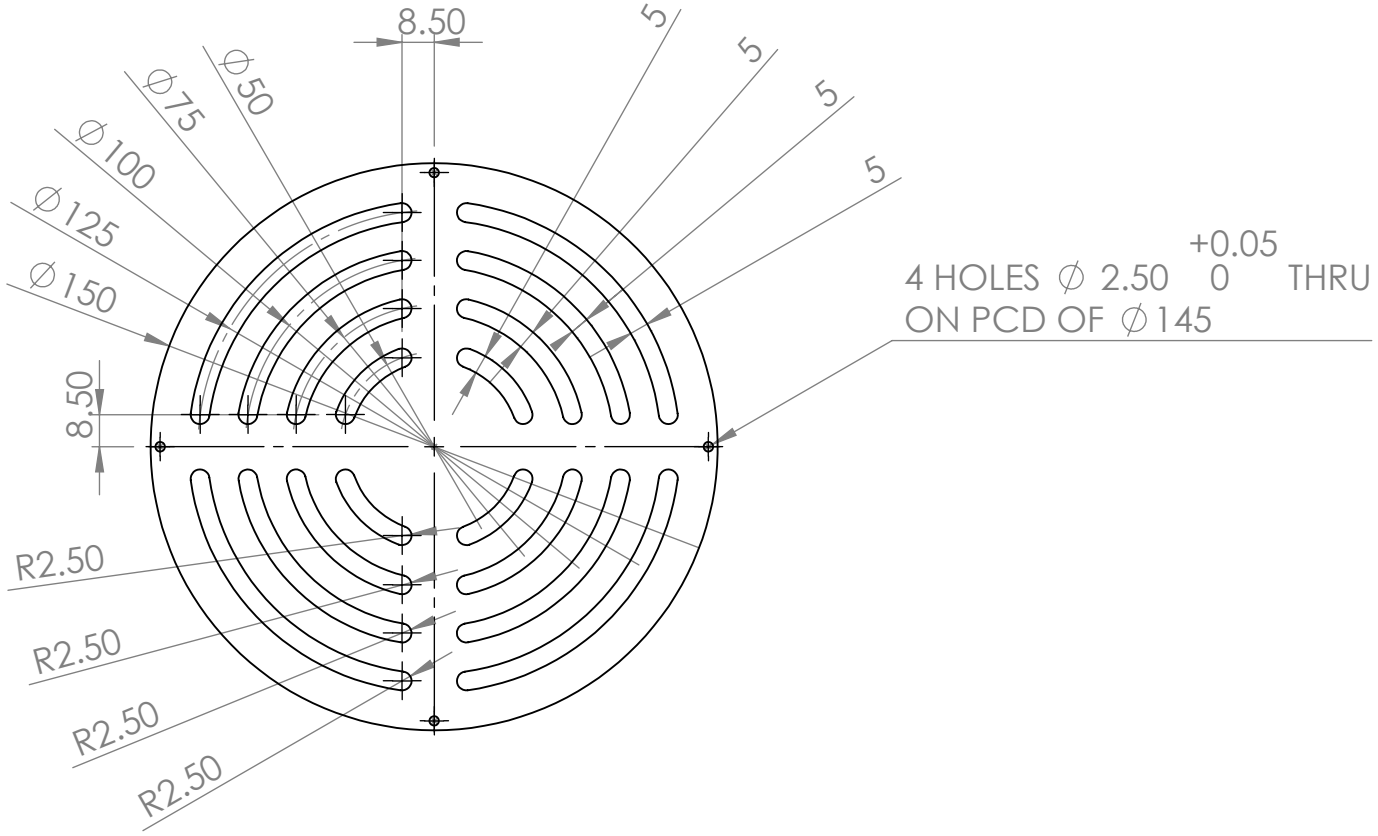

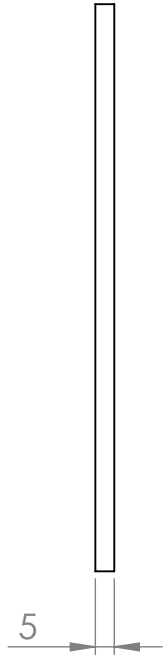

UNLESS OTHERWISE SPECIFIED	
LINEAR TOLERANCE	±0.05
ANGULAR TOLERANCE	±1°

DRAWN BY:	BRADEN VAN BREDA	DATE:	UNIVERSITY OF CAPE TOWN
CHECKED:		20/07/2015	
APPROVED:		REVISION:	P0
TITLE: MOTOR LID		DRAWING NO. FTR - P027	
PROJECTION	SCALE 1:2	ALL DIMENSIONS IN MILLIMETRES	